Evaluation and comparison of bottom-of-atmosphere calibrated Sentinel-2 imagery using SIAM-derived knowledge-based spectral categories

Master Thesis

for the attainment of the Master`s degree “Master of Science”,
abbreviated “MSc”

submitted within the University Master Program for Further Education
“Geographical Information Science & Systems – (UNIGIS MSc)”
at the Department of Geoinformatics - Z_GIS,
Faculty of Digital and Analytical Sciences,
University of Salzburg

submitted by

B.Eng. Oleg Cernenko

Supervisor:
Assoc. Prof. Dr. Dirk Tiede

Munich, 25.02.2026

Acknowledgements

I would like to sincerely thank my supervisor, Associate Professor Dirk Tiede, for the guidance, feedback and academic support provided throughout the development of this Master's thesis. His advice and experience were valuable in shaping this work and supporting me during the research process.

I am especially grateful to the academic and administrative staff of UNIGIS Salzburg for their continuous support throughout the studies. Their assistance, professionalism and willingness to help combined with provided guidance and access to resources contributed in many ways to the successful completion of this degree.

I would also like to thank my family and friends for their patience, understanding and encouragement. My studies required significant time commitment, including many weekends committed to assignments and this thesis. I am very thankful for their care and for accepting my frequent absence during this period.

Finally, my deepest thanks go to my wife. Her constant care, patience and unconditional support made this work possible. She supported me throughout my studies, took care of many responsibilities at home and encouraged me regardless of the challenges. Her understanding and belief in me were a great source of motivation and I am deeply grateful for everything she has done.

This thesis would not be possible without the continuous assistance of all those mentioned above, and I sincerely thank everyone who contributed to this journey.

Abstract

This study investigates the impact of atmospheric and topographic correction on SIAM-based spectral categorization of Sentinel-2 imagery across multiple regions and seasons. While atmospheric corrections are generally considered a necessary preprocessing step in optical remote sensing, its compatibility with systems originally designed for top-of-atmosphere (TOA) reflectance remains uncertain. Therefore, the objective of this research is to evaluate how different atmospheric correction methods influence SIAM stability, inter-method agreement as well as regional and seasonal robustness.

Sentinel-2 images were processed using three atmospheric correction algorithms to generate bottom-of-atmosphere (BOA) reflectance products. SIAM categorization was applied to both uncorrected TOA and corrected BOA datasets. The resulting categories were compared qualitatively and quantitatively across four Austrian regions with diverse terrain and four seasons. Agreement metrics, including overall accuracy, Cohen's Kappa, category retention and inter-method reproducibility were used to evaluate categorization stability. Potential biases were identified, and category change severity was classified.

The results reveal pronounced seasonal and spatial variability. Broad land-cover classes such as vegetation and snow remain relatively stable after correction, while other spectral categories show substantial method-dependent redistribution. Cloud, shadow and water-related categories show the highest rates of disagreement, particularly during seasons characterized by high SZAs. Across the analyzed methods, Sen2Cor and FORCE demonstrate higher mutual consistency than Py6S.

The findings indicate that atmospheric correction does not universally enhance performance of TOA-optimized systems. In fact, the present study demonstrates that even small radiometric differences can cause significant variations in rule-based SIAM-like categorization systems, especially under challenging conditions.

Table of contents

Acknowledgements ii
Abstract iii
Table of contents iv
List of tables v
List of figures vi
List of abbreviations vii
List of appendices x
1. Introduction 1
2. Study objectives 2
3. Theory and concepts 3
 3.1. Physical principles 3
  3.1.1. Scattering and absorption of radiation in the atmosphere 4
  3.1.2. Surface reflectance 6
  3.1.3. Cloud and shadow effects 6
 3.2. Radiative transfer theory 9
 3.3. Topographic correction 11
4. Input data 12
 4.1. Satellite imagery 13
 4.2. Atmospheric properties and aerosol products 17
 4.3. Digital elevation model 18
5. Methodology 19
 5.1. Sen2Cor 21
 5.2. FORCE 24
 5.3. Py6S 27
6. Categorization with SIAM 31
7. Results 32
 7.1. SIAM category distribution analysis 33
 7.2. Inter-method categorization consistency 33
 7.3. Change severity analysis (BOA vs. L1C) 35
 7.4. Spatial patterns of disagreement 37
8. Discussion 39
9. Conclusions and outlook 42
List of references viii
Appendices xv

List of tables

Table 1 - Sentinel-2 (L1C) data used for each study region and season 14
Table 2 - Spectral information per band for S2A and S2B (European Space Agency, 2025b) 17
Table 3 - Conceptual comparison of atmospheric and topographic correction approaches...21
Table 4 - SIAM categories with their colour symbolization, abbreviations and descriptions (Major et al., 2025, Table 2).. lix

List of figures

Figure 1 - The Earth's annual global mean energy budget in W/m² (Rottman, 2007) 5
Figure 2 - Typical spectral signatures of thick clouds, fresh snow and bare soil in the visible, near infrared and shortwave infrared ranges (adapted from GEOLab, 2021)........................ 7
Figure 3 - Example of erosion and dilation operations with a radius of 3 pixels. (a) Potential false positive cloud layer. (b) Remaining pixels after erosion. (c) Cloud recovered by dilation (Qiu et al., 2019).. 8
Figure 4 - Grey image with clouds (left - peaks) and shadows (right - valleys) presented as topographic surface (Statella and Erivaldo, 2008). 9
Figure 5 - Study regions (from left to right): Alpine valleys, High Alps, Pre-Alps, Eastern planes 13
Figure 6 - SAFE file content of a Sentinel-2 product (European Space Agency, 2025a).......15
Figure 7 - Distribution of Sentinel-2 satellites over the mission orbit (European Space Agency, 2025b) 16
Figure 8 - Flow chart of Sen2Cor atmospheric correction processing chain (European Space Agency, 2021) 23
Figure 9 - FORCE Level 2 Processing System (L2PS) workflow. WVDB - water vapor database; BT - brightness temperature; QAI - quality assurance information (Frantz, 2019) 25
Figure 10 - Sample 6S input file (Wilson, 2013)..28
Figure 11 - Classification differences in winter (red - UNKNOWN category) 38
Figure 12 - Classification differences over water (left - winter, right - spring) 38

List of abbreviations

6

6S.. *Second Simulation of the Satellite Signal in the Solar Spectrum*

A

AC...*Atmospheric Correction*
AOD .... *Aerosol Optical Depth*
AOI...*Area Of Interest*
AOT...*Aerosol Optical Thickness*
APDA .... *Atmospheric Pre-corrected Differential Absorption algorithm*
ARD ....*Analysis ready data*
ASTER GDEM...*Advanced Spaceborne Thermal Emission and Reflection Radiometer Global Digital Elevation Model*
ATBD ....*Level-2A Algorithm Theoretical Basis Document*

B

BOA .... *Bottom-of-atmosphere*
BRDF ....*Bidirectional Reflectance Distribution Function*
BT ....*Brightness Temperature*

C

CAMS... *Copernicus Atmosphere Monitoring System*
CSD .... *Cloud Storage Downloader*

D

DDV ....*Dark Dense Vegetation*
DEM ....*Digital Elevation Model*

E

EAC4...*ECMWF Atmospheric Composition Reanalysis 4*
ECMWF...*European Centre for Medium-Range Weather Forecasts*
EO.. *Earth Observation*
ESA.. *European Space Agency*

F

FORCE .....*Framework for Operational Radiometric Correction and Environmental monitoring*

G

GLO-30 .... *Copernicus DEM*
GMAO .... *Global Modelling and Assimilation Office*
GUI.. *Graphical User Interface*

L

L2PS .... *FORCE Level 2 Processing System*
LUT .... *Lookup Table*

M

MERRA-2 .... *Modern-Era Retrospective analysis for Research and Applications, Version 2*
MM .... *Mathematical Morphology*
MODIS .... *Moderate Resolution Imaging Spectroradiometer*
MSI.. *Multispectral Imager*, *Multispectral Imager*

N

NASA .... *National Aeronautics and Space Administration*
NBAR .... *Nadir BRDF-Adjusted Reflectance*
NIR... *Near infrared*

P

Py6S ...... *Python interface for Second Simulation of the Satellite Signal in the Solar Spectrum*

R

RTE.. *Radiative Transfer Equation*, *Radiative Transfer Equation*

S

S2 L1C *Sentinel-2 Level-1C*
S2 L2A *Sentinel-2 Level-2A*
SC .... *Scene Classification*
Sen2Cor .... *Sentinel-2 Correction*
SIAM .... *Satellite Image Automatic Mapper*
SRTM .... *Shuttle Radar Topography Mission*
STEP.. *Science Toolbox Exploration Platform*
SWIR.. *Shortwave infrared*
SZA .... *Solar Zenith Angle*

T

TIR .... *Thermal infrared*
TOA........ *Top-of-atmosphere*
TOD .... *Total Optical Depth*
TROPOMI .... *Tropospheric Monitoring Instrument*

U

UTM .... *Universal Transversal Mercator*
UV........ *ultraviolet*

V

VIS .... *Visible*
VNIR .... *Very near infrared*

W

WVDB .... *Water Vapor Database*

List of appendices

Appendix A – Sentinel-2 L1C data used in this study xv

Appendix B – FORCE parameter file xvi

Appendix C – Alpine valleys – Class (category) distribution (from top to bottom: winter, spring, summer, autumn) xix

Appendix D – High Alps – Class (category) distribution (from top to bottom: winter, spring, summer, autumn) xxi

Appendix E – Pre-Alps – Class (category) distribution (from top to bottom: winter, spring, summer, autumn) xxiii

Appendix F – Eastern planes – Class (category) distribution (from top to bottom: winter, spring, summer, autumn) xxv

Appendix G – Alpine valleys – Pairwise agreement BOA-BOA (from top to bottom: winter, spring, summer, autumn) xxvii

Appendix H – High Alps – Pairwise agreement BOA-BOA (from top to bottom: winter, spring, summer, autumn) xxviii

Appendix I – Pre-Alps – Pairwise agreement BOA-BOA (from top to bottom: winter, spring, summer, autumn) xxix

Appendix J – Eastern planes – Pairwise agreement BOA-BOA (from top to bottom: winter, spring, summer, autumn) xxx

Appendix K – Category stability across seasons xxxi

Appendix L – Alpine valleys – change magnitude (from top to bottom: winter, spring, summer, autumn) xxxv

Appendix M – High Alps – change magnitude (from top to bottom: winter, spring, summer, autumn) xxxvii

Appendix N – Pre-Alps – change magnitude (from top to bottom: winter, spring, summer, autumn) xxxix

Appendix O – Eastern planes – change magnitude (from top to bottom: winter, spring, summer, autumn) xli

Appendix P - Alpine valleys – systematic bias (from top to bottom: winter, spring, summer, autumn) xliii

Appendix Q – High Alps – systematic bias (from top to bottom: winter, spring, summer, autumn) xliv

Appendix R – Pre-Alps – systematic bias (from top to bottom: winter, spring, summer, autumn) xlv

Appendix S – Eastern planes – systematic bias (from top to bottom: winter, spring, summer, autumn) xlvi

Appendix T - Alpine valleys – change severity distribution (from top to bottom: winter, spring, summer, autumn) xlvii
Appendix U – High Alps – change severity distribution (from top to bottom: winter, spring, summer, autumn) xlix
Appendix V – Pre-Alps – change severity distribution (from top to bottom: winter, spring, summer, autumn) li
Appendix W – Eastern planes – change severity distribution (from top to bottom: winter, spring, summer, autumn) liii
Appendix X - Alpine valleys – cover type stability (from top to bottom: winter, spring, summer, autumn) lv
Appendix Y – High Alps – cover type stability (from top to bottom: winter, spring, summer, autumn) lvi
Appendix Z – Pre-Alps – cover type stability (from top to bottom: winter, spring, summer, autumn) lvii
Appendix AA – Eastern planes – cover type stability (from top to bottom: winter, spring, summer, autumn) lviii
Appendix AB – SIAM categories lix

1. Introduction

Since its launch in 2014, Copernicus, the European Space Agency's (ESA) Earth observation component consisting of dedicated satellites and instruments called Sentinels and existing public and commercial satellites referred to as Contributing Missions, has been providing its users with accurate Earth Observation (EO) data worldwide.

One of the most recent and widely used multispectral EO missions - Sentinel-2 - is based on a constellation of two identical satellites in the same orbit positioned 180° apart, each carrying a novel Multispectral Imager (MSI) with 13 spectral bands, a wide swath (290 km), high resolution (10, 20 and 60 m) and a 5-day revisit time at the equator (European Space Agency, n.d.). These high-resolution satellite images help policymakers and researchers to track and support urban area management, sustainable agriculture, forestry, civil protection, climate change and many more areas of application (European Commission - Directorate-General for Defence Industry and Space, n.d.).

While obtaining satellite images, solar radiation travelling through the atmosphere of the Earth undergoes changes in terms of its spectral and spatial properties. In order to mitigate these effects, an atmospheric correction must be applied to the energy reflected by the surface of the Earth and registered by a satellite sensor (Raiyani et al., 2021). This preprocessing is one of the most crucial steps in satellite data analysis as it can have an effect on the final result (Rumora et al., 2020).

Over the years multiple different approaches and technical implementations have been created in order to mitigate atmospheric effects – each with its own requirements, strengths and weaknesses. These are, for example, Sen2Cor (correction processor for Sentinel-2 images, developed on behalf of ESA) (Main-Knorn et al., 2017), 6S (Second Simulation of the Satellite Signal in the Solar Spectrum) (Vermote et al., 1997) and FORCE (Framework for Operational Radiometric Correction for Environmental monitoring) (Frantz, 2020a), to name a few.

The resulting actual reflectance values of a surface is referred to as a bottom-of-atmosphere (BOA) reflectance, as opposed to the top-of-atmosphere (TOA) reflectance, which is a mix of electromagnetic radiation, reflected off the surface and attenuated by the atmosphere. The equivalent Sentinel-2 products are called Sentinel-2 Level 1C (S2 L1C - TOA reflectance images) and Sentinel-2 Level 2A (S2 L2A - BOA reflectance images, derived from the corresponding S2 L1C products).

Nevertheless, with this approach alone, large amounts of data still stay underutilized due to the technical expertise needed for gathering actual information from this numerical, sensory data. One way to counteract this is to perform a semantic enrichment of EO data, which allows users to run semantic queries on scene content rather than raw statistics. The Satellite Image Automatic Mapper (SIAM) software is capable of categorizing satellite images based on their reflectance values. It is a rapid, fully automated system designed to process large EO datasets efficiently. The tool is adaptable to various sensors and ensures consistency when comparing images taken at different locations and times (Augustin et al., 2019).

SIAM uses prior knowledge to categorize reflectance values into specific spectral categories (Interdisciplinary Centre of Competence for Geoinformatics, Z-GIS, University of Salzburg and Spatial Services GmbH, n.d.) which can help estimating the accuracy of atmospheric corrections. Although SIAM requires TOA reflectance values, a thorough review of the relevant literature revealed that this approach has not yet been applied to BOA reflectance values.

The objective of this master's thesis is to examine and compare various atmospheric correction techniques on the basis of BOA calibrated Sentinel-2 images using spectral categories derived from the SIAM software based on knowledge-based methods to evaluate whether different methods produce similar results compared to each other and to TOA-based data and if not – to which extent and following which pattern atmospheric corrections influence SIAM results and where they introduce uncertainties.

2. Study objectives

The primary objective of this study is to assess the influence of different atmospheric correction techniques on SIAM-based land cover categorization across different regions and seasons. To achieve this goal, the research is structured into four main sections.

First, S2 L1C (TOA reflectance) data is downloaded from ESA’s official portal. The data is then processed before three atmospheric correction methods are applied to generate BOA reflectance products. This step establishes the basis for evaluating methodological differences.

Second, SIAM software is used to perform spectral categorization on both the uncorrected (TOA) und corrected (BOA) datasets in order to allow systematic cross-method, cross-region and cross-season evaluation.

Third, the results are systematically compared to capture methodological, spatial and temporal variability. Different metrics are derived to assess SIAM category distribution, inter-method classification consistency, semantic change severity and spatial patterns of disagreement across all methods. The results not only identify stable and unstable categories, but also demonstrate the magnitude, severity and direction of category shifts helping to reveal systematic biases.

Finally, the findings are synthesized to evaluate the suitability of atmospheric correction for SIAM-based applications and to formulate recommendations for practical use and future research.

The aims of this work are considered as satisfied when the data has been processed, the results have been evaluated and compared, and appropriate recommendations have been given.

3. Theory and concepts

The following chapter is structured around a progressive introduction of the main processes that describe the interaction between solar radiation, the atmosphere and the Earth's surface. First, fundamental physical principles underlying atmospheric phenomena are introduced in Chapter 3.1. These mainly include atmospheric scattering and absorption, which modify spectral characteristics of radiation travelling through the atmosphere. Additionally, the concepts of surface reflectance and radiance are outlined to clarify how surface properties influence the signal recorded by the satellite sensors. Finally, cloud and cloud shadow effects and their detection methods are introduced, as they represent a major source of uncertainty in remote sensing.

Building on this foundation, the theoretical basis of radiative transfer – the physical framework for atmospheric correction algorithms – is discussed in the next section. A simplified formulation of radiative transfer equation (RTE) is presented to explain how TOA measurements are transformed into estimates of BOA reflectance.

Next, the principles of topographic correction are introduced to explain how variations in terrain slope, surface orientation and elevation affect illumination and cause systematic distortions, especially in complex mountainous regions. Topographic correction methods aim to compensate for these effects by normalizing reflectance with respect to local illumination conditions.

Together, these components establish the physical and theoretical basis for following processing and analysis steps. By understanding the influence of atmospheric and topographic effects, the methodology enables a comprehensive assessment of their impact on SIAM's spectral categorization results across different environmental and seasonal conditions.

3.1. Physical principles

Before delving deeper into the specific physical principles which make an atmospheric correction of remote sensing data necessary in order to produce high quality BOA from TOA reflectance values, it is essential to define the terms reflectance and radiance.

Surface reflection refers to the amount of incident solar radiation reflected by the Earth, often depending on the incident or viewing angles and the wavelength influenced by the spectral and geometrical properties of the surface. A good example is the surface reflectance of a water body like an ocean. It varies not only depending on its water constitution (determined by the concentration of chlorophyll and other dissolved organic and inorganic particles), but also on the wind-induced surface roughness. And while spectral characteristics of a material or a surface can be measured with a spectroradiometer, its angular dependency is significantly more complex. Assuming a beam-like light and an ideal mirror-like surface, the incident and reflection angles are equal. The reflectance of an ideal rough planar surface, on the other hand, is equal at different viewing angles, which can be referred to as "Lambertian". However, real-world surfaces don't fit these two categories, their reflectance changes in response to incident and viewing geometries (Qu, 2018). This directional dependance is quantitively described by the Bidirectional Reflectance Distribution Function (BRDF), a more detailed explanation is provided in Chapter 3.1.2.

Unfortunately, surface reflectance – the true, intrinsic reflection properties of the Earth's surface – is not what is observed by the satellite sensors. Instead, satellites measure the radiance, which is the amount of backscattered electromagnetic energy at the top of the atmosphere, including not only the light reflected by the Earth's surface, but also the effects of the atmosphere as the light passes through (Qin et al., 2001). These atmospheric effects, such as scattering and absorption, will be discussed in more detail in the following chapter.

In other words, reflectance and radiance are closely related in the context of remote sensing, but they represent fundamentally different concepts. TOA radiance describes the raw signal received by the satellite sensor, whereas TOA reflectance is derived from this raw data through a series of corrections, including radiometric calibration, orthorectification and solar geometry normalization. This process is it what makes atmospheric correction necessary as atmospheric effects can contaminate the measurements and lead to an increased or decreased (TOA) reflectance as well as introduce some other unwanted effects like blurring, resulting in a reduced resolution and contrast and making the interpretation of data more difficult (Kaufman, 1984; Rahman and and Dedieu, 1994). In order to account for these effects, BOA reflectance takes the corrected TOA reflectance data as input and applies atmospheric correction. In the scope of this work, these correspond to Copernicus' S2 L1C and L2A products respectively (European Space Agency, 2025a). Although technically not exactly the same, BOA reflectance (model-based estimate) is often used as synonym for surface reflectance (physical reality) in remote sensing literature, as they typically describe the same corrected data. For consistency and simplicity, this study adopts this convention.

3.1.1. Scattering and absorption of radiation in the atmosphere

Referring back to the previous chapter, the atmosphere interacts with both – incoming and reflected radiation, mainly through the processes of scattering and absorption. While scattering refers to a redistribution of light in the atmosphere, some energy is transformed into other forms like heat through a process called absorption.

Different gases in the atmosphere absorb light in specific spectral bands. Best known for playing a crucial role in sustaining life on our planet is the absorption of UV light by ozone (O_3), while the absorption of infrared radiation by greenhouse gases like CO_2, CH_4, N_2O and water vapor contributes to the greenhouse effects. In the visible (VIS), near infrared (NIR) and near ultraviolet (UV) regions of the spectral range suspended particles called atmospheric aerosols – and mainly black carbon found in soot – account for the light absorption. Unlike gases that absorb at specific wavelengths, this kind of absorption is continuous, covering the whole visible spectrum and only weakly depending on wavelength. Despite representing a small fraction of atmospheric aerosols, light absorbing particles – depending on location – can be responsible for up to half of visibility reduction. Additionally, they can contribute to a brownish urban haze and sky discoloration (Horvath, 1993).

Similar to the absorption, scattering can also be divided into two main parts – scattering by small particles like gas molecules and scattering by similar or larger particles compared to the wavelength like dust particles or water droplets. For small particles, there is not much scattering variation with direction, the light is scattered evenly in all directions. This is usually referred to as Rayleigh scattering after Lord Rayleigh who was the first to describe this phenomenon in 1871, making it responsible for blue skies and red sunsets (Strutt (Lord Rayleigh), 1871; Young, 1982). Shorter wavelengths of visible light are scattered more easily compared to longer wavelengths. During the sunsets, the light travels longer distances causing the shortwave blue and violet portions of the spectrum to be scattered away, leaving only longer, reddish-orange light reaching the observer.

The bigger the particle, however, the more complex the scattering pattern becomes, with stronger scattering in certain directions. Moreover, the scattering pattern also additionally depends on the shape of the particle. (Bohren and Huffmann, 1983; Klassen, 1987). This type of scattering – typical for haze, clouds and dust – has been described by Gustav Mie in 1908 (Mie, 1908) and is known as Mie scattering. Compared to mostly symmetric, strongly wavelength-dependent Rayleigh scattering, Mie scattering is weakly wavelength dependent and has strong forward scattering characteristics.

In his study Rottman (2007) estimates, that globally averaged only around 9% of incident solar radiation is reflected by the Earth's surface. Approximately 49% are absorbed by the surface while the atmosphere scatters and reflects back 22% and absorbs around 20% (see Figure 1).

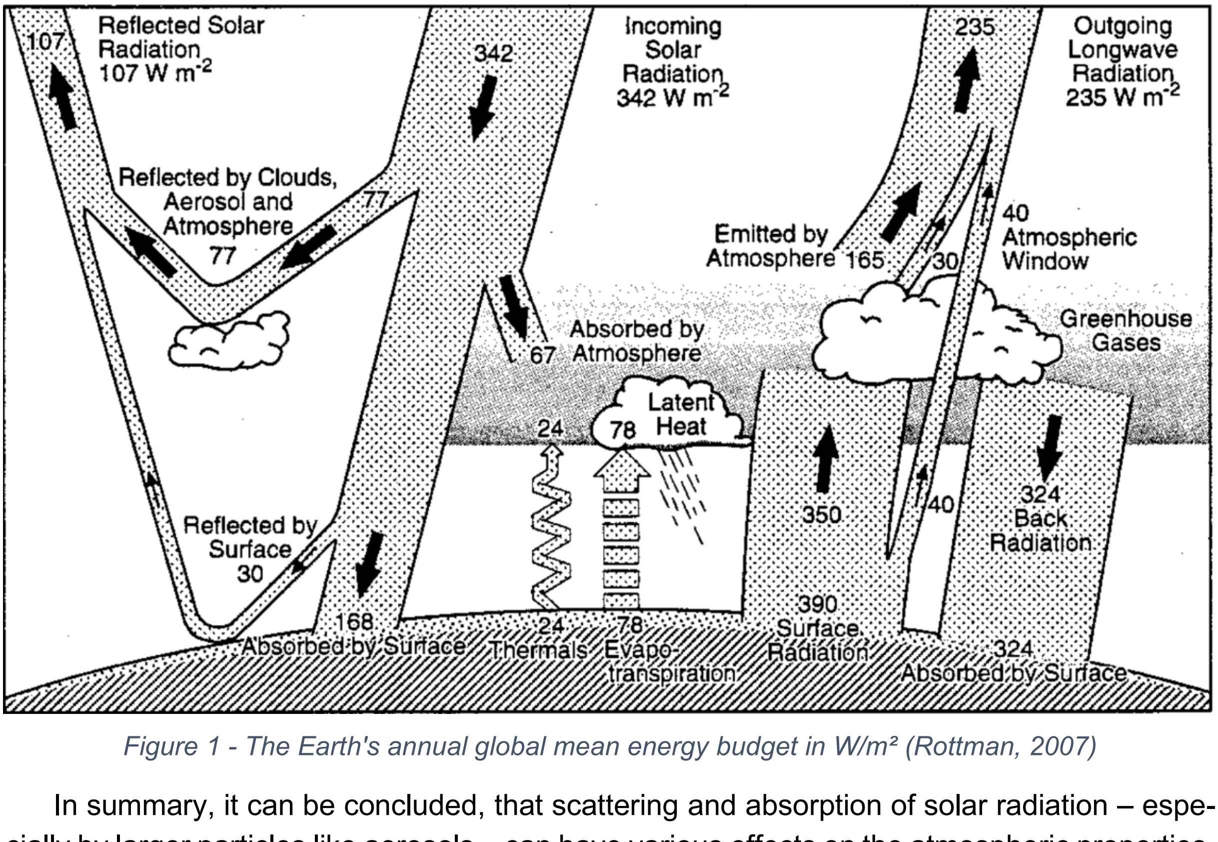

Figure 1 - The Earth's annual global mean energy budget in W/m² (Rottman, 2007)

In summary, it can be concluded, that scattering and absorption of solar radiation – especially by larger particles like aerosols – can have various effects on the atmospheric properties. It is therefore important to analyze their characteristics and investigate their variability, both – spatial and temporal – at scales ranging from local to planetary. The integrated measurement of aerosol distribution within the atmospheric column and thus – the extent to which aerosols attenuate light transmission from the Earth's surface to the top of the atmosphere, is referred to as Aerosol Optical Depth (AOD) or Aerosol Optical Thickness (AOT) (Wei et al., 2020). AOD must be distinguished from the Total Optical Depth (TOD), which includes not only AOD, but also the optical depth variations caused by Reileigh scattering and the absorption by atmospheric water vapor and other gases like O3 or NO2 (Bodhaine et al., 1999). In the context of atmospheric corrections, AOD and TOD will be discussed in more detail in Chapter 3.2.

3.1.2. Surface reflectance

The previous chapters described how the atmosphere influences the solar radiation passing through it and thus distorts the radiance received by satellite sensors. However, the atmosphere is not solely responsible for this bias – reflectance of a surface also depends on its intrinsic properties. As stated previously, real-world surfaces are neither mirror-like, reflecting the radiation at the same angle as receiving it, nor are they “Lambertian”, where the reflectance is independent of direction. Natural surfaces are anisotropic – soil, water and vegetation reflect light differently depending on the illumination direction as well as the viewing direction described by the solar and sensor zenith and azimuth angles. This angular dependence of surface reflectance is described by BRDF. BRDF effects are present across all spectral bands in satellite imagery and can introduce substantial noise in high-precision applications (Shen et al., 2025). And although the ESA is claiming the same viewing angles for every revisit for the nominal Sentinel-2 configuration (Sentinel-2B/2C) (European Space Agency, 2025b), the seasonal changes in the Sun’s position alone – the Sun is higher in summer and lower in winter – is enough to cause BRDF-related reflectance variations unrelated to an actual surface change.

Besides BRDF, there is also another effect which needs to be accounted for to get accurate reflectance results. Due to the surface anisotropy, horizontal radiation fluxes can develop in the atmosphere. After subsequent scattering, the photons reflected by brighter areas can eventually contaminate adjacent darker pixels (Otterman et al., 1980). In the literature, this phenomenon is referred to as adjacency effect. This radiation transfer results in a blurred image with a reduced apparent contrast (Mekler and Kaufman, 1980). Practically, it means that scattered photons from snow, white sand or clouds can artificially increase the reflectance of a darker water body, vegetation or snow-free soil. It is important to understand, that adjacency effect is systematic – it always decreases the measured reflectance of bright areas while increasing it for dark surfaces and thus should be specifically accounted for in remote sensing for dark or bright land targets (Lyapustin and Kaufman, 2001).

3.1.3. Cloud and shadow effects

Aside from the beforementioned adjacency effects, clouds and cloud shadows can strongly influence the radiance measured by a satellite, even if they only represent a small portion of the scene surface – they either conceal or distort the surface signal entirely or partially, making the retrieval of missing data physically impossible. Thus, it is important to detect clouds and cloud shadows in order to exclude their signals from the surface analysis (Le Hégarat-Mascle and André, 2009).

It is not uncommon to confuse bright surfaces with clouds, but cloud detection becomes even more challenging in case of semi-transparent clouds, where the observed surface reflectance is a result of land and cloud signals mixed together. Moreover, cloud shadows often have similar reflectance properties to water, burnt areas or other shadows, which leads to even more confusion (Baetens et al., 2019). Consequently, a reliable cloud and cloud shadow masking algorithm represents a fundamental step in any workflow aiming at deriving meaningful surface reflectance products from satellite imagery.

Over the years, a variety of cloud detection algorithms have been developed for remote sensing purposes. In terms of conceptual strategies, they can loosely be grouped into four categories: spectral thresholding, physical radiative modelling, textural or morphological analysis and machine learning approaches.

Spectral thresholding utilizes threshold rules for reflectance or band ratios to create checks against a set of conditions, such as:

- surface reflectance is low compared to a higher cloud reflectance in the VIS range.
- in the VIS and NIR ranges, clouds are usually white (Baetens et al., 2019).
- a threshold on the 1.38-μm water vapor absorption band. This band absorbs all light in the lower layers of the atmosphere (Gao et al., 1993) leaving only high-altitude objects, which are usually clouds, but can also represent mountaintops (Ben-Dor, 1994). In case of cirrus clouds, it is not possible to distinguish them from ground above 3000m altitude, because the mountaintops this high are just as bright or even brighter. For this reason, the cloud mask for cirrus clouds is only calculated below 3000m (European Space Agency, 2025c).
- in the shortwave infrared range (SWIR), clouds have a much higher reflectance than snow (Dozier, 1989).

Some typical spectral signatures of clouds, bare soil (desert) and fresh, fine snow are shown in Figure 2.

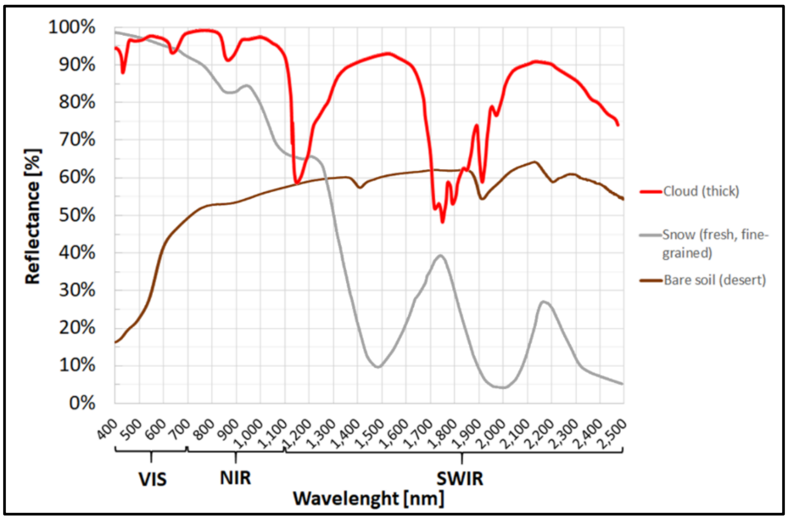

Figure 2 - Typical spectral signatures of thick clouds, fresh snow and bare soil in the visible, near infrared and shortwave infrared ranges (adapted from GEOLab, 2021)

Unlike the spectral thresholding, which is applying fixed numerical thresholds to the reflectance, the physical methods utilize the underlying absorption and scattering processes to determine whether or not an observation equals the predicted, cloud-free TOA reflectance. For this purpose, a time series of the same water vapor absorption band can be used. The simulated TOA reflectance is then compared to the measured one. A significant positive deviation indicates the presence of a cirrus cloud (Qiu et al., 2020). The prediction modelling itself is achieved by using RTE and additional atmospheric information, such as water vapor and aerosol profiles, solar-sensor geometry and surface elevation. This will be discussed in more detail in Chapter 3.2.

Besides the spectral and physical properties of clouds, their texture, shape and size can also be used to detect them. The key concepts for this morphological analysis are the dilation and erosion operators. In image processing, they are typically used for modifying the structure of objects, especially in case of binary or greyscale images, using a structuring element. In simple terms, in case of dilation, the value of a pixel is replaced with the maximum value found in its neighborhood, defined by the structuring element, such as a rectangle, a circle or an octagon. This way dilation "grows" or thickens objects but can also be used to fill holes or connect parts in an image. The opposite operation is called erosion. Here, the value of a pixel becomes the minimum within its neighborhood, causing regions to "shrink", removing the noise by filtering out small objects or leading to thinner boundaries (Haralick et al., 1987).

In practice, morphology-based approach is being used to distinguish whether a bright surface can represent a cloud, which tends to have a shape with a low perimeter-to-area ratio and a large size. Bright urban areas and mountain snow, on the other hand, are mostly represented by isolated pixels, pixel lines or rectangles, having a much larger perimeter-to-area ratio. These objects can be removed by erosion using a circular structuring element. After that, dilation is performed to recover the initial cloud shape (Figure 3). For "round" clouds, one dilation operation can be enough, but needs to be repeated multiple times for clouds with sharp boundaries (Qiu et al., 2019).

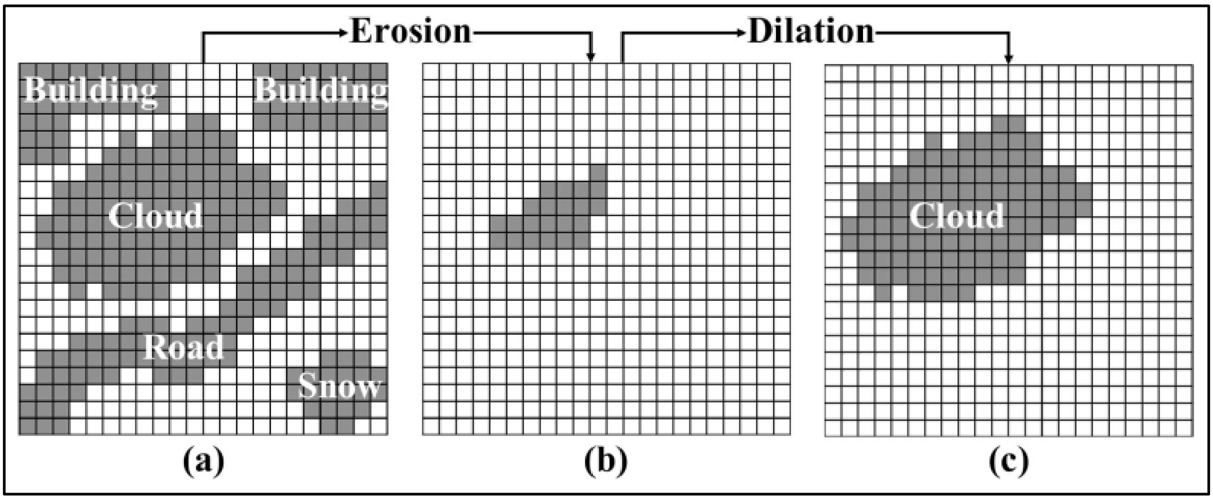

Figure 3 - Example of erosion and dilation operations with a radius of 3 pixels. (a) Potential false positive cloud layer. (b) Remaining pixels after erosion. (c) Cloud recovered by dilation (Qiu et al., 2019).

Based on erosion and dilation, mathematical morphology (MM) with its area opening and closing techniques is another widely used tool in remote sensing applications. Both techniques make use of the fact that shadows reduce the illumination and contrast of an area, lowering the brightness and behaving as minimum in digital images, while clouds have a high reflectance and represent the maximum due to non-selective solar scattering. In a grey image, where the pixel values are represented as heights on a topographical surface, shadows would be visually represented by valleys and clouds – by peaks (Figure 4). Utilizing this characteristics, peaks and valleys can be reduced or eliminated by applying opening and closing operations (Statella and Erivaldo, 2008).

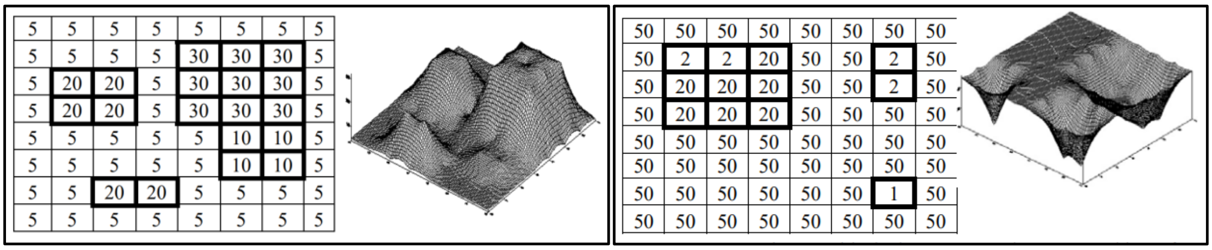

Figure 4 - Grey image with clouds (left - peaks) and shadows (right - valleys) presented as topographic surface (Statella and Erivaldo, 2008).

Lastly, there are a variety of machine learning and hybrid applications for automated cloud detection. The issue with machine learning approach is that it heavily relies on the size and the quality of the training and validation data. This is the main reason they mostly underperform compared to classical methods. However, their ability to quickly improve and evolve, combined with growing availability and amount of good quality samples, is what is making machine learning so promising for the future (Sanchez et al., 2020; Zupanc, 2020).

Comparing all the methods to find the best approach is not always reasonable due to versatile landscapes, different sensors, available data and lots of other factors. Instead, users should concentrate on the intended use and consider the strengths and weaknesses of each method before making their decision.

3.2. Radiative transfer theory

Radiative transfer theory describes the physical laws controlling the propagation of electromagnetic radiation through a medium such as the Earth's atmosphere. In optical remote sensing this theory provides the fundamental framework for understanding how solar radiation is modified by atmospheric processes described in previous chapters before and after interaction with the surface of the Earth. The mathematical description of radiative transfer originates from studies in astrophysics and atmospheric physics and has been adapted for terrestrial remote sensing applications (Chandrasekhar, 1960; V. V. Sobolev, 1975).

The RTE provides a general description of how radiance changes along its path withing the atmosphere. Referring to the previous chapters, in the surface-atmosphere system, radiation propagating from atmosphere's top boundary towards the surface gets scattered by molecules and particles and absorbed by atmospheric gases. After being reflected by the surface, on its way upwards toward the sensor, it gets again modified by the same atmospheric processes. As a result, the radiance measured by the satellite at the top of the atmosphere contains both – surface-reflected and atmosphere-generated components. This relationship can be expressed in simplified form as:

$$L_{TOA} = L_{path} + T_{\uparrow}\rho_s \frac{E_0 T_{\downarrow} cos\theta_s}{\pi}$$

Where:

- L_{TOA} is the measured radiance
- L_{path} is the atmospheric path radiance
- $T_{\downarrow}$ and $T_{\uparrow}$ are the downward and upward atmospheric transmittances
- ρ_s is the surface reflectance
- E_0 is the extraterrestrial solar irradiance
- θ_s is the solar zenith angle
- π is the radiance-irradiance conversion factor

The measured radiance L_{TOA} is the total outgoing radiative signal in the given spectral band and viewing direction. Is it the quantity which is directly measured by the satellite's sensor and the basis for further processing and analysis. L_{path} is the radiance generated within the atmosphere without interacting with the surface and originates mainly from scattering processes involving molecules and aerosols. The atmospheric transmittances $T_{\downarrow}$ and $T_{\uparrow}$ describe the fractions of incoming solar radiation, in other words – they determine the attenuation caused by scattering and absorption. These values depend on wavelength, atmospheric composition and solar zenith angle (SZA). ρ_s is the surface reflectance – the actual value most atmospheric correction algorithms are aimed to retrieve by removing atmospheric effects. It depends on material properties such as vegetation structure, soil composition, moisture content and surface roughness. E_0 is the amount of available solar energy outside Earth's atmosphere and depends on spectral characteristics of the Sun and the Earth-Sun distance. θ_s is the angle between the Sun and the local vertical. When the Sun is high in the sky, SZA is low and surface illumination is strong. At low Sun elevations, this term decreases, reducing incoming energy and increasing sensitivity to atmospheric effects. Finally, π is the conversion factor from hemispherical irradiance at the surface to directional radiance observed by the sensor. For practical reasons, this term assumes a Lambertian surface. The described formula represents the combined effects of atmospheric and surface components on the measured signal (Vermote et al., 1997).

The combined effect of atmospheric scattering and absorption on radiation is referred to as optical depth. The TOD consists of contributions from molecular scattering, aerosol scattering and gaseous absorption. Whereas AOD or AOT only describe the contribution of aerosol particles and is the key component for understanding how aerosols impact the transmission of light between the surface and the top of atmosphere (Li et al., 2009; Wei et al., 2020).

Due to its complexity and dependence on many interacting variables, the full RTE cannot be solved analytically under realistic atmospheric conditions. Instead, simplified solutions are typically derived under a set of assumptions regarding atmospheric structure, surface reflectance behavior and illumination geometry like horizontal homogeneity, Lambertian surface reflection or simplified geometry to name a few. These assumptions reduce complexity and allow practical implementation but introduce deviations from real atmospheric behavior.

3.3. Topographic correction

Topographic effects are a major source of radiometric variability of the signal in optical remote sensing, especially in mountainous regions. Compared to a flat surface, slopes oriented from the Sun will appear darker, while the ones oriented towards it will be brighter, even if the surface cover is the same. Consequently, topographic correction is an important preprocessing step, aimed at compensating for these effects, especially for mountainous regions (Riano et al., 2003; Richter et al., 2009). In other words, the variation in reflectance, if uncorrected, can be misinterpreted as a change in surface properties, rather than surface geometry. Topographic correction aims at reducing this variability to normalize the reflectance as if the terrain was flat or uniformly illuminated. Therefore, various correction methods have been developed in order to reduce or mitigate the topographic influence but discussing them in detail would be outside of this study's scope. Instead, the key concepts actually used in this work will be shortly explained below.

A good assessment of the most frequently used methods has been given by Riano et al. (2003). The authors state that topographic correction approaches can generally be divided into simple ratio-based approaches, which do not rely on additional data, and methods based on modelling illumination, which require digital elevation models (DEM). The ratio-based methods rely on the assumption that the illumination affects the reflectance in different bands in the same way. Therefore, it can be compensated for terrain-induced effects by dividing the reflectance values of two bands. This is true for the direct sunlight, where the incident angles are the same for all wavelengths, but not for diffuse irradiance, where the light has been scattered by the atmosphere before reaching the surface, as described using the example of a sunset in Chapter 3.1.1. Therefore, using band ratios for topographic correction cannot fully compensate for topographic effects.

The second group – illumination-based – methods, use a DEM, ideally with the same spatial resolution as the image being corrected. These approaches try to model the illumination by computing the incident angle, which is the angle between the incoming solar radiation and the normal vector of the terrain surface. In simple terms, this angle defines how much direct solar radiation reaches each pixel. Once the illumination conditions have been computed for each pixel, the flat-normalized reflectance can be estimated. The related methods can broadly be grouped into Lambertian and Non-Lambertian categories. Lambertian methods assume the surface reflectance to be independent from the observation and incident angles. They ignore the wavelength-dependent contribution of the diffuse irradiance as described above, which leads to overcorrected reflectance, especially in poorly illuminated areas. The more realistic non-Lambertian approaches account for the directional nature of surface reflectance, known as BRDF (discussed in Chapter 3.1.2), by incorporating a correction factor based on illumination conditions and allowing different behavior for different bands, which leads to less overcorrection, especially in shaded areas, and more stable reflectance values by preserving the natural brightness differences (Riano et al., 2003).

4. Input data

The study was conducted using Sentinel-2 satellite imagery, acquired mostly over Austria between May 2019 and October 2024. To ensure a wide variety of climatic, topographic and land cover conditions, four representative regions were selected:

- **Alpine valleys** - covering the region of Tirol as well as southern part of Bavaria, Germany, is characterized by narrow alpine valleys between high mountains, resulting in a strong elevation deviation and causing complex terrain-induced shadow and illumination effects and heterogeneous atmospheric conditions. Land cover is dominated by alpine grasslands and forests and small-scale agriculture and urban areas, including the city of Innsbruck. At higher elevations, seasonal snow covers are common from late autumn to late spring or even summer. The complex atmosphere and aerosol distribution lead to frequent cloud formation.

- **High Alps** - encompasses the high alpine zone with elevations above 2000m and a persistent snow cover outside the summer months. This area is located to the east of the Alpine valleys. The conditions in this zone are similar to that of the Alpine valleys, but with bigger extremes – the surface reflectance is higher due to snow cover, thinner air and a higher solar exposure.

- **Pre-Alps** - represents a transitional landscape between the Alps in the south and flat regions in the north, partly covering south-east part of Bavaria, Germany. The terrain is less complex, with fewer and less extreme slopes and stable atmospheric and illumination conditions compared to the High Alps and Alpine valleys regions. Snow occurs periodically during the winter months. The landscape consists of agriculture areas, forests, grasslands and some urban areas, including the city of Salzburg.

- **Eastern planes** - dominated by flat plains with minimal elevation variations and uniform illumination conditions. There is less snow with shorter duration, usually during the winter months. Due to the stronger influence of the continental climate, the region can experience dry periods and increased aerosol concentrations. The land cover mostly consists of agriculture areas and covers big parts of western Hungary.

This region selection allows for a better assessment of the correction methods due to a high variety of topographic, atmospheric and illumination conditions. Figure 5 shows the selected regions arranged from left to right in the order described above.

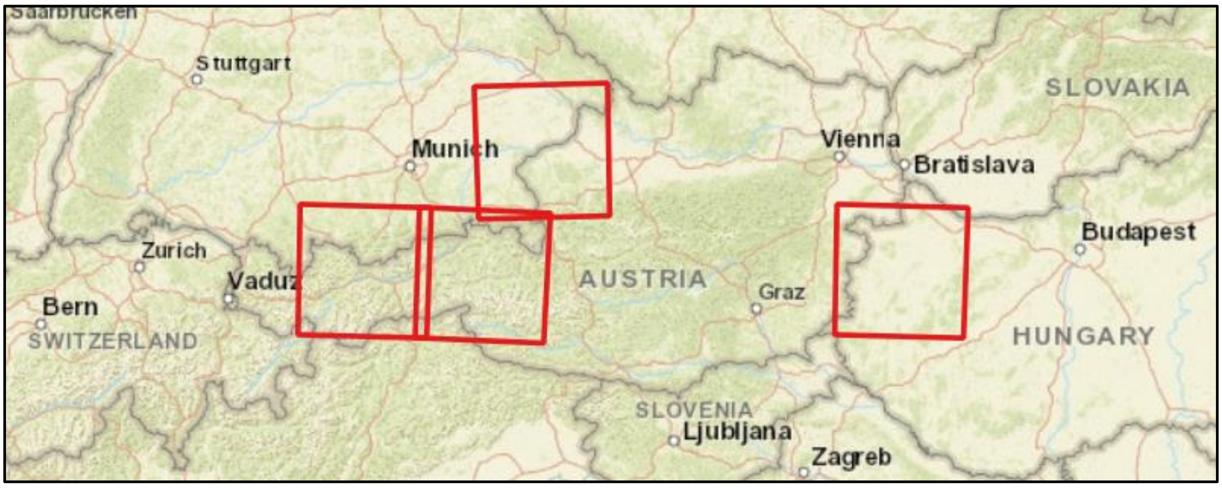

Figure 5 - Study regions (from left to right): Alpine valleys, High Alps, Pre-Alps, Eastern planes

Ideally, the regions would be better distributed spatially, and the respected images acquired within the same dates, but due to limitations in data availability and cloud cover constraints, such a strict selection was not possible. To address this issue, four months were chosen to represent the main seasons reflecting key vegetation states and atmospheric conditions relevant for land cover classification:

- **Spring** (May): the vegetation is actively greening, snow starts to melt or has melted already, except at high elevations.
- **Summer** (July): peak vegetation and agriculture activity, generally clearer atmospheric conditions, long daylight duration, almost no snow, even at higher elevations.
- **Autumn** (October): land-use changes like harvests and vegetation senescence, characterized by chlorophyll breakdown due to shorter days, cooler temperatures or nutrient deficiencies.
- **Winter** (January): presumably snow cover, relatively stable atmospheric conditions, deciduous trees lost their leaves.

By prioritizing seasonal consistency and low cloud coverage rather than focusing on identical acquisition dates, the study aims to ensure that the observed reflectance differences and spectral categorization results are primarily a result of seasonal and atmospheric variations. Therefore, images acquired from different years were allowed when necessary.

4.1. Satellite imagery

Sentinel-2 products (except Level-1B) are distributed using a tiling system of orthorectified images projected onto the Universal Transversal Mercator (UTM) reference system. Although UTM is using a 100 km step for subdividing the Earth into tiles, 110 km x 110 km areas are used for Sentinel-2 in order to ensure a large overlap with the neighboring tiles, each identified by its unique tile ID. These image products retain the native (10 m, 20 m, 60 m) band resolutions by default (European Space Agency, 2025a). The red boundaries shown in Figure 5 above correspond exactly to these tile IDs. Table 1 shows the acquisition date, the tile ID, the cloud cover percentage and the SZA of the S2 L1C datasets used in this study for each region and season, downloaded from ESA's Copernicus Browser (European Space Agency, n.d.).

Table 1 - Sentinel-2 (L1C) data used for each study region and season

Region	Season	Acquisition Date	Sentinel-2 Tile ID	Cloud Cover (%)	Solar zenith angle
Alpine valleys	Spring	31.05.2021	T32TPT	0.02	~ 27°
	Summer	15.07.2023	T32TPT	0.20	~ 28°
	Autumn	13.10.2023	T32TPT	1.08	~ 56°
	Winter	26.01.2022	T32TPT	0.00	~ 67°
High Alps	Spring	24.05.2019	T32TQT	5.27	~ 28°
	Summer	23.07.2019	T32TQT	0.34	~ 30°
	Autumn	15.10.2021	T32TQT	1.40	~ 57°
	Winter	28.01.2024	T32TQT	0.13	~ 67°
Pre-Alps	Spring	28.05.2023	T33UUP	0.49	~ 28°
	Summer	21.07.2024	T33UUP	0.00	~ 30°
	Autumn	09.10.2024	T33UUP	0.00	~ 55°
	Winter	28.01.2024	T33UUP	0.06	~ 68°
Eastern planes	Spring	22.05.2023	T33TXN	1.70	~ 29°
	Summer	30.07.2024	T33TXN	0.00	~ 32°
	Autumn	14.10.2023	T33TXN	0.00	~ 56°
	Winter	23.01.2020	T33TXN	0.54	~ 68°

Sentinel-2 products follow a strict naming convention which allows an unambiguous identification and reproducibility of each dataset. Thus, the file with the filename

S2B_MSIL1C_20220126T102209_N0510_R065_T32TPT_20240506T060628.SAFE

can be broken down into following components (alphanumeric upper-case characters, separated by underscores):

- **S2B** Mission ID / Satellite platform (S2A/S2B)
- **MSIL1C** Product level (L1C/L2A)
- **20220126T102209** Sensing date and time
- **N0510** Processing baseline / Software version
- **R065** Relative orbit number
- **T32TPT** Tile number filed
- **20240506T060628** Product generation date and time
- **SAFE** Product format (**S**tandard **A**rchive **F**ormat for **E**urope)

For the full list of S2 L1C datasets used in this study, please refer to Appendix A – Table A1.

The SAFE file contains a collection of following components:

- A **product metadata XML** file containing information about its overall structure and properties.
- An **INSPIRE XML** file following the INSPIRE Metadata regulation.
- A **manifest.safe** file summarizing the product content and referencing the included components.

- A **GRANULE** subfolder containing the actual image data in JPEG2000 format, along with associated quality indicators.
- A **DATASTRIP** subfolder, which contains acquisition information, such as sensor configuration, calibration and timing parameters etc.
- An (optional) **AUX_DATA** subfolder with auxiliary datasets used during the processing.
- A **rep_info** subfolder, which includes the XML Schema Definition (XSD) describing the structure and allowed content of the product.
- A **HTML** subfolder with visualization files for a simplified visual inspection of the product contents through a web browser.

This folder structure, described above and shown in Figure 6, refers to S2 L1C and L2A products only. Other products, such as L0, L1A or L1B are either not released at all or only released to expert users on request (European Space Agency, 2025a).

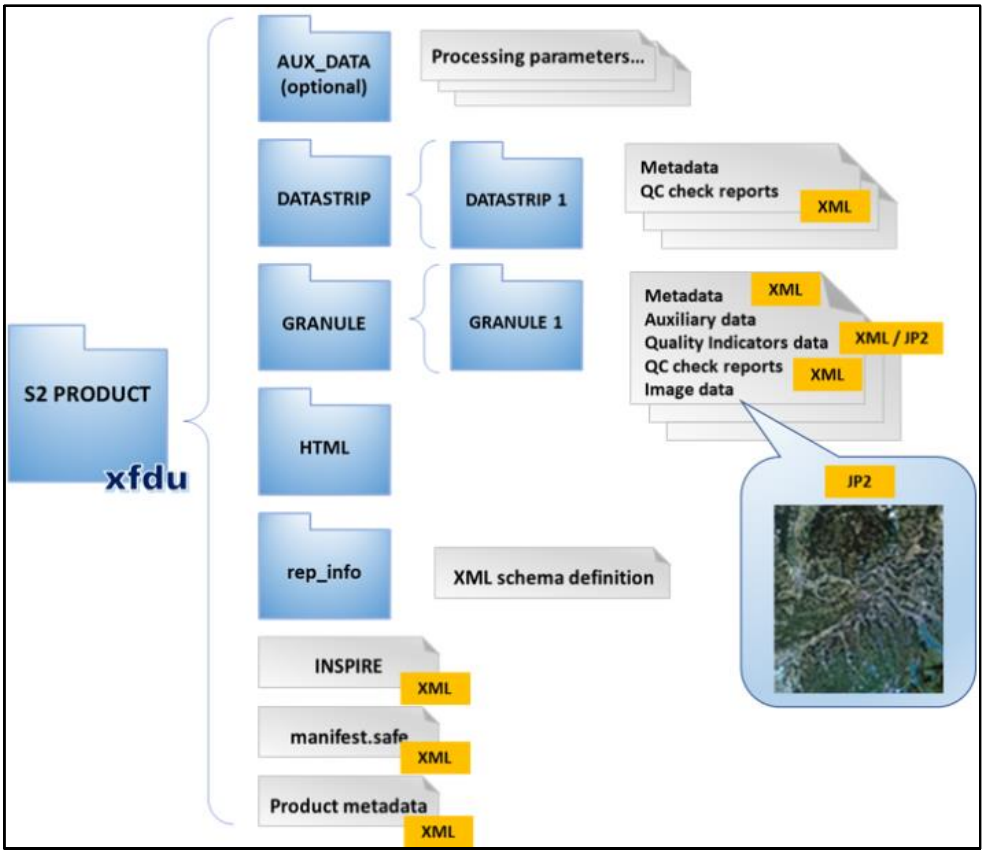

Figure 6 - SAFE file content of a Sentinel-2 product (European Space Agency, 2025a)

To ensure maximum consistency and the best comparability of this study's results, ideally, all Sentinel-2 products would have been acquired by the same satellite platform (through the same Sentinel-2 mission). Unfortunately, due to the specifications and limitations described in Chapter 4, both – S2A and S2B missions had to be used. Although S2A was positioned to have a 36° phase offset to S2B (as shown in Figure 7), which in turn is separated from S2C by 180°, they still occupy the same orbit, observe the same locations under very similar viewing conditions and use the same sensors (European Space Agency, 2025b). In the context of this work, it means that platform-related geometric or radiometric differences have negligible effects compared to the atmospheric and seasonal variability.

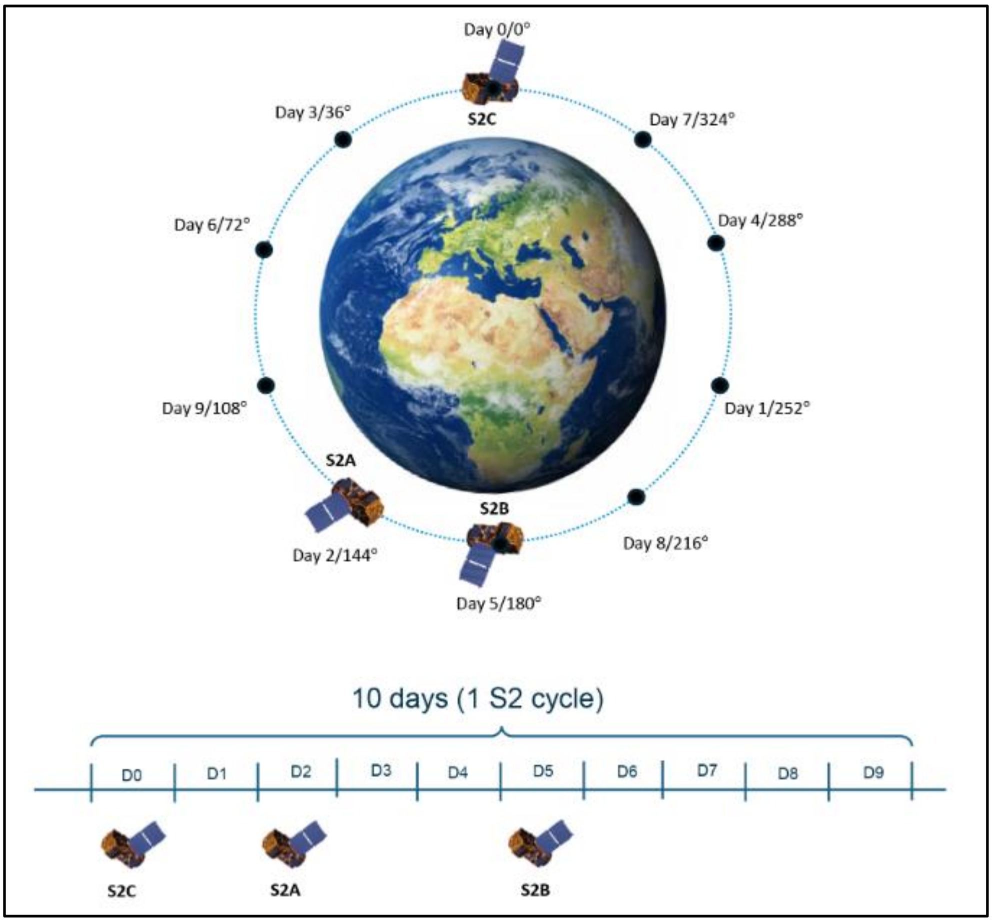

Figure 7 - Distribution of Sentinel-2 satellites over the mission orbit (European Space Agency, 2025b)

With its Multispectral Imager (MSI) sensor, Sentinel-2 delivers 13 spectral bands ranging between VIS and very near infrared (VNIR) and SWIR and between 10m and 60m resolution (10m, 20m and 60m pixel size). Table 2 shows the details for each band as well as the differences between S2A and S2B (European Space Agency, 2025b).

Table 2 - Spectral information per band for S2A and S2B (European Space Agency, 2025b)

Band	Resolution (m)	S2A		S2B		Description
		Wavelength (nm)	Bandwidth (nm)	Wavelength (nm)	Bandwidth (nm)	
B1	60	442.7	20	442.2	20	Ultra blue
B2	10	492.7	64	492.3	65	Blue
B3	10	559.8	35	558.9	35	Green
B4	10	664.6	30	664.9	31	Red
B5	20	704.1	14	703.8	15	Red-edge 1
B6	20	740.5	14	739.1	14	Red-edge 2
B7	20	782.8	20	779.9	20	Red-edge 3
B8	10	832.8	118	832.9	115	NIR
B8a	20	864.7	20	864.0	20	Narrow NIR
B9	60	945.1	20	943.2	20	Water vapor
B10	60	1373.5	30	1376.9	30	Cirrus
B11	20	1613.7	88	1610.4	93	SWIR 1
B12	20	2202.4	179	2185.7	181	SWIR 2

The differences only have a magnitude of a few tens to a few nanometers, which lies well within the bandwidth of each filter (e.g., B1 bandwidth ≈ 20 nm, B2 bandwidth ≈ 64 nm etc.). Thus, except for high-accuracy radiometric work, the two satellites can be treated as having identical band centres. This information is easily accessible inside the product metadata xml file mentioned above and can be used for analyses if needed.

4.2. Atmospheric properties and aerosol products

The importance of an accurate characterization of atmospheric properties for atmospheric correction has been already highlighted in the previous chapters. Especially the key parameters like the total column water vapor, ozone concentration, surface pressure and AOT play a crucial role here as they affect the absorption and scattering processes of radiation travelling through the atmosphere. Some atmospheric properties and aerosol parameters like the water vapor content or AOT can be retrieved directly from satellite imagery.

For instance, for water vapor retrieval ESA's Sen2Cor processor uses a technique called Atmospheric Pre-corrected Differential Absorption algorithm (APDA) (Schläpfer et al., 1998), which is derived from simplified RTEs, on Sentinel-2 bands B8a and B9. B8a is located in a so-called atmospheric window region, which means minimal atmospheric absorption, and thus serves as a reference channel. B9 lies in a water absorption region and serves as a measurement channel. The depth of absorption between the two bands is then a measure of the amount of water vapor present in the atmospheric column (Main-Knorn et al., 2015).

AOT can be retrieved using the Dark Dense Vegetation (DDV) algorithm (Kaufman and Sendra, 1988). It is built around the observation that dense vegetation has a low and spectrally predictable reflectance characteristics. It absorbs strongly in red (B4) and blue (B2) bands while also being affected by aerosol scattering. However, the reflectance in the B12 SWIR band is much less sensitive to these effects, which allows an estimation of the expected surface reflectance. The difference between the expected and the observed reflectance is then assumed to be the result of the scattering effects introduced by atmospheric aerosols (Main-Knorn et al., 2015).

It can be seen that approaches like these are based on assumptions and subject to certain limitations, like simplified RTEs in case of water vapor estimation or the dependence on a vegetation cover in case of AOT retrieval. Additionally, some atmosphere constituents like ozone simply cannot be directly retrieved from Sentinel-2 images, which spectral bands are not optimized for the specific features of ozone. In this case, data from external sources needs to be used. Within the Copernicus Programme, Sentinel-5 Precursor (Sentinel-5P) mission with its TROPOspheric Monitoring Instrument (TROPOMI), dedicated to air pollution monitoring, is specifically designed to cover the UV, VIS, NIR and SWIR wavelengths and thus capable of retrieving total ozone column by using ozone absorption characteristics in the UV bands (European Space Agency, 2020). These and other satellite-based observations like NASA's (National Aeronautics and Space Administration) Moderate Resolution Imaging Spectroradiometer (MODIS) instrument aboard the Terra and Aqua satellites (National Aeronautics and Space Administration, n.d.), combined with ground-based networks and numerical atmospheric models in a process known as assimilation, can be obtained through specialized services like Copernicus Atmosphere Monitoring System (CAMS) implemented by the European Centre for Medium-Range Weather Forecasts (ECMWF) (European Centre for Medium-Range Weather Forecasts, 2022) or the Modern-Era Retrospective analysis for Research and Applications, Version 2 (MERRA-2), implemented by NASA's Global Modelling and Assimilation Office (GMAO) (Global Modeling and Assimilation Office, n.d.).

For this study, CAMS was chosen over MERRA-2 as a primary source of atmospheric information for several reasons. First, it was implemented on behalf of the European Union and has a strong focus on, and more detailed regional atmospheric data of Europe (European Centre for Medium-Range Weather Forecasts, 2016, 2017, 2022), which makes it the ideal data source for this work. Second, CAMS is part of the Copernicus Programme and thus belongs to the same data ecosystem as the other Sentinel-2 products used in this study. In fact, it is even embedded in L1C and L2A products and is used as a fallback solution for atmospheric correction in case there are not enough DDV pixels in the image (European Space Agency, 2025c). And finally, the decision for CAMS was made based on personal convenience as it was considered to have a much more user-friendly download process, both – per API access and web interface. It is important to mention that in contrary to the embedded datasets, this is a so-called EAC4 (ECMWF Atmospheric Composition Reanalysis 4) data, retrospectively assimilated from observations and atmospheric models to ensure a higher accuracy and temporal consistency (Copernicus Atmosphere Monitoring Service, 2020; Inness et al., 2019).

4.3. Digital elevation model

Three DEMs were considered for cloud and cloud shadow detection, atmospheric and topographic corrections in this study, namely SRTM (Shuttle Radar Topography Mission), ASTER GDEM (Advanced Spaceborne Thermal Emission and Reflection Radiometer Global

Digital Elevation Model) and GLO-30 (Copernicus DEM), following the recommendation in FORCE (Framework for Operational Radiometric Correction and Environmental monitoring) documentation (Frantz, 2020b). FORCE is one of the correction methods in the context of this research and will be discussed in detail in Chapter 5.2. For multiple reasons the final choice fell on GLO-30 DEM. First, multiple studies rank GLO-30 among the most accurate 30m elevation models compared to other global products like ASTER DGEM and SRTM (del Rosario González-Moradas et al., 2023; Meadows et al., 2024; Simard et al., 2024). Second, it is yet another product within the Copernicus data ecosystem alongside Sentinel-2 and CAMS products and is used within the Sentinel-2 processing baseline (European Space Agency, 2025c). Using the same DEM for different correction methods ensures methodological consistency. And finally, DEM data from SRTM and ASTER comes in 1° tiles (NASA/METI/AIST/Japan Spacesystems and U.S./Japan ASTER Science Team, 2019; United States Geological Survey, 2018) while GLO-30 is providing a seamless global product (Copernicus Data Space Ecosystem, n.d.). This means that ASTER and SRTM GDEM require a preprocessing step called mosaicking in order to "merge" tiles to obtain continuous spatial coverage for larger study areas, therefore increasing the workflow complexity and the risk of artifacts.

5. Methodology

The previous chapters introduced the radiance and reflectance concepts, explained the role of atmospheric constituents, aerosols, clouds and cloud shadows, surface elevation and illumination conditions for atmospheric effects like scattering and absorption, introduced different methods of data retrieval in order to mitigate these effects establishing the physical background and data considerations for an accurate and successful atmospheric and topographic correction of Sentinel-2 imagery. Building on this foundation, this chapter describes the algorithmic implementation of these concepts across different types of practical processing systems like Sen2Cor (Sentinel-2 Correction), FORCE (Framework for Operational Radiometric Correction for Environmental Monitoring) and Py6S (Python interface for Second Simulation of the Satellite Signal in the Solar Spectrum). It provides a structured overview of the conceptual design and explains how different correction algorithms address the same physical problems without describing implementation details. Detailed descriptions of each methods software implementation, parametrization, processing steps, strengths and weaknesses will be presented in the subsequent method-specific chapters.

Sen2Cor, FORCE and Py6S differ fundamentally in their design philosophies. Sen2Cor is designed as an operational processor for performing atmospheric corrections of uncorrected Sentinel-2 data. FORCE, in contrast, is intended to serve as a flexible processing engine for mass-generation of analysis ready data (ARD), capable of large-area and time-series-based analysis, natively supporting Sentinel-2 and Landsat data. Py6S is a Python interface built to simplify and add new features to the 6S Radiative Transfer Model, which was initially processing cryptic input and output files. These design choices have an impact on the degree of automation, user interaction and parameter customization and exhibit distinct strengths and limitations in regard to adaptability, robustness and computational complexity.

Although all applied methods are based on radiative transfer theory, they differ in the way how atmospheric and aerosol information is incorporated into the correction process. Sen2Cor primarily relies on pre-computed LUTs (Lookup Table) for atmospheric parameters and image-derived aerosol data with some fallback options using external sources. FORCE is designed to either integrate externally provided atmospheric and aerosol products or estimate them using a physically based, image-driven approach, while Py6S gives the user a choice of either explicitly prescribing the parameters or using external sources. The chosen approach determines the effectiveness of atmospheric correction, especially in case of limited reference targets or challenging atmospheric conditions.

BRDF and adjacency effects are also handled differently. Sen2Cor performs approximate, empirical corrections for both effects by using simplified rules to reduce the brightness variations caused by viewing angles and neighboring pixels. FORCE handles adjacency in a more physics-based manner, deriving it from radiative transfer theory and is capable of accounting for angular effects to simulate a directly overhead view and produce a physical Nadir BRDF-Adjusted Reflectance (NBAR). Finally, Py6S also allows physical BRDF modeling, but does not have a built-in adjacency correction capability.

In regard to cloud and cloud shadows, Sen2Cor's image-based and Sentinel-2 focused detection algorithm is mandatory, it is automatically performed as part of L2A processing. FORCE users can optionally perform cloud detection by choosing between an internal algorithm and external cloud mask products. Py6S is designed to simulate atmospheric effects for already valid, clear-sky, pixels. It does not include any internal cloud and cloud shadow capabilities and so is fully relying on externally provided masks. All three methods use cloud and cloud shadow masks mainly to exclude contaminated pixels from atmospheric correction.

Another difference across the three methods is how surface elevation and topography are treated. All three account for the terrain height and adjust the absorption and scattering processes accordingly, however, only Sen2Cor and FORCE correct the terrain-induced illumination. While doing so, Sen2Cor focuses more on the Sun-surface geometry while FORCE is following a more physically consistent approach using radiative transfer theory to calculate per-pixel corrections across the spectrum. To represent the elevation and to derive slope- and aspect-related illumination conditions, both are using the same DEM, described in Chapter 4.3. Especially in mountainous regions selected for this study these conditions have a strong influence on the observed reflectance.

Table 3 summarizes the key conceptual and algorithmic characteristics of Sen2Cor, FORCE and Py6S with respect to atmospheric and topographic correction, cloud detection, aerosol and auxiliary data handling and is meant to support the interpretation of differences observed in the subsequent analysis. The illustrated information is based on the official documentation of Sen2Cor, FORCE and Py6S.

Table 3 - Conceptual comparison of atmospheric and topographic correction approaches

Aspect	Sen2Cor	FORCE	Py6S
Primary design goal	Operational product generation	All-in-one processing engine	Radiative transfer modelling
Typical application	Standardized L2A products	Large-scale and time-series products	Research and sensitivity analyses
Radiative transfer basis	Yes	Yes	Yes
Cloud and cloud shadow detection	Integrated and automated, mandatory	Optional, internal or external	Out of scope (clear sky) external only
Atmospheric correction strategy	RTE-based, LUT-assisted	Full RTE-based, external products	Full radiative transfer modeling
Aerosol handling	Image-based (fallback to external products)	Image-based or external products	User-defined or external
Topographic illumination correction	Yes	Yes	No
DEM usage	Elevation and terrain illumination	Elevation and terrain illumination	Elevation only
Adjacency effects correction	Empirical / approximate correction	Physics-based (via RTE)	No
BRDF correction	Optional (disabled by default)	Physical, Nadir BRDF-adjusted reflectance	BRDF modelling (optional)
Degree of user control	Limited	Moderate	High
Intended output	Analysis-ready surface reflectance	Time-series analysis ready data	Custom-corrected reflectance

The following sections describe Sen2Cor, FORCE and Py6S in detail. For each method, algorithmic implementation, required input data, parametrization and practical considerations are presented for an in-depth examination of the differences described in this chapter.

5.1. Sen2Cor

This chapter presents the algorithms implemented in the Sen2Cor processor as described in the official Level-2A Algorithm Theoretical Basis Document (ATBD) (European Space Agency, 2021).

Sen2Cor is an atmospheric correction processor, designed to process mono-temporal Copernicus Sentinel-2 images to generate L2A (BOA) products by correcting L1C (TOA) reflectance. This process consists of two components – the Scene Classification (SC) module, which generates a classification map with additional cloud and snow probability maps as necessary for the second component - the Atmospheric Correction (AC) module. AC is then using the provided maps to differentiate between clear land, water and cloudy pixels. The according algorithms are using the band ratios and spectral thresholding techniques discussed in Chapter 3.1.3. Therefore, they have been designed to be fast and efficient since AC relies on them.

Next, an optional cirrus correction can be performed utilizing the same spectral thresholding technique discussed earlier on the 1.38-µm water vapor absorption band (Sentinel-2 B10).

Atmospheric correction in Sen2Cor is based on radiative transfer modelling assuming a Lambertian surface and using pre-computed LUTs containing the relevant atmospheric information for surface reflectance retrieval. These LUTs are computed by the libRadTran library – a set of freely available functions for radiative transfer calculations (Mayer and Kylling, 2005). Explaining these algorithms in detail would be out of scope of this study, but in general libRadTran selects a different algorithm particularly optimized for dealing with either a signal strongly affected by atmospheric redirection or a signal reduced by gaseous absorption, depending on which physical effect is the dominant one for the particular region - scattering or absorption.

For aerosol (AOT) and water vapor retrieval Sen2Cor primarily relies on image-based approaches. When sufficient reference pixels are available, the DDV algorithm is used for AOT and the APDA – for water vapor retrieval. Both concepts have already been discussed in Chapter 4.2. If there are not enough DDV pixels in the scene, either default values or external CAMS data is used as a fallback option. These AOT and water vapor estimates are then subsequently used in combination with LUTs to retrieve the surface reflectance (BOA).

During the surface reflectance retrieval, Sen2Cor also accounts for adjacency effects. Since a detailed aerosol height distribution is not available for operational purposes, it is using an approximate and empirical approach for this correction by estimating the contribution from a 1 km neighborhood (or 2 km adjacency kernel window size) and subtracting it from the observed reflectance. This is an empirical, approximate approach which does not explicitly model multiple scattering effects but rather assumes that all neighboring pixels within the kernel contribute equally or according to a simple distance-based weight, which makes the correction faster and simpler, but also less accurate.

To avoid artifacts caused by a topographic correction of quasi-flat areas, Sen2Cor applies a set of conditions. Only if the elevation difference in the scene is > 50 m or at least 1 % of all pixels have a slope > 6 degrees a topographic correction using a DEM is performed, otherwise Sen2Cor ignores the DEM and switches to flat terrain processing. The correction is illumination-based and Lambertian, as described in Chapter 3.3., and can lead to reflectance overcorrections, especially in dark areas. To account for Non-Lambertian effects, an optional BRDF correction can be applied. However, by default S2 L2A products do not perform a BRDF correction.

All the algorithms described in this chapter are performed on a per-pixel scale. The flow chart of the processing chain is shown in Figure 8.

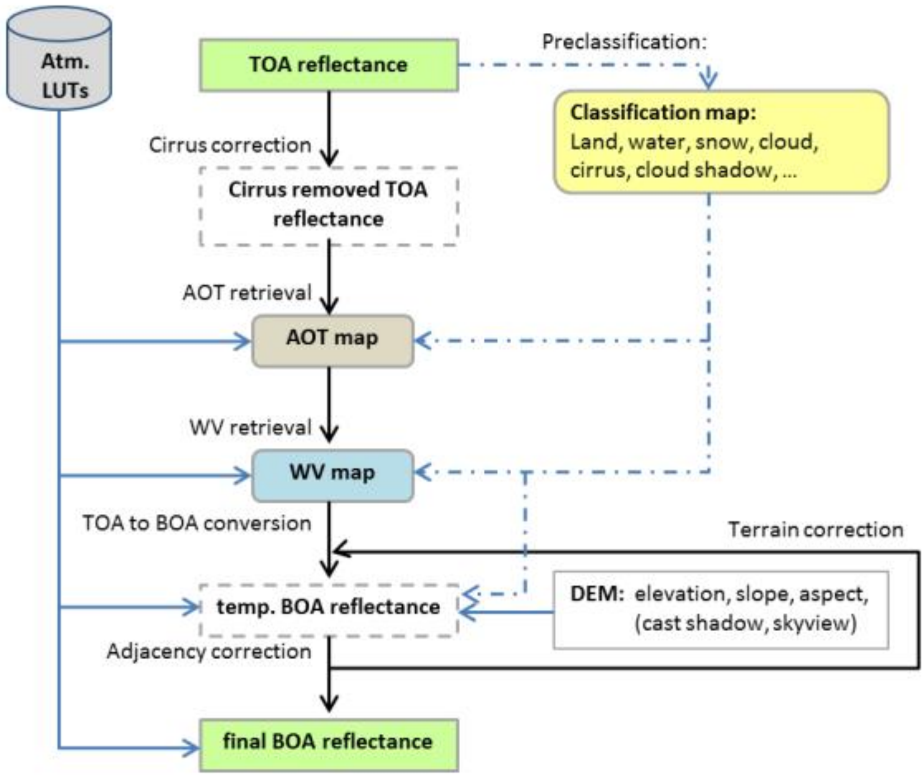

Figure 8 - Flow chart of Sen2Cor atmospheric correction processing chain (European Space Agency, 2021)

S2 L2A products can either be generated locally using a freely available Sen2Cor processor from ESA's Science Toolbox Exploration Platform STEP (European Space Agency, n.d.) or downloaded directly from the Copernicus Browser (European Space Agency, n.d.). In this study, the latter option was used to ensure consistent and operationally validated atmospheric correction. For the full list of the datasets used, please refer to Appendix A – Table A2.

The main strength of Sen2Cor-processed datasets - regardless of the retrieval method - is the strong integration with the Sentinel-2 product chain, automated scene classification and operational stability across different regions and seasons by the selection of appropriate algorithms depending on the given conditions. Its use of pre-computed LUTs makes it efficient and thus well suited for processing large datasets. The availability of standardized download-ready products eliminates the need for additional software and computational effort and ensures reproducibility.

Sen2Cor's limitations arise from its image-based aerosol and water vapor retrieval, simplified topographic and adjacency and missing BRDF corrections in the default product. This might result in a lower performance in complex terrain, snow-covered regions and regions with strong illumination variations, which make up most of the areas analyzed in this study. Furthermore, the degree of user control is either very limited or not given at all when it comes to download-ready data. Nevertheless, Sen2Cor represents a reliable method for surface reflectance generation and is well suited to the comparative analysis in this study.

5.2. FORCE

Unlike strictly operational processors like Sen2Cor, which are designed to follow a single purpose, end-to-end processing chain, FORCE is a modular processing framework for EO, where atmospheric correction is only one of many modules. Its primary purpose is to support large area, multi-temporal and multi-sensor time-series analysis by using data cube concept for generating ARD. According to FORCE documentation (Frantz, 2020c) ARD is understood as “readily usable for any application without further processing” in this context. The framework is designed to be flexible and configurable with a strong emphasis on physical consistency. All the information presented in this chapter is based on the software’s documentation (Frantz, 2020a) and the technical note (Frantz, 2019).

Cloud and cloud shadow detection in FORCE is performed using a rule-based approach named Fmask (Zhu and Woodcock, 2012). In summary, this algorithm combines spectral thresholding, band ratios and indices, cirrus and thermal band tests, morphological filtering and geometric cloud shadow projection. All of these methods except the thermal band tests and geometric cloud shadow projection have been already described earlier. The thermal band test refers to the early Landsat missions, which do not have a dedicated cirrus (water vapor absorption) band like Sentinel-2 does. Instead, they make use of the thermal infrared (TIR) bands and the fact that clouds are generally colder than the surface. By applying appropriate thresholds in TIR, cloud presence can be detected. A geometric cloud shadow projection, in simple terms, estimates where a cloud shadow falls on the ground depending on the position of the Sun, the satellite viewing angle and the height of the cloud. Additionally, although beyond of the scope of this study, a multi-temporal comparison of time-series data can also be used to catch clouds and cloud shadows that the per-scene Fmask might have missed. FORCE is also capable of using external cloud and cloud shadow products.

Atmospheric correction in FORCE is based on radiative transfer modeling, AOD is, by default, estimated from the image using the previously mentioned DDV algorithm with multiple scattering. Although FORCE’s parameter file includes the option to provide external AOD values, it also contains a recommendation to use the internal algorithm only. In this study, this recommendation was followed. Water vapor amount is directly estimated from the Sentinel-2 image.

Although adjacency effect is not explicitly mentioned in the technical note, it can be inferred from the surrounding description how FORCE is handling the correction. It states that the radiometric correction is embedded in radiative transfer framework and accounts for multiple scattering and that the background reflectance is approximated using “three kernels of increasing size” (Frantz, 2019). Since the mentioned background reflectance stands for the lateral contribution of neighboring surfaces within radiative transfer theory, this indicates physics-based modelling and correction rather than Sen2Cor’s empirical neighborhood smoothing. This approach is promising to be more accurate, especially for the heterogeneous scenes analyzed in this study.

Compared to Sen2Cor’s illumination-based, Lambertian-assumption-driven topographic correction, which mainly focuses on the geometric relationships between the Sun and the surface and neglects or simplifies diffuse illumination and surface anisotropy, FORCE applies a physics-enhanced correction additionally accounting for diffuse sky light, atmospheric scattering and non-Lambertian surface effects. This approach allows an estimation of an individual correction factor (C-factor) for each pixel before propagating it through the bands in a physically consistent way based on radiative transfer theory.

Nadir (straight-down) BRDF-adjusted reflectance can be computed using MODIS-derived parameters, which describe different scattering processes contributing to the observed reflectance. These parameters allow to remove directional effects caused by the Sun and sensor angles, therefore allowing a more consistent comparison between images taken at different times and seasons.

As in Sen2Cor, all the described algorithms in FORCE are performed on a per-pixel basis. FORCE Level 2 Processing System (L2PS) workflow including the described corrections is shown in Figure 9.

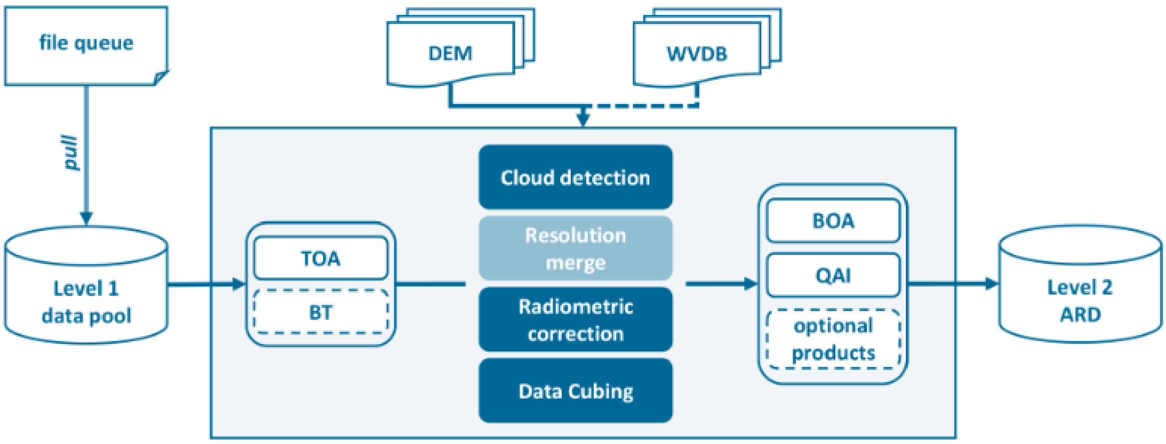

Figure 9 - FORCE Level 2 Processing System (L2PS) workflow. WVDB - water vapor database; BT - brightness temperature; QAI - quality assurance information (Frantz, 2019)

The blue box in the figure above represents the image. Brightness temperature (BT) – a measure of the thermal emission converted to a temperature-like unit - is only used when the input sensor has thermal infrared (TIR) bands, which is not the case for Sentinel-2 as described earlier in this chapter. Although a water vapor database (WVDB) can be used, it is not necessary and even not recommended by FORCE documentation for Sentinel-2 images. Instead, the values are being estimated from the image directly. A Cloud Storage Downloader (CSD) module enables the user to acquire Level 1 data directly from cloud services like Google Cloud Storage. When used, CSD requires additional configuration for service authentication, downloading and storage of data. The module was not used in this study since S2 L1C data has already been downloaded prior to processing to ensure that all processing methods operate on the same input data, ensuring comparable and consistent results.

FORCE is using a parameter file to parameterize L2PS. The file controls the processing environment, masking options, correction steps, spatial referencing and output products. The following section provides a description of the parameters relevant to this study. The complete file is provided in Appendix B.

The parameter file is organized in sections. The first section is dedicated to the input and output management defining the directories for Level 1 input and Level 2 output data, the parameter file itself, log files, temporary files which might be created during the correction process, provenance files and auxiliary data. Following the recommendation in the documentation (Frantz, 2020c), separate directories were created for each of the mentioned components.

In the next – the masking – section a vector file can be provided to clip the output product to a defined area of interest (AOI). By default, this option is disabled and was not used in this study.

Next is the DEM section. FORCE needs a DEM for cloud and cloud shadow detection as well as for atmospheric and topographic corrections. If no DEM is provided, the quality of cloud and cloud shadow detection and the atmospheric correction will be degraded, topographic correction simply cannot be performed. Depending on AOI and the DEM used, an additional mosaicking step might be required. However, due to a careful selection of a DEM discussed in Chapter 4.3. this step was not necessary for the purposes of this research.

Next section controls FORCE's data cubing parameters such as reprojection to a target coordinate system, spatial resolution, tile size etc. which are primarily designed to process multi-temporal or multi-sensor datasets. Since the primary objective of this work is to compare the outputs of different atmospheric correction methods rather than performing temporal stacking or harmonization, data cubing options were not applied to avoid introducing unnecessary processing steps and potential artifacts.

As for the radiometric correction, all available options – atmospheric, topographic, BRDF, adjacency and multiple scattering – corrections were enabled in the corresponding section to ensure the output product to be as physically accurate as possible.

Following the notes and recommendations provided in the parameter file, AOD and water vapor were set to be estimated internally. The same holds true for cloud detection options – all parameters were kept at their default settings.

FORCE offers several methods for resolution merging – improving the spatial resolution of 20 m bands to 10 m. Deviating from the suggested default performance-quality trade-off method, regression (Hill et al., 2003) was chosen in favor of its increased prediction quality, but at the expense of significant processing time.

The next three sections – parameters for co-registration of Sentinel-2 images, noise removal and no data handling and quality tier of Landsat data – were not used and therefore kept unchanged at their default values.

FORCE L2PS employs a nested parallelization approach combining multiprocessing and multithreading. The first parallelization level – multiprocessing – allows the system to process multiple images simultaneously while the second level – multithreading – enables different computational tasks for an individual image to be run concurrently. On the system used in this study (AMD Ryzen 5 1600 Six-Core Processor 3.20GHz, 16GB RAM, SSD for storage), multiprocessing was restricted to a single process by memory constraints, as each FORCE process requires a considerable amount of RAM, especially when processing Sentinel-2 data with all the enabled processing options described above. Increasing the number of parallel processes resulted in memory exhaustion and cancelled execution. Two parallel threads were used to improve computational efficiency without exceeding the available system resources, which is consistent with the recommendation in FORCE's documentation for systems with limited RAM and a small number of input images.

Finally, the last section of the parameter file controls the output options. The output format was set to a widely supported, compressed GeoTIFF to ensure compatibility with GIS and remote sensing tools. Overview thumbnails were generated for a quick visual inspection and quality control of the processed images. Auxiliary outputs not required for this study were disabled.

FORCE was developed and tested primarily on Ubuntu LTS systems but can also run on other Linux distributions. In case of a Windows operating system, it is strongly recommended to be executed within container environments like Docker. In this study, FORCE (v3.8.01) was run in a containerized environment using Podman Desktop (v1.20.2) instead of Docker, mainly for practical reasons – in was already installed and more convenient for the author to use and the choice does not affect the compatibility or reproducibility of the results. To ensure compatibility and reproducibility, uncorrected L1C data mentioned in Chapter 4.1 and listed in Appendix A – Table A1 was used as input data.

The primary strengths of FORCE are its physical robustness and flexible solution, not only for atmospheric and topographic corrections, but also for other large-area and time-series analyses. Integrated data cubing capabilities allow mass-generation of ARD.

The biggest downside of FORCE is its steep learning curve – especially for users not familiar with coding. The installation and execution within a containerized environment require proficiency with command line tools due to the fact that no graphical user interface (GUI) is provided. Aside from additional learning effort, this approach also introduces a higher risk of user-induced configuration errors. Another limitation arises from a limited user control – although users can enable or disable individual modules, the underlying algorithms are predefined and not directly adjustable. Lastly, computational complexity results in high resource requirements and significant processing times.

Overall, FORCE represents a comprehensive correction framework for physically based atmospheric and topographic corrections in this study.

5.3. Py6S

Building on the radiative transfer theory introduced in Chapter 3.2, the Second Simulation of the Satellite Signal in the Solar Spectrum (6S) represents its practical and widely used numerical implementation. In other words – 6S is a computer code designed to accurately simulate how solar radiation is affected by the atmosphere and Earth's surface along its path from the Sun to the surface to the satellite sensor. It models the coupled effects of atmospheric constituents, Sun-sensor geometry and surface properties based on predefined atmospheric profiles, aerosol models and surface reflectance representations, allowing an accurate retrieval of TOA radiance in the VIS and NIR spectrum (Vermote et al., 1997). In this way, 6S acts as a bridge between the theoretical RTE formulation and the practical application in remote sensing and represents a physically based framework for performing atmospheric corrections.

The original 6S model is controlled via input file requiring numerical parameters - even for categorical options - making reading and editing difficult and prone to user errors. Furthermore, the file requires a strictly defined format and is limited to one parameter set, making batch processing impossible without manual editing between simulations. An example of such an input file is shown in Figure 10. Finally, while being human-readable, the output files are not properly suited for automated data extraction. Py6S is a Python interface to 6S model, specifically designed to overcome the described limitations by acting as a wrapper rather than a re-implementation of the original, ensuring numerical consistency with native 6S results. It is intended to offer a convenient framework for radiative transfer research making 6S more accessible to a broader audience (Wilson, 2013).

```
0 (User defined)
40.0 100.0 45.0 50.0 7 23 (geometrical conditions)
8 option for Water Vapor and Ozone
3.0 3.5 Water Vapor and Ozone
4 User's Components
0.25 0.25 0.25 0.25
0
0.5 value
-0.2  (target level, negative value)
-3.3 (sensor level)
-1.5 -3.5 (water vapor and ozone)
0.25 (aot)
11 (chosen band)
1 (Non homogeneous surface)
2 1 0.5 (ro1 ro2 radius)
1 BRDF
-0.1 radiance (positive value)
```

Figure 10 - Sample 6S input file (Wilson, 2013)

Given the core purpose of Py6S, cloud and cloud shadow detection are outside its scope, Py6S does not analyze the image directly and therefore does not include any algorithms dedicated to it. Same is true for adjacency and topographic corrections. Adjacency effects require spatial modelling of surrounding pixels, topographic correction – functions to handle slope, shadowing and terrain-induced illumination effects. While including BRDF models, Py6S relies on accurate surface-specific parameters, which are often unavailable for Sentinel-2 images in the required quality or resolution. Therefore, in practice, Py6S usually assumes Lambertian surfaces. Py6S allows users to define surface altitude, which has an impact on atmospheric pressure, air density and gas absorption within the radiative transfer model. This enables correction for variations in atmospheric column thickness across different elevations.

Atmospheric correction with Py6S is performed through explicit radiative transfer modelling. The 6S model computes atmospheric transmittance, path radiance and scattering effects and reverts the RTE to retrieve surface reflectance when TOA radiance is given as input. In order to do so, Py6S relies on user-defined atmospheric profile, sensor geometry and surface assumptions. It does not estimate these properties from the image itself, as already mentioned earlier. The same applies to aerosol handling – the user must explicitly define the aerosol profile, AOT value and band-specific spectral response functions.

Py6S offers the highest level of transparency and user control among the evaluated methods. Its strengths include explicit radiative transfer modelling and flexible parametrization. Its flexibility makes Py6S well suited for experiment or testing scenarios and workflow integration. Considering its purpose, Py6S represents a significant improvement over the original 6S software, making it far more accessible, user-friendly and compatible with other workflows while preserving the underlying physical accuracy.

The limitations of Py6S include missing cloud and cloud detection, adjacency effect and topographic correction algorithms as well as its reliance on detailed input parameters. Built-in BRDF correction is often impractical due to required surface-specific parameters that are rarely available for Sentinel-2 data. Finally, for effective use Py6S demands both - proficiency in Python coding and a solid understanding of radiative transfer theory to correctly configure atmospheric and surface parameters, which makes it particularly prone to user errors.

Py6S does not perform topographic illumination correction, adjacency correction or BRDF modeling, which makes it especially sensitive to high SZA, snow and complex terrain. At high SZA, sunlight travels a longer path through the atmosphere which increases scattering and absorption by gases and aerosols. As a result, less direct sunlight reaches the surface, in other words - direct irradiance ($\boldsymbol{E_{dir}}$) decreases and the diffuse irradiance ($\boldsymbol{E_{dif}}$) often becomes the dominant component relative do $\boldsymbol{E_{dir}}$. Snow enhances the observed, reflected radiance, but it does not increase the downwelling irradiance components $\boldsymbol{E_{dir}}$ and $\boldsymbol{E_{dif}}$, in other words Py6S still assumes weak illumination, but the observed signal is actually bright. Furthermore, at high elevations and thus – thinner atmosphere, assumptions about aerosol content, gas concentrations and surface reflectance can cause large relative changes in $\boldsymbol{E_{dir}}$ and $\boldsymbol{E_{dif}}$. These effects can destabilize the surface reflectance calculation, and hence small, modeled irradiance values can lead to disproportionally large surface reflectance estimates, not constrained by illumination and adjacency correction or BRDF modeling.

Within this study Py6S represents a physics-based reference implementation of atmospheric correction, which is suited to be compared to the automated, operational processing of Sen2Cor and the integrated processing framework provided by FORCE.

The code implementation in this study builds upon the Py6S wrapper (Wilson, 2013) for 6S radiative transfer model (Vermote et al., 1997) and the codebase published in the original GitHub repository (Wilson, 2026). While the core radiative transfer calculations and atmospheric correction formulas remained unchanged, multiple modifications were implemented, primarily for operational usability and comparability with Sen2Cor and FORCE:

- **Sentinel-2 data loading and preprocessing**

  A complete S2 L1C data ingestion pipeline was implemented for .SAFE file handling and automated metadata parsing of radiometrically critical parameters (solar irradiance, geometry, satellite platform, quantification value, radiometric offset). Band selection for processing allows correction execution for specific bands only to reduce the file size and processing time. Spectral response functions are being selected from built-in Py6S constants depending on the satellite platform used.

- **Radiometric offset correction for processing baseline 04.00+**

  Starting with processing baseline 04.00 introduced in January 2022, ESA added a constant band-dependent radiometric offset to Sentinel-2A and Sentinel-2B data to avoid clipping of negative values (European Space Agency, 2025c). Without this adjustment, TOA reflectance values are systematically biased, leading to incorrect atmospheric correction results.

- **Spatially explicit per-pixel elevation correction**

Instead of assuming sea-level conditions, elevation data from a DEM was integrated to apply elevation-dependent atmospheric correction on a per-pixel basis. To ensure perfect pixel-to-pixel alignment between elevation and reflectance data, DEM was clipped to scene bounds, reprojected and resampled to match Sentinel-2 grid. An elevation bin size of 100 m was chosen as variations in atmospheric properties over smaller intervals would increase the processing times without resulting in significant improvements in simulated surface reflectance.

- **CAMS data integration and unit conversion**

  Automated retrieval and unit conversion of AOT, water vapor and ozone from CAMS data were implemented to improve correction accuracy by using actual atmospheric data instead of standardized atmospheric models. Therefore, atmospheric profile parameter was set to be defined automatically depending on these values. Water vapor units were converted from kg/m² to cm and ozone units – from kg/m² to cm-atm (using conversion factor 46.698) as expected by 6S.

- **Output scaling**

  To match Sen2Cor and FORCE output format and reduce the file size, surface reflectance values were scaled from [0,1] float32-values to [0,10000] integer range.

- **Preservation of high reflectance values**

  To avoid artificial bias by clipping surface reflectance >1.0 (respectively, 10000) and remain aligned with FORCE and Sen2Cor, higher values were preserved. Physical surfaces can exceed apparent reflectance of 1.0 due to BRDF effects or snow presence.

- **Negative reflectance floor and Nodata pixel preservation**

  Physically non-meaningful, negative reflectance values arising from noise and atmospheric correction uncertainties were floored at 0.0001. Nodata pixels were preserved to identify data gaps.

- **Automated quality control and validation checks**

  Extensive quality assurance mechanisms (high SZA, missing atmospheric data, excessive AOT values, over-correction artifacts) and comprehensive logging (intermediate values, output statistics, diagnostic warnings) were implemented to allow detection of potential issues.

- **Multiband GeoTIFF output generation**

  To match FORCE output format a functionality for multiband GeoTIFF generation was implemented.

Additionally, certain parameters were defined manually. Aerosol profile was set to "continental", which is the predefined value for inland within Py6S. View zenith angle was set to nadir (0°) to reflect the near-nadir acquisition geometry of Sentinel-2 MSI. For nadir viewing geometry, view azimuth angle becomes meaningless and was set to 0, accordingly. Using metadata values would sensitize correction to angular uncertainties without meaningfully improving the correction accuracy.

6. Categorization with SIAM

SIAM - the Satellite Image Automatic Mapper is a prior knowledge-based expert system developed for automatic spectral categorization of satellite imagery (Baraldi, 2011). Unlike machine learning classifiers, it does not rely on training data but is rather applying predefined rules from physical and expert knowledge of spectral reflectance behavior. Operating as a deterministic decision tree, SIAM derives a set of spectral categories from radiometrically calibrated reflectance values. These categories represent an intermediate level of interpretation between raw reflectance measurements and high-level land cover classification.

SIAMs algorithm operates point-wise, analyzing each pixel independently without incorporating spatial context. Each reflectance vector is assigned to one of the 33 distinct spectral categories with no overlaps or gaps. These mutually exclusive and collectively exhaustive categories do not represent land cover classes. In consequence, same spectral signatures can correspond to different land cover types depending on spatial, temporal or contextual factors. They are designed to resemble the natural human color perception and to be application-independent and scalable, with implementations available for different multispectral imaging sensors like Landsat or Sentinel-2 (Baraldi, 2011; Major et al., 2025).

For Sentinel-2 data analysis in this study, SIAM is utilizing six spectral bands: Blue (B02), Green (B03), Red (B04), NIR (B08) and two SWIR (B11, B12) bands (see Table 2). SIAMs algorithm partitions the six-dimensional space into 33 multi-dimensional polygons, each associated with a specific spectral category (Interdisciplinary Centre of Competence for Geoinformatics, Z-GIS, University of Salzburg and Spatial Services GmbH, n.d.). A full list of SIAMs categories with their descriptions, abbreviations and color symbolization is shown in Appendix AB. Category abbreviations indicate vegetation type (SV = Strong vegetation, AV = Average vegetation, WV = Weak vegetation), NIR response (HNIR = high NIR, LNIR = low NIR) and other spectral characteristics. Non-vegetated categories include various bare soil types (e.g., DBB = Dark bare soil, BBB = Bright bare soil), snow and ice (SN_WAICE = Snow or water ice), water bodies, and atmospheric phenomena (e.g., SH = Shadow, TNCLV = Thin cloud over vegetation).

One fundamental consideration for this study is the fact that SIAM originally was developed for TOA reflectance data, where atmospheric phenomena like clouds and shadows are to be preserved rather than treated as artifacts and removed (Interdisciplinary Centre of Competence for Geoinformatics, Z-GIS, University of Salzburg and Spatial Services GmbH, n.d.). This means, that when SIAM is applied to BOA surface reflectance data – the primary focus of this study – fundamental tensions arise. Atmospheric correction algorithms including Sen2Cor, FORCE and Py6S aim to remove atmospheric effects and retrieve true surface reflectance, which results in considerable modifications of spectral characteristics of surface categories like vegetation, soil or snow. These modifications can push a pixel outside of SIAMs fixed spectral category boundaries, leading to more or less extreme classification changes.

To the best of author's knowledge, the beforementioned TOA-BOA tension has not been quantified in the literature yet. While SIAM has been validated at continental scale (Baraldi et al., 2018) and utilized in different operational contexts (Arvor et al., 2021; Major et al., 2025), but its performance on atmospherically corrected imagery has not been evaluated. This study addresses this knowledge gap by comparing SIAM categorization of Sentinel-2 imagery across correction methods Sen2Cor, FORCE and Py6S relative to TOA baseline and to each other. By analyzing nature and magnitude of categorization changes and the impact of seasonal and terrain-induced effects, this research provides valuable insight into the consequences of atmospheric correction on spectral categorization applications. SIAM provides the analytical framework for this evaluation.

7. Results

This chapter is divided into four sections: first part – Chapter 7.1 – gives a short overview of the category distribution across all four methods, which allows for a quick visualization of distribution differences and a better understanding of how atmospheric correction generally changes SIAM's spectral interpretation.

The second sub-chapter is mostly focused on inter-method consistency between BOA methods. This section is designed to demonstrate whether Sen2Cor, FORCE and Py6S produce consistent SIAM results or strongly disagree and therefore produce uncertainties, and if so – to what extent. For this purpose, Cohen's Kappa and overall accuracy have been calculated. Cohen's Kappa ($\boldsymbol{\kappa}$) is a chance-corrected measure of agreement between two categorical classifications, which provides a more reliable indicator of classification consistency than a simple percentage agreement (Cohen, 1960).

To evaluate where the changes actually occurred, agreement on per-category level has been calculated in the next step. This helps to identify strong categories, where spectral signatures are reliably categorized regardless of correction method and weak categories with inconsistent results revealing which parts of SIAM's decision tree are sensitive to atmospheric corrections. Finally, each BOA method has been compared to L1C baseline to display the direction and the magnitude of category transitions to identify potential unidirectional systematic biases.

While the previous section is focused on the inter-method consistency, Chapter 7.3 aims at answering the question how much atmospheric corrections change SIAM's behavior. For this purpose, each BOA method has been compared to L1C, which represents the baseline in the context of this study due to the fact that SIAM was validated on TOA reflectance data. To classify the severity of a change, every pixel has been assigned to one the four categories – No Change (pixel stayed in the same category), Minor or intra-type change (category shift withing the same land cover type, e.g. "Average vegetation" -> "Strong vegetation"), Major or inter-type change (pixels moved to unrelated land cover type, e.g. "VEGETATION" -> "BARE SOIL") and extreme change (pixels shift to cloud or shadow-related atmospheric phenomena categories or UNKNOWN).

For many applications knowing the land cover type is sufficient, even if the exact category within the subtype differs. To evaluate SIAM's broad physical decision tree branches stability, all 33 categories have been grouped into 12 classes. For each class, pairwise agreement between the L1C baseline and the BOA method has been calculated to demonstrate the cover type consistency across all methods.

Finally, Chapter 7.4 examines the geographic distribution of classification inconsistencies through a visual inspection and spot checks. This chapter aims to verify whether previously identified disagreement trends are spatially logical and to isolate recurring landscape features associated with the highest classification instability.

7.1. SIAM category distribution analysis

Analyzing the category distribution across BOA methods, strong vegetation categories SVHNIR and SVLNIR dominate Eastern planes and the Pre-Alps in spring and summer with 40-65% pixel coverage, while average vegetation categories constitute only 15-30% (Appendix C-Appendix F). Snow and ice (SN_WAICE) show strong seasonal and elevation gradients, ranging from 25-45% coverage in high-elevation winter and spring to 5-15% in summer. Compared to the S2 L1C baseline, consistent differences between similar categories can be observed: strong vegetation increases by 5-12% while average vegetation decreases by 8-15% across all methods. Bare soil categories maintain a relatively stable presence at 10-20% coverage with 5-8% inter-method variability. Atmospheric phenomena categories show minimal retention (< 2%) after correction. Method-specific patterns can also be observed for Py6S – with 6-44% depending on the season, it generates a significantly higher number of UNKNOWN pixels compared to other methods.

7.2. Inter-method categorization consistency

- **Alpine valleys**

The Alpine valleys region shows the lowest, but still strong seasonal variation in the impact on SIAM categorization consistency. Spring exhibits the best results with Cohen’s Kappa reaching 0.71 and 76% accuracy between Sen2Cor and FORCE (Appendix G) and overall good agreement between the correction methods, corresponding to the optimal SZA of 27° (Table 1), which minimizes atmospheric path length. In contrast, winter indicates severe problems with Kappa and accuracy dropping to 0.38-0.47 and 48-56% respectively, directly reflecting the extreme 67° SZA that increases the path length by 2.3 times compared to spring. These low agreement values, where the methods disagree on more than half of all pixels, make SIAM categorization highly unreliable. Autumn and summer show moderate performance with Kappa between 0.45 and 0.66, with autumn’s 56° SZA creating intermediate atmospheric path length which results in intermediate categorization stability. These patterns show a clear correlation to solar geometry with the atmospheric path length, which increases proportionally to 1/cos(zenith angle), being one of the dominant factors controlling the categorization stability.

Examining the per-category reliability reveals significant disagreements between BOA methods at the individual category level. SVHNIR achieves only 56% mean agreement, SVLNIR drops to 38%, AVHNIR to 26%, AVLNIR to just 16%. Most vegetation categories show below 40% inter-method agreement, which is a strong indication, that while pixels remain categorized as “vegetation”, the BOA methods frequently disagree on which specific category applies. The most reliable category in this region is SN_WAICE with 81% agreement (Appendix K).

One notable finding is the consistent volatility of the AVLNIR category, which loses 14-20% of its pixels across all seasons and methods (Appendix L), typically transitioning to SVHNIR (Appendix P). This systematic bias suggests that atmospheric correction increases the apparent NIR reflectance of vegetation affecting SIAM's vegetation categorization capabilities.

- **High Alps**

The High Alps region also shows a strong seasonal variation in SIAM categorization stability across all four regions with strong similarities to the Alpine valleys region. Spring produces the best agreement with Cohen's Kappa reaching 0.61-0.70 and an overall accuracy around 67-75%. Winter introduces a severe failure with Kappa dropping to 0.35-0.47 and an accuracy between 45% and 55% (Appendix H). Following the same pattern as the Alpine valleys region, a clear seasonal gradient becomes apparent: spring shows the best results, followed by summer and autumn, while winter performs by far the worst, which again directly correlates with the given SZA of 67° (Table 1).

Another strong similarity to Alpine valleys is demonstrated in per-category reliability - atmospheric correction preserves SIAM's vegetation and snow distinctions reasonably well in spring and summer but introduces significant uncertainty in fine spectral category assignments regardless of season. Among all categories, SN_WAICE again achieves the highest inter-method reliability at 84%, while vegetation categories remain below 65% agreement (SVHNIR - 63%, others - <35%, see Appendix K).

Systematic bias patterns appear consistently across all seasons: abundant vegetation categories (AVLNIR, AVHNIR) show net losses of 7-12% of pixels (Appendix M), predominantly transitioning to sparse vegetation (SVLNIR, SVHNIR) (Appendix Q). Shadow categories consistently lose pixels to vegetation and snow categories (around 8-15%). Thin cloud categories lose most of their pixels to clear-sky vegetation or snow categories, indicating that atmospheric correction removes the spectral signatures of thin clouds.

- **Pre-Alps**

This region, being a transition between the Alps in the south and the flat regions in the north, is characterized by mid to low elevation levels and intensive agriculture and shows extreme – largest across all regions – seasonal variations in SIAM categorization reliability. Cohen's Kappa values span an extensive range between 0.25 to 0.76 across the four seasons (Appendix I), indicating that seasonal effects dominate over differences between correction methods. Spring produces excellent results with Kappa reaching 0.68-0.76 and overall accuracy of 80-85%, making it the best season across all four study regions. In complete contrast, winter shows severe failure with Kappa dropping to 0.25 between FORCE and Py6S revealing nearly independent categorization results between these methods. This extreme seasonal range corresponds to SZAs with a more than doubled path length in winter compared to spring, analogically to other regions. Additionally, moderate elevation seems to amplify the atmospheric path effects resulting in particularly difficult conditions for atmospheric corrections.

With 85% mean agreement between methods SVHNIR achieves the highest vegetation reproducibility across all regions (Appendix K). SVLNIR reaches 41%, AVHNIR - 43%, AVLNIR drops to just 19%, and SN_WAICE - 43%. Water and shadow categories prove to be highly unreliable across all seasons, showing 0-71% retention depending on the season and correction method.

The systematic bias where pixels (here - 8-19%) transition from abundant (AVHNIR, AVLNIR) to sparse (SVHNIR, SVLNIR) vegetation categories can be observed in this region again and persists across all atmospheric correction methods (Appendix R). Additionally, bare soil categories, while maintaining good to excellent retention rates depending on season and method, show persistent confusion between each other.

- **Eastern planes**

The inter-method agreement in this region shows almost as extreme variations as in the Pre-Alps, ranging from good agreement in spring and summer (with Cohen's Kappa between 0.64 and 0.77) to very poor in winter (with Kappa = 0.30-0.57) (Appendix J). Winter's extremely low Kappa values, particularly between Sen2Cor and Py6S (with Kappa = 0.30) again indicate near-random agreement showing the same strong correlation with SZA as the other regions. Similarly to what has been observed in the Pre-Alps, low elevations in combination with high SZA seem to amplify the atmospheric path effects due to a higher atmospheric column compared to more elevated regions.

SVHNIR shows with 84% mean agreement the highest reliability of all vegetation categories, SVLNIR reaches 35%, AVHNIR - 41%, AVLNIR - 28%, while SN_WAICE drops to the lowest snow reproducibility across all regions with just 33% (Appendix K).

Across all seasons and methods, 11-19% of AVHNIR pixels undergo the same transition to SVHNIR that has been observed in other regions (Appendix S). This consistent pattern across all regions indicates an enhancement of the vegetation spectral signal

7.3. Change severity analysis (BOA vs. L1C)

- **Alpine valleys**

In regard to change severity, Sen2Cor and FORCE generally show a good agreement with each other across all seasons, although FORCE tends to create more intra-type transitions within cover types, rather than between them (Appendix T). This observation correlates with the finding made in Chapter 7.2, that most vegetation pixels shift category, but stay categorized as "vegetation". Py6S shows unpredictable behavior in autumn, where it generates a 34.6% increase in UNKNOWN category pixels (Appendix C) contributing to 40.7% extreme changes (Appendix T). Overall, with the most changes being either minor or extreme, it can be stated that the categorization for a given pixel either works well or fails completely.

Comparing the BOA methods categorization to the TOA baseline reveals at the cover-type level what has been observed earlier at the category-level – VEGETATION shows a high stability across seasons and methods with 77-99% retention (Appendix X), meaning that most pixels assigned to vegetation in L1C remain in this class after BOA correction. SNOWE_ICE shows an even higher retention at 92-98%, confirming that broad land cover types remain relatively stable within SIAM despite atmospheric correction. However, other classes show major problems across all seasons. Shadow-related categories retain only 4-31% of their pixels, with most transitioning incorrectly to vegetation or water classes (Appendix P). Thin cloud and snow-shadow classes show a slightly better, but still poor stability. These lower retention rates indicate that atmospheric correction removes or alters the spectral signatures used by SIAM, introducing significant uncertainty in fine spectral category assignments.

- **High Alps**

Concerning the change severity, Sen2Cor and FORCE again perform similarly overall, mostly showing balanced transitions between categories. However, FORCE exhibits heightened sensitivity in summer, where only 52% of pixels remain unchanged compared to 62-64% for Sen2Cor and Py6S. This indicates that FORCE is applying stronger correction during this season, causing more category shifts within the VEGETATION class (Appendix Q). Py6S exhibits a similar variable behavior as in the Alpine valleys region – in summer it achieves the highest observed pairwise agreement with Sen2Cor (Kappa = 0.66), but in autumn in produces the highest number of extreme category changes – 22% (Appendix U), making Py6S less reliable than Sen2Cor and FORCE.

At the cover-type level, VEGETATION class shows good consistency with agreement values between 91-99% in spring and summer, 80-96% in autumn and 56-80% in winter. SNOW_ICE maintains an excellent agreement at 91-98% with a slight degradation in winter, while shadow-related categories consistently get reclassified across all seasons and methods (Appendix Y).

- **Pre-Alps**

Examination of the change severity reveals clear performance differences. Overall, Sen2Cor performs best minimizing extreme categorization changes to 4.3% in summer and 10.2% in spring (Appendix V). Winter is an exception, where Sen2Cor shows 39.4% extreme changes, confirming that winter conditions overwhelm all correction methods. Sen2Cor is closely followed by FORCE, exhibiting higher rates of moderate, but fewer rates of extreme categorization changes. Py6S shows severe problems across multiple seasons, generating 7.7-44% UNKNOWN category pixels (Appendix E). This categorization represents complete radiometric failure where Py6S correction pushes the spectral values to extreme or impossible ranges, which SIAM cannot categorize.

In regard to cover type consistency, VEGETATION shows excellent 98-99% agreement for Sen2Cor and FORCE in spring, summer and autumn and a slightly lower agreement between 84% and 95% in winter. Py6S shows with 98% agreement similar values in spring, 90% in summer, 70% in autumn and only 39% in winter (Appendix Z). Bare soil class shows varying agreement across season-method combinations, but with a persistent confusion between categories. Once again, cloud and shadow-related categories show the lowest retention rate across all classes.

- **Eastern planes**

Comparing the performance shows that Sen2Cor maintains the highest consistency across seasons with 53-73% remaining in their original SIAM categories, except in winter (Appendix W). FORCE shows comparable overall accuracy but tends to create more intra-type changes. Py6S shows problematic behavior in all seasons, generating 6-19% UNKNOWN pixels (Appendix J) pushing spectral values outside the range SIAM can assign. Winter amplifies the problems dramatically across all methods, dropping the unchanged pixels to 20% for Sen2Cor, 22% for FORCE and 21% for Py6S and maximizing the extreme changes to 35%, 32% and 45% respectively.

VEGETATION cover-type retention shows 92-99% in spring and summer under Sen2Cor and FORCE, degrading to 67-99% in autumn and 55-93% in winter. Bare soil and built-up areas maintain 55-88% retention depending on season and spectral brightness class, with systematic confusion between subtypes. Shadow and cloud-related categories perform poorly across all seasons (Appendix AA). Water and shadow classes retain 0-56% of their pixels, with zero retention in some season-method combinations. Shadow classes rarely exceed 30% retention, and thin cloud classes collapse almost completely with less than 13% retention. Shadow pixels most commonly get reclassified as vegetation or water after atmospheric correction, while thin cloud pixels transition to other clear-sky land cover classes (Appendix S). These consistent failures across all seasons confirm that these categories cannot be reliably used with BOA-corrected data in this region.

7.4. Spatial patterns of disagreement

Spatial disagreement between SIAM outputs follows the same pattern described in the previous chapters – the disagreement in concentrated in areas associated with shadowed surfaces and water bodies such as lakes, shaded slopes, shadowed snowfields and deep valley bottoms. Strongest effects can be observed in winter (Figure 11).

Water surfaces represent a persistent source of instability. In the Pre-Alps region during winter, extreme heterogeneity is demonstrated with a wild mix of agreement and disagreement within individual lakes as shown in Figure 12 (left).

Even during spring, when overall agreement in highest, SIAM's outputs frequently differ from the baseline and each other (Figure 12 - right). An exception is observed for Sen2Cor and FORCE, which show a comparatively high agreement over water bodies under favorable conditions.

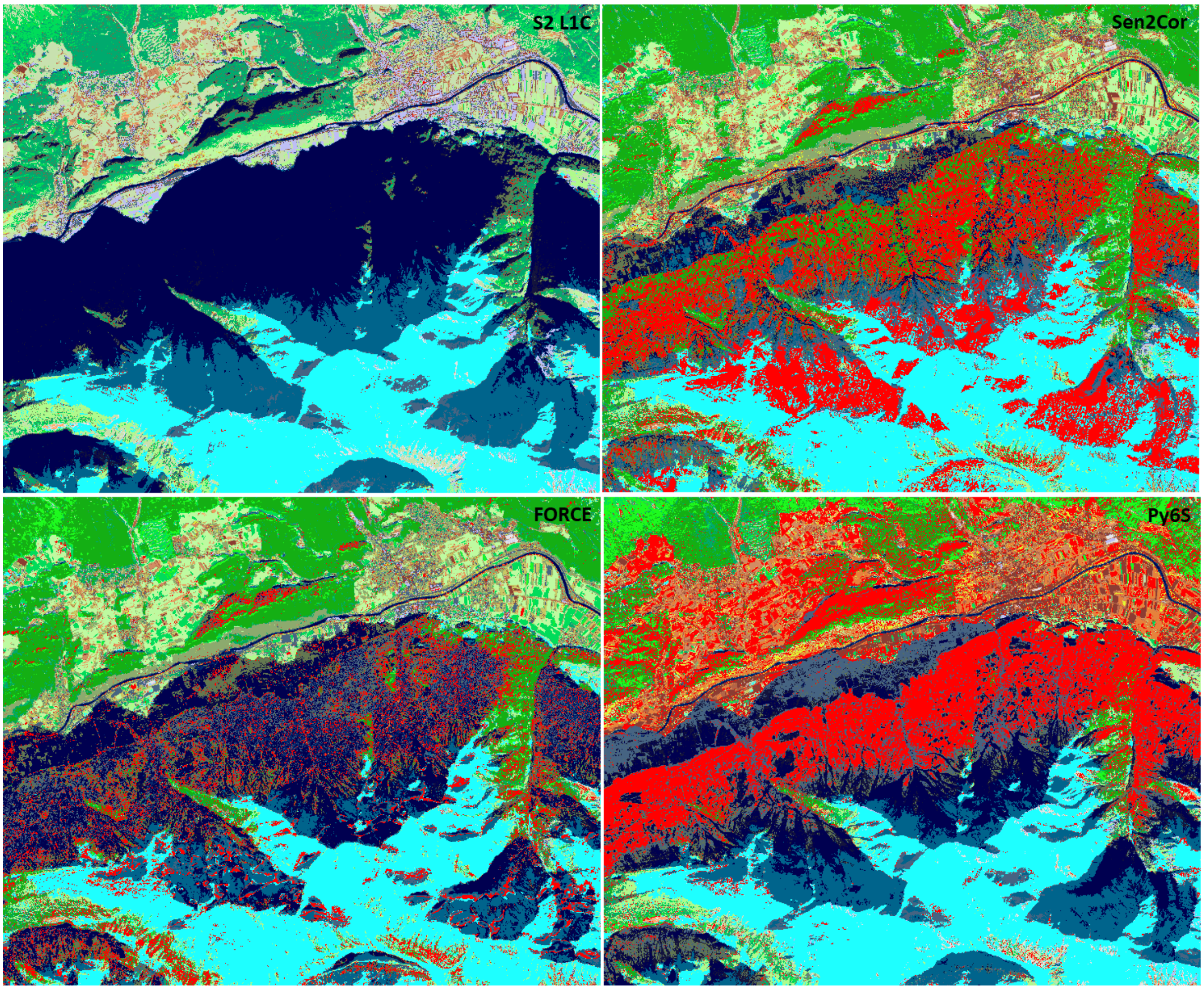

Figure 11 - Classification differences in winter (red - UNKNOWN category)

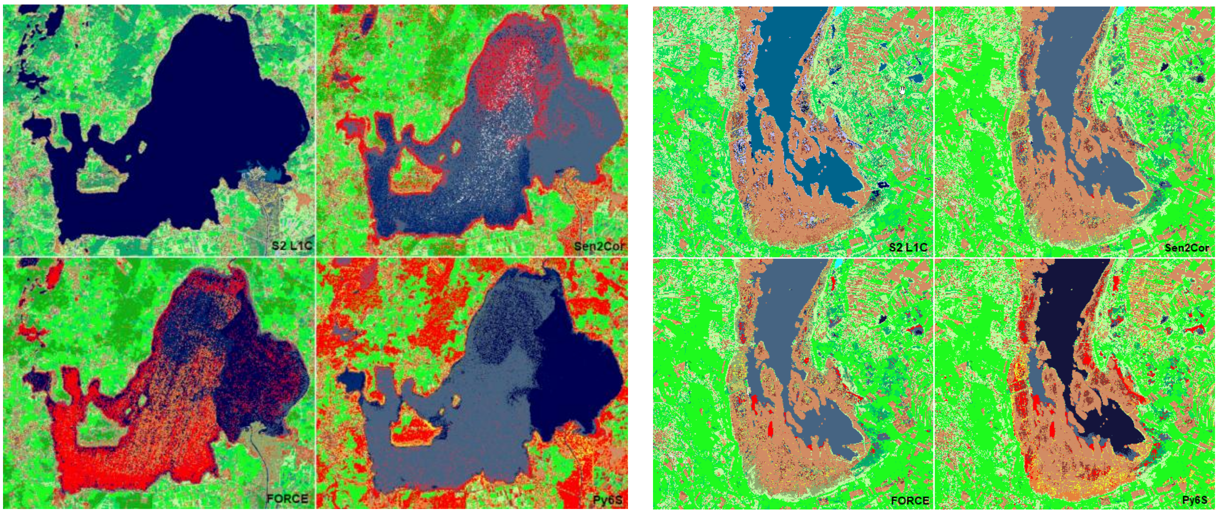

Figure 12 - Classification differences over water (left - winter, right - spring)

8. Discussion

In this study, the Satellite Automatic Image Mapper (SIAM) was used as a diagnostic rule-based spectral categorization framework to evaluate the effects of different preprocessing operations on spectral representation. It served as a spectral reference system to detect and quantify changes induced by atmospheric and topographic correction methods. The analysis was conducted in two phases: first, atmospheric correction methods Sen2Cor, FORCE and Py6S were compared to each other to evaluate their internal consistency and relative stability across four distinct regions and seasons. This step allowed for identification of systematic differences between the correction approaches at a spectral categorization level. In the second phase, the corrected data was compared to the uncorrected baseline to evaluate severity and the direction of changes introduced by corrections. Additionally, the evaluation was performed on two hierarchical levels of the SIAM output: at the category-level, individual spectral categories (e.g. strong vegetation, weak vegetation, bright bare soil, dark bare soil, deep water) were analyzed to capture fine-scale spectral transitions and potential systematic biases. At the more aggregated cover-type level, semantic classes (VEGETATION, SOIL, WATER) were examined to assess structural consistency and class-level stability. This approach allowed for a classification of changes and their severity (from minor intra-class shifts to extreme inter-class transitions). Overall, the objective was not only to quantify changes, but to interpret whether atmospheric corrections modify spectral signals in a manner that enhances physical plausibility or whether they introduce instability and over-correction artifacts.

SIAM's spectral classification was originally developed in the context of TOA reflectance data (Baraldi et al., 2018) in which atmospheric effects such as clouds and shadows are preserved and interpreted as meaningful spectral features rather than treated as noise. The results of this study indicate a systematic degradation of categorization performance when SIAM is applied to BOA corrected data. Compared to TOA, overall accuracy and agreement metrics decreased consistently across regions and seasons. In particular, significant reductions were observed during winter conditions and categories related to the mentioned atmospheric phenomena like clouds or shadows, which exhibit strongly reduced stability. The main implication here is that SIAM should not be applied as a complete 33-category system to BOA corrected data.

A cross-regional and cross-seasonal comparison reveals consistent differences in performance of the evaluated methods. Sen2Cor exhibits the highest overall stability, characterized by limited extreme category transitions and strong retention of the original spectral categorization under most conditions. FORCE shows almost comparable performance but demonstrates increased sensitivity in intra-class and boundary regions, leading to slightly more transitions across major land-cover types. In contrast, Py6S demonstrates pronounced instability in several cases by systematically shifting pixels towards unknown or ambiguous categories, indicating limited robustness under certain environmental conditions. These findings align with validation literature, where Sen2Cor and FORCE are reported to have a consistent performance (Kganyago et al., 2020; Sola et al., 2018) und low uncertainty levels in surface reflectance retrieval (Doxani et al., 2023).

Py6S's suboptimal performance diverges from Sen2Cor's and FORCE's, likely due to the fact that Py6S was primarily designed as flexible radiative transfer simulation and research tool rather than a comprehensive, operational atmospheric correction processor optimized for classification stability and therefore should not be used in the context of SIAM. Sen2Cor and FORCE seem to be acceptable for SIAM applications with awareness of FORCE's boundary softening.

A consistent seasonal pattern can be observed across all four study regions, indicating a strong influence of image acquisition timing on SIAM's categorization stability. Spring shows the highest overall stability with limited category transitions and a strong vegetation retention, closely followed by summer. Autumn scenes demonstrate moderate performance decline and increased confusion involving shadow-related categories. Winter exhibits the lowest stability, characterized by significant category transitions and significant degradation of vegetation-related classes.

These seasonal differences seem to be closely related to variations in solar geometry. Increasing SZA from spring and summer to autumn and winter results in longer atmospheric path lengths, which amplify atmospheric effects. This pattern can be observed across all regions, suggesting that solar geometry rather than seasonal or regional atmospheric variability is the dominant factor controlling the classification stability. Particularly shadow-related ambiguities increased strongly under high SZA, further reducing classification reliability.

As for the regions, Alpine valleys show the smallest seasonal variation in the BOA-to-BOA accuracy and agreement values, followed by High Alps, Eastern planes and the Pre-Alps. In the Alps and the Alpine valleys snow and ice categories are the most stable throughout the year, probably due to their distinct spectral signature and reduced atmospheric interference at high altitudes. In contrast, in the lower regions Pre-Alps and Eastern planes, strong vegetation demonstrates by far the highest unanimous agreement between the baseline and the correction methods and the lowest snow reproducibility. This can be explained by dense and homogenous canopy structures and reduced topographic shading effects in these mostly flat, vegetation-dominated regions. Across all regions and all seasons except winter, systematic near infrared (NIR) brightening can be observed, average vegetation pixels are systematically shifted to strong vegetation categories, most probably due to removal of scattering effects and compensation for adjacency and bidirectional reflectance (BRDF) effects during correction. In winter, dormant vegetation experiences substantial instability leading to widespread category transitions, especially in low-elevation regions. Overall, these observations indicate that uniform atmospheric correction and classification workflows are generally insufficient to account for region-specific environmental and spectral characteristics.

Category-level stability assessment reveals a relatively high agreement for certain strong vegetation and snow-related categories, while most weaker vegetation categories exhibit only moderate to low reproducibility. This is a strong indication that although correction methods tend to agree on the presence of vegetation, they frequently disagree on the assignment to particular vegetation categories. Many other spectral categories show a similar inter-method agreement, demonstrating sensitivity to correction parametrization and strategies.

At the cover-type level vegetation and snow-ice cover types generally exhibit highest retention rates, at least under favorable seasonal conditions. These classes are particularly robust, with the exception of winter, when dormant vegetation and low illumination increase spectral ambiguity. Bare soil and built-up cover display moderate retention with persistent confusion across categories. In contrast, categories related to atmospheric phenomena exhibit significant instability. For instance, thin cloud categories tend to collapse into clear-sky surface classes, while shadow-related categories often transition to underlying snow or vegetation classes. These classes are strongly linked to TOA spectral characteristics and therefore demonstrate a limited validity for SIAM after atmospheric correction.

Taken together, these results indicate that in practice most pixels are likely to remain classified within the same broad land cover type after correction, but their spectral category may vary considerably between correction methods. This leads to the implication that atmospheric phenomena categories should be excluded from operational SIAM deployment entirely and the users must be aware of systematic method-dependent uncertainty at the category-level.

The interpretation of the results of this study requires consideration of several limitations: first, the findings are specific to SIAM and may not be meaningful to other classification or categorization approaches for surface reflectance data. Second, the analysis is based on four Austrian regions, which do not fully represent atmospheric and land cover conditions in other regions or climatic zones. Third, choosing different parameters for the correction methods or adding missing functionality (e.g. BRDF or topographic corrections for Py6S) might significantly improve SIAM results. Fourth, TOA-based categorization itself, used as baseline for this study, may introduce uncertainty or errors which could propagate through the analysis. Furthermore, driven by practical reasons, image acquisition was limited to single-image seasonal snapshots, which do not reflect year-to-year variability. The results also depend on the specific software versions and future updates may lead to different performance characteristics. The partition into 33 categories and 12 classes may have hidden fine-scale correction effects, while the spatial resolution of Sentinel-2 could have led to correction instabilities near spectral boundaries. Finaly, the results do not reflect absolute accuracy due to the lack of definite ground-truth reference but rather focus on inter-method consistency.

Based on the analysis results and the described limitations, some practical constraints for the application of SIAM in combination with atmospheric correction can be defined. First, usage should be limited to low SZA acquisitions only, which for in the context of this study were primarily spring and summer. Autumn must be treated with caution due to its moderate instability, while winter should generally be avoided. Regarding atmospheric correction methods, Sen2Cor demonstrated the most reliable performance and is therefore recommended as the primary processing approach. FORCE also may be used under certain conditions, but requires careful validation, while Py6S should not be used for routine classification workflows.

At the category-level, only strong vegetation and snow-ice categories can be recommended for high-accuracy applications. Other categories can be used after comprehensive validation, whereas atmospheric phenomena categories should be avoided. Overall, validation procedures should be linked to specific regions and seasons, as they are shown to not be directly transferable across different environmental conditions. Therefore, unrestricted use of SIAM category hierarchy in combination with atmospheric correction is generally not recommended.

9. Conclusions and outlook

The findings of this study do not oppose previous atmospheric correction validation studies but rather extend their scope to a different class of classification systems. Earlier work has mostly focused on radiometric accuracy and machine learning approaches, generally revealing only minor differences between correction methods. For instance, Sola et al. (2018b) reported a similar radiometric performance between different atmospheric correction methods across land cover types when validated against field measurements. However, their analysis primarily focused on Mediterranean environment. Similarly, Rumora et al. (2020) concluded a relatively minor impact of atmospheric corrections on classification performance across different machine learning algorithms. In contrast, the present study demonstrates that even small radiometric differences can cause significant variations in rule-based categorization systems like SIAM, especially under suboptimal conditions. And although atmospheric correction is often recommended to improve classification accuracy in many applications, earlier work has shown that it does not always lead to measurable benefits for particular classification tasks, specifically when the classification scheme is not designed around surface reflectance (Song et al., 2001; Zhu and Xia, 2023). This research confirms these findings for TOA-optimized systems like SIAM, where corrections remove classification-relevant information.

Future research could aim at improving the integration of SIAM with atmospheric correction workflows. Developing additional BOA-based SIAM variants using atmospherically corrected imagery with reliable reference data would eliminate inconsistencies between TOA-oriented decision rules and surface reflectance input, even though it would probably mean losing atmospheric phenomena detection capability of TOA data. Additionally, adaptive decision trees accounting for seasonal solar geometry variability may help maintain classification stability under different atmospheric and illumination conditions. Considering the fast advancement in machine learning algorithms, a BOA-trained deep learning-based classifier may demonstrate a better tolerance to correction-induced uncertainties. Alternatively, future atmospheric correction algorithms could be designed with greater emphasis on preserving category boundaries rather than focusing on radiometric accuracy. Finally, validation across diverse climatic regions with a BOA-adapted SIAM categorization could help to expand the applicability of the presented findings.

List of references

Arvor, D., Betbeder, J., Daher, F., Blossier, T., Renan, L.R., Corgne, S., Corpetti, T., Silgueiro, V., Silva Junior, C.A., 2021. Towards user-adaptive remote sensing: Knowledge-driven automatic classification of Sentinel-2 time series. Remote Sensing of Environment 264, 112615. https://doi.org/10.1016/j.rse.2021.112615

Augustin, H., Sudmanns, M., Tiede, D., Lang, S., Baraldi, A., 2019. Semantic Earth Observation Data Cubes. Data 4, 102. https://doi.org/10.3390/data4030102

Baetens, L., Desjardins, C., Hagolle, O., 2019. Validation of Copernicus Sentinel-2 Cloud Masks Obtained from MAJA, Sen2Cor, and FMask Processors Using Reference Cloud Masks Generated with a Supervised Active Learning Procedure. Remote Sensing 11, 433. https://doi.org/10.3390/rs11040433

Baraldi, A., 2011. Satellite Image Automatic Mapper™ (SIAM™) - A Turnkey Software Executable for Automatic Near Real-Time Multi-Sensor Multi-Resolution Spectral Rule-Based Preliminary Classification of Spaceborne Multi-Spectral Images. RPTST 1, 81–106. https://doi.org/10.2174/1877611611101020081

Baraldi, A., Humber, M.L., Tiede, D., Lang, S., 2018. GEO-CEOS stage 4 validation of the Satellite Image Automatic Mapper lightweight computer program for ESA Earth observation level 2 product generation - Part 1: Theory. Cogent Geoscience 4, 1467357. https://doi.org/10.1080/23312041.2018.1467357

Ben-Dor, E., 1994. A precaution regarding cirrus cloud detection from airborne imaging spectrometer data using the 1.38 μm water vapor band. Remote Sensing of Environment 50, 346–350. https://doi.org/10.1016/0034-4257(94)90084-1

Bodhaine, B.A., Wood, N.B., Dutton, E.G., Slusser, J.R., 1999. On Rayleigh Optical Depth Calculations. J. Atmos. Oceanic Technol. 16, 1854–1861. https://doi.org/10.1175/1520-0426(1999)016%3C1854:ORODC%3E2.0.CO;2

Bohren, C.F., Huffmann, D.R., 1983. Absorption and Scattering of Light by Small Particles. John Wiley & Sons, New York.

Chandrasekhar, S. (Subrahmanyan), 1960. Radiative transfer. New York : Dover Publications.

Cohen, J., 1960. A coefficient of agreement for nominal scales. Educational and Psychological Measurement 20, 37–46. https://doi.org/10.1177/001316446002000104

Copernicus Atmosphere Monitoring Service, 2020. CAMS global reanalysis (EAC4). Copernicus Atmosphere Monitoring Service (CAMS) Atmosphere Data Store. https://doi.org/DOI:%2010.24381/d58bbf47

Copernicus Data Space Ecosystem, n.d. Copernicus DEM - Global and European Digital Elevation Model | Copernicus Data Space Ecosystem [WWW Document]. URL https://doi.org/10.5270/ESA-c5d3d65 (accessed 1.1.26).

del Rosario González-Moradas, M., Viveen, W., Andrés Vidal-Villalobos, R., Carlos Villegas-Lanza, J., 2023. A performance comparison of SRTM v. 3.0, AW3D30, ASTER

GDEM3, Copernicus and TanDEM-X for tectonogeomorphic analysis in the South American Andes. CATENA 228, 107160. https://doi.org/10.1016/j.catena.2023.107160

Doxani, G., Vermote, E.F., Roger, J.-C., Skakun, S., Gascon, F., Collison, A., De Keukelaere, L., Desjardins, C., Frantz, D., Hagolle, O., Kim, M., Louis, J., Pacifici, F., Pflug, B., Poilvé, H., Ramon, D., Richter, R., Yin, F., 2023. Atmospheric Correction Inter-comparison eXercise, ACIX-II Land: An assessment of atmospheric correction processors for Landsat 8 and Sentinel-2 over land. Remote Sensing of Environment 285, 113412. https://doi.org/10.1016/j.rse.2022.113412

Dozier, J., 1989. Spectral signature of alpine snow cover from the landsat thematic mapper. Remote Sensing of Environment 28, 9–22. https://doi.org/10.1016/0034-4257(89)90101-6

European Centre for Medium-Range Weather Forecasts, 2022. Copernicus Atmosphere Monitoring Service [WWW Document]. URL https://www.ecmwf.int/en/about/what-we-do/environmental-services/copernicus-atmosphere-monitoring-service (accessed 12.31.25).

European Centre for Medium-Range Weather Forecasts, 2017. The ECMWF Copernicus Atmosphere Monitoring Service (CAMS) – applications and recent improvements [WWW Document]. URL https://www.ecmwf.int/en/about/media-centre/focus/2017/ecmwf-copernicus-atmosphere-monitoring-service-cams-applications (accessed 12.31.25).

European Centre for Medium-Range Weather Forecasts, 2016. Atmosphere Monitoring Service makes big strides in first year [WWW Document]. URL https://www.ecmwf.int/en/about/media-centre/news/2016/atmosphere-monitoring-service-makes-big-strides-first-year (accessed 12.31.25).

European Commission - Directorate-General for Defence Industry and Space, n.d. Copernicus | Earth Observation - European Commission [WWW Document]. Use cases. URL https://defence-industry-space.ec.europa.eu/eu-space/copernicus-earth-observation_en (accessed 3.2.25).

European Space Agency, 2025a. S2 Products [WWW Document]. S2 Products. URL https://sentiwiki.copernicus.eu/web/s2-products (accessed 6.29.25).

European Space Agency, 2025b. S2 Mission [WWW Document]. S2 Mission. URL https://sentiwiki.copernicus.eu/web/s2-mission (accessed 11.16.25).

European Space Agency, 2025c. S2 Processing [WWW Document]. S2 Processing. URL https://sentiwiki.copernicus.eu/web/s2-processing (accessed 12.7.25).

European Space Agency, 2021. Sentinel-2 Product Definition and Generation Specification – Level-2A Algorithm Theoretical Basis Document S2-PDGS-MPC-ATBD-L2A (v2.10) [WWW Document]. URL https://sentiwiki.copernicus.eu/__attachments/1692737/S2-PDGS-MPC-ATBD-L2A%20-%20Level%202A%20Algorithm%20Theoretical%20Basis%20Document%202021%20-%202.10.pdf?inst-v=0b38ac37-4dd6-44ba-865b-d9854aa106d8

European Space Agency, 2020. Copernicus Sentinel-5P (processed by ESA) [WWW Document]. URL https://doi.org/10.5270/S5P-ft13p57 (accessed 12.31.25).

European Space Agency, n.d. Sentinel-2 [WWW Document]. The mission. URL https://www.esa.int/Applications/Observing_the_Earth/Copernicus/Sentinel-2 (accessed 3.2.25a).

European Space Agency, n.d. Copernicus Browser [WWW Document]. Copernicus Browser. URL https://browser.dataspace.copernicus.eu/ (accessed 12.27.25b).

European Space Agency, n.d. Sen2Cor v2.12 – STEP. URL https://step.esa.int/main/snap-supported-plugins/sen2cor/sen2cor-v2-12/ (accessed 1.10.26c).

Frantz, D., 2020a. FORCE documentation — FORCE 3.0 documentation [WWW Document]. URL https://force-eo.readthedocs.io/en/latest/index.html (accessed 1.11.26).

Frantz, D., 2020b. Digital Elevation Model — FORCE 3.0 documentation [WWW Document]. URL https://force-eo.readthedocs.io/en/latest/howto/dem.html#tut-dem (accessed 1.1.26).

Frantz, D., 2020c. Level 2 ARD — FORCE 3.0 documentation [WWW Document]. URL https://force-eo.readthedocs.io/en/latest/howto/l2-ard.html (accessed 1.11.26).

Frantz, D., 2019. FORCE—Landsat + Sentinel-2 Analysis Ready Data and Beyond. Remote Sensing 11. https://doi.org/10.3390/rs11091124

Gao, B.-C., Goetz, A.F.H., Wiscombe, W.J., 1993. Cirrus cloud detection from Airborne Imaging Spectrometer data using the 1.38 µm water vapor band. Geophysical Research Letters 20, 301–304. https://doi.org/10.1029/93GL00106

GEOLab, 2021. 3.2. Principles of image analysis — GIS4Schools documentation [WWW Document]. 3.2.1.3. Spectral signatures of the main macro land cover classes. URL https://gis4schools.readthedocs.io/en/latest/part3/rs_imageanalysis.html#fig2-signature (accessed 12.10.25).

Global Modeling and Assimilation Office, n.d. Modern-Era Retrospective analysis for Research and Applications, Version 2 [WWW Document]. URL https://gmao.gsfc.nasa.gov/gmao-products/merra-2/ (accessed 12.31.25).

Haralick, R.M., Sternberg, S.R., Zhuang, X., 1987. Image Analysis Using Mathematical Morphology. IEEE Transactions on Pattern Analysis and Machine Intelligence PAMI-9, 532–550. https://doi.org/10.1109/TPAMI.1987.4767941

Hill, J., Diemer, C., Udelhoven, T., 2003. A local correlation approach for the fusion of image bands with different spatial resolutions, in: Bulletin - Société Française de Photogrammétrie et de Télédétection. Presented at the Séminaire CNES : « Méthodes de fusion multi-résolution pour la synthèse d’images », 16-17 décembre 2002 (CNES, Toulouse), pp. 26–34.

Horvath, H., 1993. Atmospheric light absorption—A review. Atmospheric Environment. Part A. General Topics 27, 293–317. https://doi.org/10.1016/0960-1686(93)90104-7

Inness, A., Ades, M., Agustí-Panareda, A., Barré, J., Benedictow, A., Blechschmidt, A.-M., Dominguez, J.J., Engelen, R., Eskes, H., Flemming, J., Huijnen, V., Jones, L., Kipling, Z., Massart, S., Parrington, M., Peuch, V.-H., Razinger, M., Remy, S., Schulz, M., Suttie, M., 2019. The CAMS reanalysis of atmospheric composition. Atmospheric Chemistry and Physics 19, 3515–3556. https://doi.org/10.5194/acp-19-3515-2019

Interdisciplinary Centre of Competence for Geoinformatics, Z-GIS, University of Salzburg, Spatial Services GmbH, n.d. SIAM (Satellite Image Automatic Mapper) Process and Product Description [WWW Document]. URL https://www.onda-dias.eu/cms/wp-content/uploads/2019/06/SIAM-Process-and-Product-Description-1.pdf

Interdisciplinary Centre of Competence for Geoinformatics, Z-GIS, University of Salzburg, Spatial Services GmbH, n.d. SIAM (Satellite Image Automatic Mapper) Process and Product Description.

Kaufman, Y.J., 1984. Atmospheric effect on spatial resolution of surface imagery: errata. Appl. Opt., AO 23, 3400–3408. https://doi.org/10.1364/AO.23.004164

Kaufman, Y.J., Sendra, C., 1988. Algorithm for automatic atmospheric corrections to visible and near-IR satellite imagery. International Journal of Remote Sensing 9, 1357–1381. https://doi.org/10.1080/01431168808954942

Kganyago, M., Ovakoglou, G., Mhangara, P., Alexandridis, T., Odindi, J., Adjorlolo, C., Mashiyi, N., 2020. Validation of atmospheric correction approaches for Sentinel-2 under partly-cloudy conditions in an African agricultural landscape, in: Comerón, A., Kassianov, E.I., Schäfer, K., Picard, R.H., Weber, K., Singh, U.N. (Eds.), Remote Sensing of Clouds and the Atmosphere XXV. Presented at the Remote Sensing of Clouds and the Atmosphere XXV, SPIE, Online Only, United Kingdom, p. 9. https://doi.org/10.1117/12.2572293

Klassen, R.V., 1987. Modeling the effect of the atmosphere on light. ACM Trans. Graph. 6, 215–237. https://doi.org/10.1145/35068.35071

Le Hégarat-Mascle, S., André, C., 2009. Use of Markov Random Fields for automatic cloud/shadow detection on high resolution optical images. ISPRS Journal of Photogrammetry and Remote Sensing 64, 351–366. https://doi.org/10.1016/j.isprsjprs.2008.12.007

Li, B., Yuan, H., Feng, N., Tao, S., 2009. Comparing MODIS and AERONET aerosol optical depth over China. International Journal of Remote Sensing 30, 6519–6529. https://doi.org/10.1080/01431160903111069

Lyapustin, A.I., Kaufman, Y.J., 2001. Role of adjacency effect in the remote sensing of aerosol. Journal of Geophysical Research: Atmospheres 106, 11909–11916. https://doi.org/10.1029/2000JD900647

Main-Knorn, M., Pflug, B., Debaecker, V., Louis, J., 2015. CALIBRATION AND VALIDATION PLAN FOR THE L2A PROCESSOR AND PRODUCTS OF THE SENTINEL-2 MISSION. Int. Arch. Photogramm. Remote Sens. Spatial Inf. Sci. XL-7/W3, 1249–1255. https://doi.org/10.5194/isprsarchives-XL-7-W3-1249-2015

Main-Knorn, M., Pflug, B., Louis, J., Debaecker, V., Müller-Wilm, U., Gascon, F., 2017. Sen2Cor for Sentinel-2, in: Bruzzone, L., Bovolo, F., Benediktsson, J.A. (Eds.), Image and Signal Processing for Remote Sensing XXIII. Presented at the Image and Signal Processing for Remote Sensing, SPIE, Warsaw, Poland. https://doi.org/10.1117/12.2278218

Major, D., Horváth, Z., Kröber, F., Augustin, H., Sudmanns, M., Ševčík, P., Baraldi, A., Berg, A., Cornel, D., Tiede, D., 2025. A holistic approach for multi-spectral Sentinel-2 super-resolution and spectral evaluation. International Journal of Remote Sensing 46, 7437–7464. https://doi.org/10.1080/01431161.2025.2549132

Mayer, B., Kylling, A., 2005. Technical note: The libRadtran software package for radiative transfer calculations - description and examples of use. Atmospheric Chemistry and Physics 5, 1855–1877. https://doi.org/10.5194/acp-5-1855-2005

Meadows, M., Jones, S., Reinke, K., 2024. Vertical accuracy assessment of freely available global DEMs (FABDEM, Copernicus DEM, NASADEM, AW3D30 and SRTM) in flood-prone environments. International Journal of Digital Earth 17, 2308734. https://doi.org/10.1080/17538947.2024.2308734

Mekler, Y., Kaufman, Y.J., 1980. The effect of Earth's atmosphere on contrast reduction·for a nonuniform surface albedo and 'two-halves' field. Journal of Geophysical Research: Oceans 85, 4067–4083. https://doi.org/10.1029/JC085iC07p04067

Mie, G., 1908. Beiträge zur Optik trüber Medien, speziell kolloidaler Metallösungen. Annalen der Physik, Vierte Folge Band 25, No. 3, 377–445.

NASA/METI/AIST/Japan Spacesystems and U.S./Japan ASTER Science Team, 2019. ASTER Global Digital Elevation Model V003. https://doi.org/https://doi.org/10.5067/ASTER/ASTGTM.003

National Aeronautics and Space Administration, n.d. MODIS Moderate Resolution Imaging Spectroradiometer) [WWW Document]. About. URL https://modis.gsfc.nasa.gov/about/ (accessed 12.31.25).

Otterman, J., Ungar, S., Kaufman, Y., Podolak, M., 1980. Atmospheric effects on radiometric imaging from satellites under low optical thickness conditions. Remote Sensing of Environment 9, 115–129. https://doi.org/10.1016/0034-4257(80)90003-6

Qin, W., Herman, J.R., Ahmad, Z., 2001. A fast, accurate algorithm to account for non-Lambertian surface effects on TOA radiance. Journal of Geophysical Research: Atmospheres 106, 22671–22684. https://doi.org/10.1029/2001JD900215

Qiu, S., Zhu, Z., He, B., 2019. Fmask 4.0: Improved cloud and cloud shadow detection in Landsats 4–8 and Sentinel-2 imagery. Remote Sensing of Environment 231, 111205. https://doi.org/10.1016/j.rse.2019.05.024

Qiu, S., Zhu, Z., Woodcock, C.E., 2020. Cirrus clouds that adversely affect Landsat 8 images: What are they and how to detect them? Remote Sensing of Environment 246, 111884. https://doi.org/10.1016/j.rse.2020.111884

Qu, Y., 2018. Sea Surface Albedo, in: Comprehensive Remote Sensing. Elsevier, pp. 163–185. https://doi.org/10.1016/B978-0-12-409548-9.10371-9

Rahman, H., and Dedieu, G., 1994. SMAC: a simplified method for the atmospheric correction of satellite measurements in the solar spectrum. International Journal of Remote Sensing 15, 123–143. https://doi.org/10.1080/01431169408954055

Raiyani, K., Gonçalves, T., Rato, L., Salgueiro, P., Marques da Silva, J.R., 2021. Sentinel-2 Image Scene Classification: A Comparison between Sen2Cor and a Machine Learning Approach. Remote Sensing 13, p.3. https://doi.org/10.3390/rs13020300

Riano, D., Chuvieco, E., Salas, J., Aguado, I., 2003. Assessment of different topographic corrections in Landsat-TM data for mapping vegetation types (2003). IEEE Transactions on Geoscience and Remote Sensing 41, 1056–1061. https://doi.org/10.1109/TGRS.2003.811693

Richter, R., Kellenberger, T., Kaufmann, H., 2009. Comparison of Topographic Correction Methods. Remote Sensing 1, 184–196. https://doi.org/10.3390/rs1030184

Rottman, G., 2007. Measurement of Total and Spectral Solar Irradiance. Space Sci Rev 125, 39–51. https://doi.org/10.1007/s11214-006-9045-6

Rumora, L., Miler, M., Medak, D., 2020. Impact of Various Atmospheric Corrections on Sentinel-2 Land Cover Classification Accuracy Using Machine Learning Classifiers. ISPRS International Journal of Geo-Information 9, p.1. https://doi.org/10.3390/ijgi9040277

Sanchez, A.H., Picoli, M.C.A., Camara, G., Andrade, P.R., Chaves, M.E.D., Lechler, S., Soares, A.R., Marujo, R.F.B., Simões, R.E.O., Ferreira, K.R., Queiroz, G.R., 2020. Comparison of Cloud Cover Detection Algorithms on Sentinel–2 Images of the Amazon Tropical Forest. Remote Sensing 12, 1284. https://doi.org/10.3390/rs12081284

Schläpfer, D., Borel, C.C., Keller, J., Itten, K.I., 1998. Atmospheric Precorrected Differential Absorption Technique to Retrieve Columnar Water Vapor. Remote Sensing of Environment 65, 353–366. https://doi.org/10.1016/S0034-4257(98)00044-3

Shen, A., Shao, J., Qi, X., Zhu, Z., Dai, Y., Zeng, Q., 2025. BRDF Correction in Landsat Directional Reflectance Data by Combining Optimal BRDF Archetype With Spectral Characteristics. IEEE J. Sel. Top. Appl. Earth Observations Remote Sensing 18, 17592–17609. https://doi.org/10.1109/JSTARS.2025.3586463

Simard, M., Denbina, M., Marshak, C., Neumann, M., 2024. A Global Evaluation of Radar-Derived Digital Elevation Models: SRTM, NASADEM, and GLO-30. JGR Biogeosciences 129, e2023JG007672. https://doi.org/10.1029/2023JG007672

Sola, I., García-Martín, A., Sandonís-Pozo, L., Álvarez-Mozos, J., Pérez-Cabello, F., González-Audícana, M., Montorio Llovería, R., 2018. Assessment of atmospheric correction methods for Sentinel-2 images in Mediterranean landscapes. International Journal of Applied Earth Observation and Geoinformation 73, 63–76. https://doi.org/10.1016/j.jag.2018.05.020

Song, C., Woodcock, C.E., Seto, K.C., Lenney, M.P., Macomber, S.A., 2001. Classification and Change Detection Using Landsat TM Data: When and How to Correct Atmospheric Effects? Remote Sensing of Environment 75, 230–244. https://doi.org/10.1016/S0034-4257(00)00169-3

Statella, T., Erivaldo, A. da S., 2008. SHADOWS AND CLOUDS DETECTION IN HIGH RESOLUTION IMAGES USING MATHEMATICAL MORPHOLOGY.

Strutt (Lord Rayleigh), J.W., 1871. On the light from the sky, its polarization and colour. Philos. Mag. 41, 107–120, 274–279.

United States Geological Survey, 2018. USGS EROS Archive - Digital Elevation - Shuttle Radar Topography Mission (SRTM) 1 Arc-Second Global | U.S. Geological Survey [WWW Document]. URL https://doi.org/10.5066/F7PR7TFT (accessed 1.1.26).

V. V. Sobolev, 1975. Light Scattering In Planetary Atmospheres.

Vermote, E.F., Tanre, D., Deuze, J.L., Herman, M., Morcette, J.-J., 1997. Second Simulation of the Satellite Signal in the Solar Spectrum, 6S: an overview. IEEE Transactions on Geoscience and Remote Sensing 35, 675–686. https://doi.org/10.1109/36.581987

Wei, X., Chang, N.-B., Bai, K., Gao, W., 2020. Satellite remote sensing of aerosol optical depth: advances, challenges, and perspectives. Critical Reviews in Environmental Science and Technology 50, 1640–1725. https://doi.org/10.1080/10643389.2019.1665944

Wilson, R., 2026. robintw/Py6S.

Wilson, R.T., 2013. Py6S: A Python interface to the 6S radiative transfer model. Computers & Geosciences 51, 166–171. https://doi.org/10.1016/j.cageo.2012.08.002

Young, A.T., 1982. Rayleigh scattering. Physics today 35, 42–48.

Zhu, W., Xia, W., 2023. Effects of Atmospheric Correction on Remote Sensing Statistical Inference in an Aquatic Environment. Remote Sensing 15. https://doi.org/10.3390/rs15071907

Zhu, Z., Woodcock, C.E., 2012. Object-based cloud and cloud shadow detection in Landsat imagery. Remote Sensing of Environment 118, 83–94. https://doi.org/10.1016/j.rse.2011.10.028

Zupanc, A., 2020. Improving Cloud Detection with Machine Learning. Planet Stories. URL https://medium.com/sentinel-hub/improving-cloud-detection-with-machine-learning-c09dc5d7cf13 (accessed 12.20.25).

Appendices

Appendix A – Sentinel-2 L1C data used in this study

Table A1 - Sentinel-2 (L1C) product identifier list used in this study

Region	Season	Product identifier
Alpine valleys	Spring	S2B_MSIL1C_20210531T101559_N0500_R065_T32TPT_20230228T151433.SAFE
	Summer	S2A_MSIL1C_20230715T101601_N0509_R065_T32TPT_20230715T140208.SAFE
	Autumn	S2A_MSIL1C_20231013T101951_N0510_R065_T32TPT_20241102T190646.SAFE
	Winter	S2B_MSIL1C_20220126T102209_N0510_R065_T32TPT_20240506T060628.SAFE
High Alps	Spring	S2A_MSIL1C_20190524T101031_N0500_R022_T32TQT_20221209T052220.SAFE
	Summer	S2A_MSIL1C_20190723T101031_N0500_R022_T32TQT_20230718T015529.SAFE
	Autumn	S2B_MSIL1C_20211015T101029_N0500_R022_T32TQT_20230109T030137.SAFE
	Winter	S2A_MSIL1C_20240128T101301_N0510_R022_T32TQT_20240128T105717.SAFE
Pre-Alps	Spring	S2B_MSIL1C_20230528T100559_N0509_R022_T33UUP_20230528T121146.SAFE
	Summer	S2B_MSIL1C_20240721T100559_N0510_R022_T33UUP_20240721T121133.SAFE
	Autumn	S2B_MSIL1C_20241009T100829_N0511_R022_T33UUP_20241009T124639.SAFE
	Winter	S2A_MSIL1C_20240128T101301_N0510_R022_T33UUP_20240128T105717.SAFE
Eastern planes	Spring	S2B_MSIL1C_20230522T094549_N0510_R079_T33TXN_20240906T072736.SAFE
	Summer	S2A_MSIL1C_20240730T095031_N0511_R079_T33TXN_20240730T133103.SAFE
	Autumn	S2A_MSIL1C_20231014T095031_N0510_R079_T33TXN_20241103T004433.SAFE
	Winter	S2A_MSIL1C_20200123T095311_N0500_R079_T33TXN_20230426T173845.SAFE

Table A2 - Sentinel-2 (L2A) product identifier list used in this study

Region	Season	Product identifier
Alpine valleys	Spring	S2B_MSIL2A_20210531T101559_N0500_R065_T32TPT_20230301T002441.SAFE
	Summer	S2A_MSIL2A_20230715T101601_N0509_R065_T32TPT_20230715T164102.SAFE
	Autumn	S2A_MSIL2A_20231013T101951_N0509_R065_T32TPT_20231013T162457.SAFE
	Winter	S2B_MSIL2A_20220126T102209_N0510_R065_T32TPT_20240506T092711.SAFE
High Alps	Spring	S2A_MSIL2A_20190524T101031_N0500_R022_T32TQT_20221209T143154.SAFE
	Summer	S2A_MSIL2A_20190723T101031_N0500_R022_T32TQT_20230719T012350.SAFE
	Autumn	S2B_MSIL2A_20211015T101029_N0500_R022_T32TQT_20230109T121420.SAFE
	Winter	S2A_MSIL2A_20240128T101301_N0510_R022_T32TQT_20240128T121856.SAFE
Pre-Alps	Spring	S2B_MSIL2A_20230528T100559_N0509_R022_T33UUP_20230528T131159.SAFE
	Summer	S2B_MSIL2A_20240721T100559_N0510_R022_T33UUP_20240721T125344.SAFE
	Autumn	S2B_MSIL2A_20241009T100829_N0511_R022_T33UUP_20241009T132806.SAFE
	Winter	S2A_MSIL2A_20240128T101301_N0510_R022_T33UUP_20240128T121856.SAFE
Eastern planes	Spring	S2B_MSIL2A_20230522T094549_N0509_R079_T33TXN_20230522T113408.SAFE
	Summer	S2A_MSIL2A_20240730T095031_N0511_R079_T33TXN_20240730T155453.SAFE
	Autumn	S2A_MSIL2A_20231014T095031_N0510_R079_T33TXN_20241103T055952.SAFE
	Winter	S2A_MSIL2A_20200123T095311_N0500_R079_T33TXN_20230427T041459.SAFE

Appendix B – FORCE parameter file

```
++PARAM_LEVEL2_START++

# INPUT/OUTPUT DIRECTORIES
FILE_QUEUE = /data/force/level1/queue.txt
DIR_LEVEL2 = /data/force/level2
DIR_LOG = /data/force/log
DIR_PROVENANCE = /data/force/provenance
DIR_TEMP = /data/force/temp

# MASKING
FILE_AOI = NULL

# DIGITAL ELEVATION MODEL
FILE_DEM = /data/force/dem/austria.tif
DEM_NODATA = -32767

# DATA CUBES
DO_REPROJ = FALSE
DO_TILE = FALSE
FILE_TILE = NULL
TILE_SIZE = 30000
BLOCK_SIZE = 3000
RESOLUTION_LANDSAT = 30
RESOLUTION_SENTINEL2 = 10
ORIGIN_LON = -25
ORIGIN_LAT = 60
PROJECTION = GLANCE7
RESAMPLING = CC

# RADIOMETRIC CORRECTION OPTIONS
DO_ATMO = TRUE
DO_TOPO = TRUE
DO_BRDF = TRUE
ADJACENCY_EFFECT = TRUE
MULTI_SCATTERING = TRUE

# WATER VAPOR CORRECTION OPTIONS
DIR_WVPLUT = NULL
```

```
STRICT_WATER_VAPOR = FALSE
WATER_VAPOR = NULL

# AEROSOL OPTICAL DEPTH OPTIONS
DO_AOD  = TRUE
DIR_AOD  = NULL

# CLOUD DETECTION OPTIONS
ERASE_CLOUDS = FALSE
MAX_CLOUD_COVER_FRAME = 75
MAX_CLOUD_COVER_TILE  = 75
CLOUD_BUFFER  = 300
CIRRUS_BUFFER = 0
SHADOW_BUFFER = 90
SNOW_BUFFER   = 30
CLOUD_THRESHOLD  = 0.225
SHADOW_THRESHOLD = 0.02

# RESOLUTION MERGING
RES_MERGE = REGRESSION

# CO-REGISTRATION OPTIONS
DIR_COREG_BASE = NULL
COREG_BASE_NODATA = -9999

# MISCELLANEOUS OPTIONS
IMPULSE_NOISE = TRUE
BUFFER_NODATA = FALSE

# TIER LEVEL
TIER = 1

# PARALLEL PROCESSING
NPROC = 1
NTHREAD = 2
PARALLEL_READS = FALSE
DELAY = 3
TIMEOUT_ZIP = 30

# OUTPUT OPTIONS
```

OUTPUT_FORMAT = GTiff
FILE_OUTPUT_OPTIONS = NULL
OUTPUT_DST = FALSE
OUTPUT_AOD = FALSE
OUTPUT_WVP = FALSE
OUTPUT_VZN = FALSE
OUTPUT_HOT = FALSE
OUTPUT_OVV = TRUE

++PARAM_LEVEL2_END++

Appendix C – Alpine valleys – Class (category) distribution (from top to bottom: winter, spring, summer, autumn)

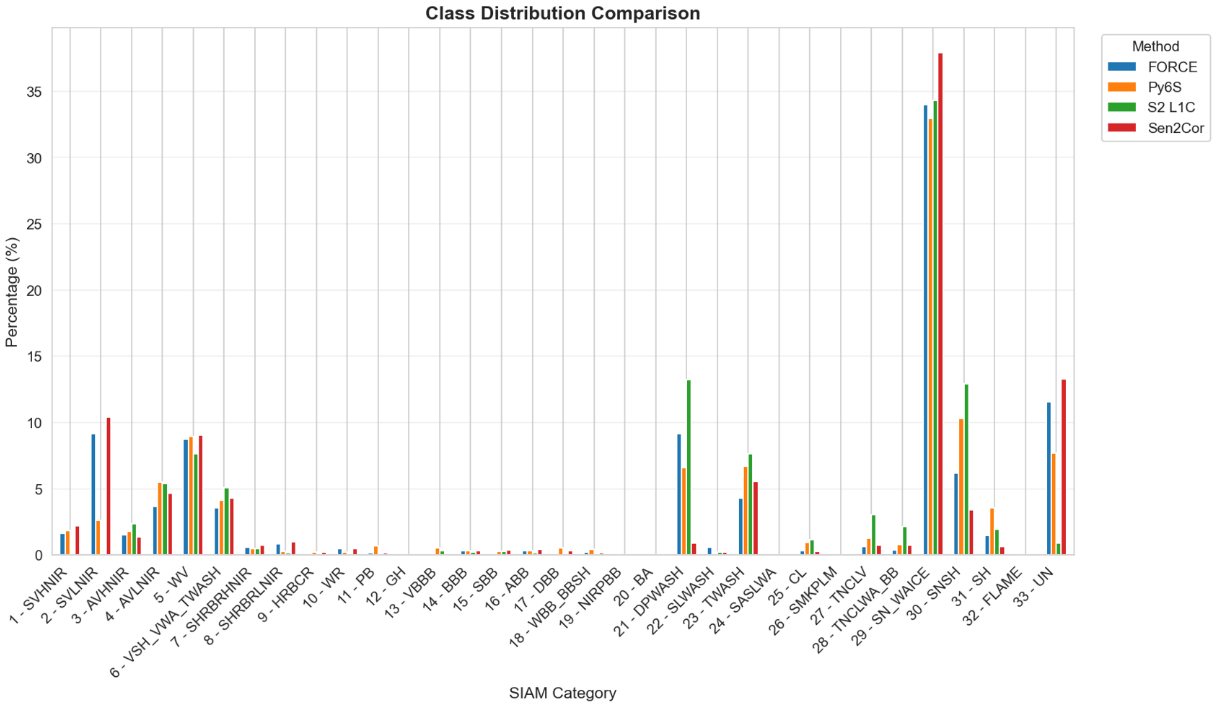

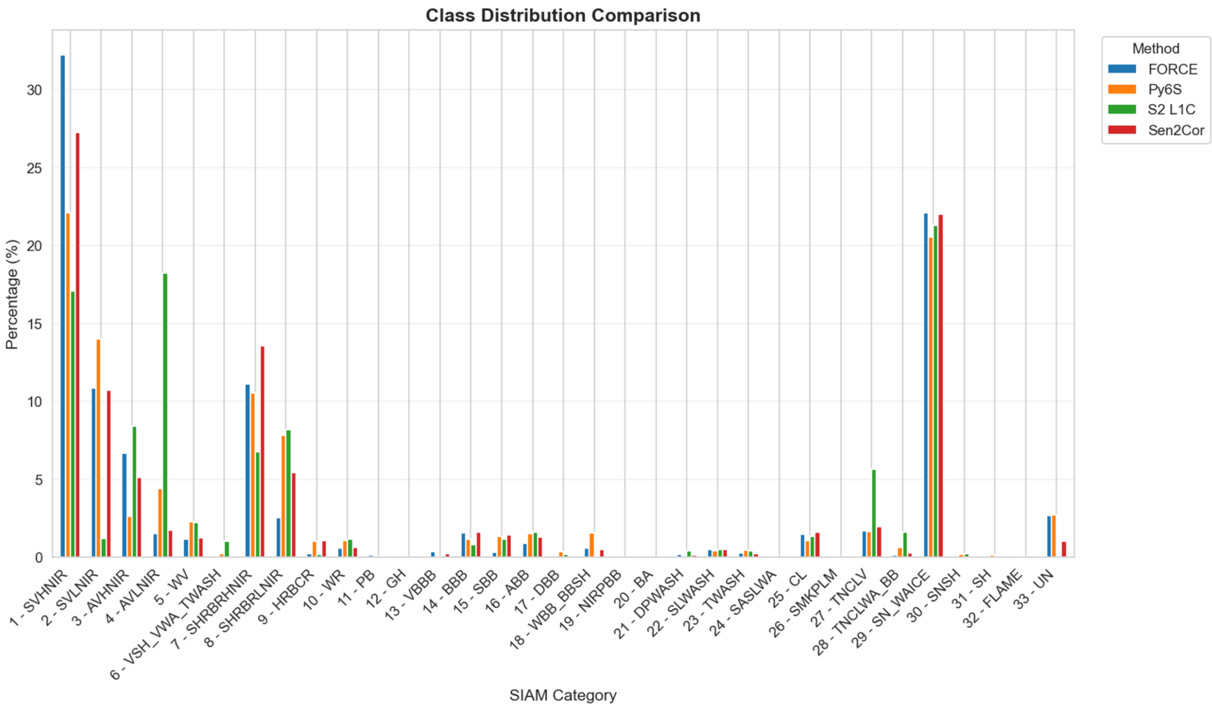

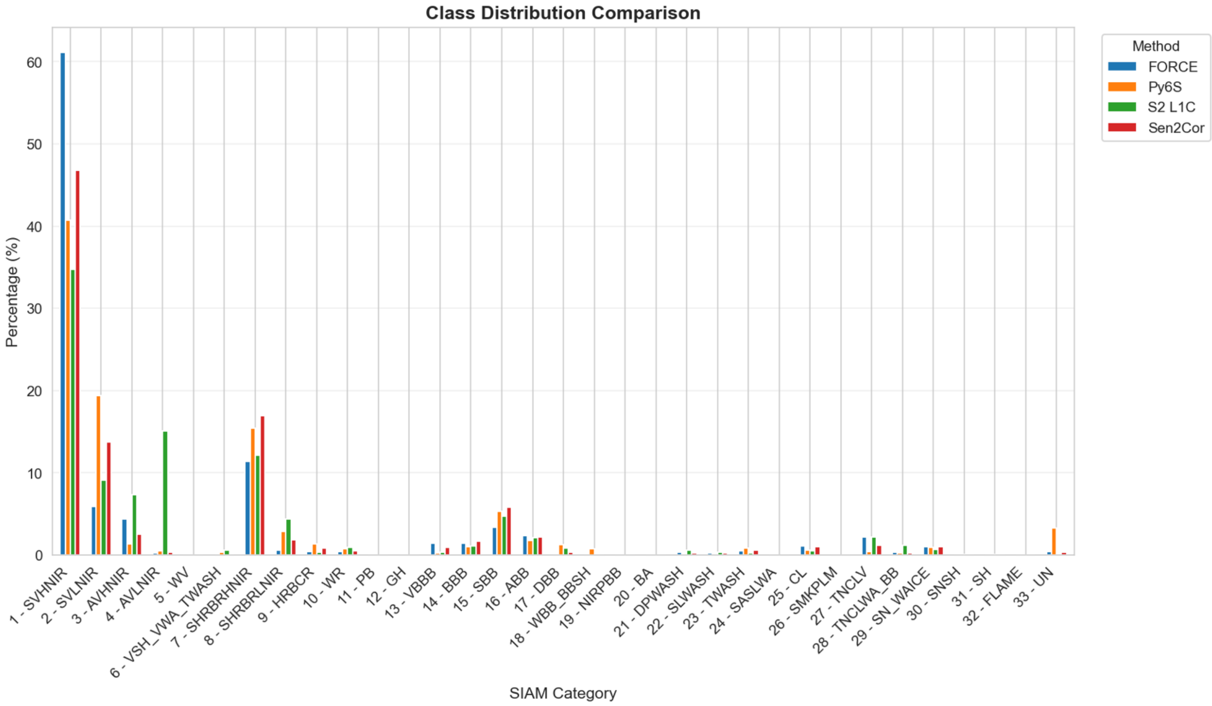

Class Distribution Comparison
Percentage (%)
SIAM Category
Method
FORCE
Py6S
S2 L1C
Sen2Cor
1 - SVHNIR
2 - SVLNIR
3 - AVHNIR
4 - AVLNIR
5 - WV
6 - VSH_VWA_TWASH
7 - SHRBRHNIR
8 - SHRBRLNIR
9 - HRBCR
10 - WR
11 - PB
12 - GH
13 - VBBB
14 - BBB
15 - SBB
16 - ABB
17 - DBB
18 - WBB_BBSH
19 - NIRPBB
20 - BA
21 - DPWASH
22 - SLWASH
23 - TWASH
24 - SASLWA
25 - CL
26 - SMKPLM
27 - TNCLV
28 - TNCLWA_BB
29 - SN_WAICE
30 - SNSH
31 - SH
32 - FLAME
33 - UN

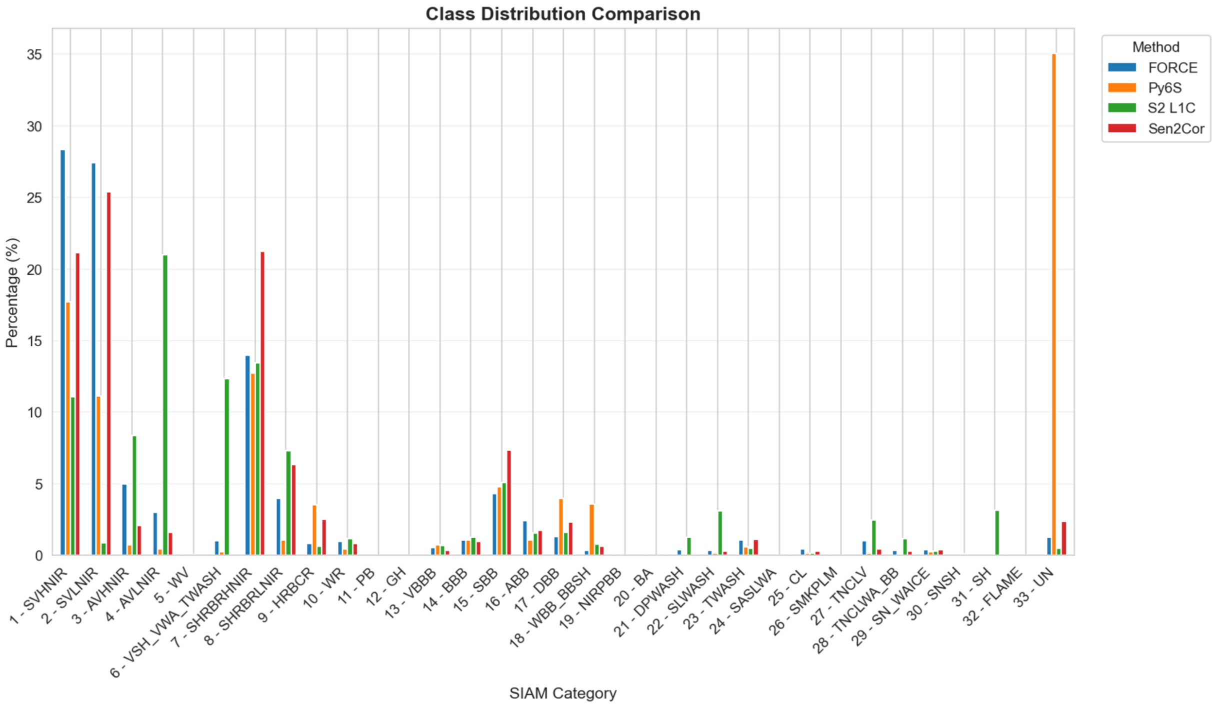

Class Distribution Comparison
Percentage (%)
SIAM Category
Method
FORCE
Py6S
S2 L1C
Sen2Cor
1 - SVHNIR
2 - SVLNIR
3 - AVHNIR
4 - AVLNIR
5 - WV
6 - VSH_VWA_TWASH
7 - SHRBRHNIR
8 - SHRBRLNIR
9 - HRBCR
10 - WR
11 - PB
12 - GH
13 - VBBB
14 - BBB
15 - SBB
16 - ABB
17 - DBB
18 - WBB_BBSH
19 - NIRPBB
20 - BA
21 - DPWASH
22 - SLWASH
23 - TWASH
24 - SASLWA
25 - CL
26 - SMKPLM
27 - TNCLV
28 - TNCLWA_BB
29 - SN_WAICE
30 - SNSH
31 - SH
32 - FLAME
33 - UN

Appendix D – High Alps – Class (category) distribution (from top to bottom: winter, spring, summer, autumn)

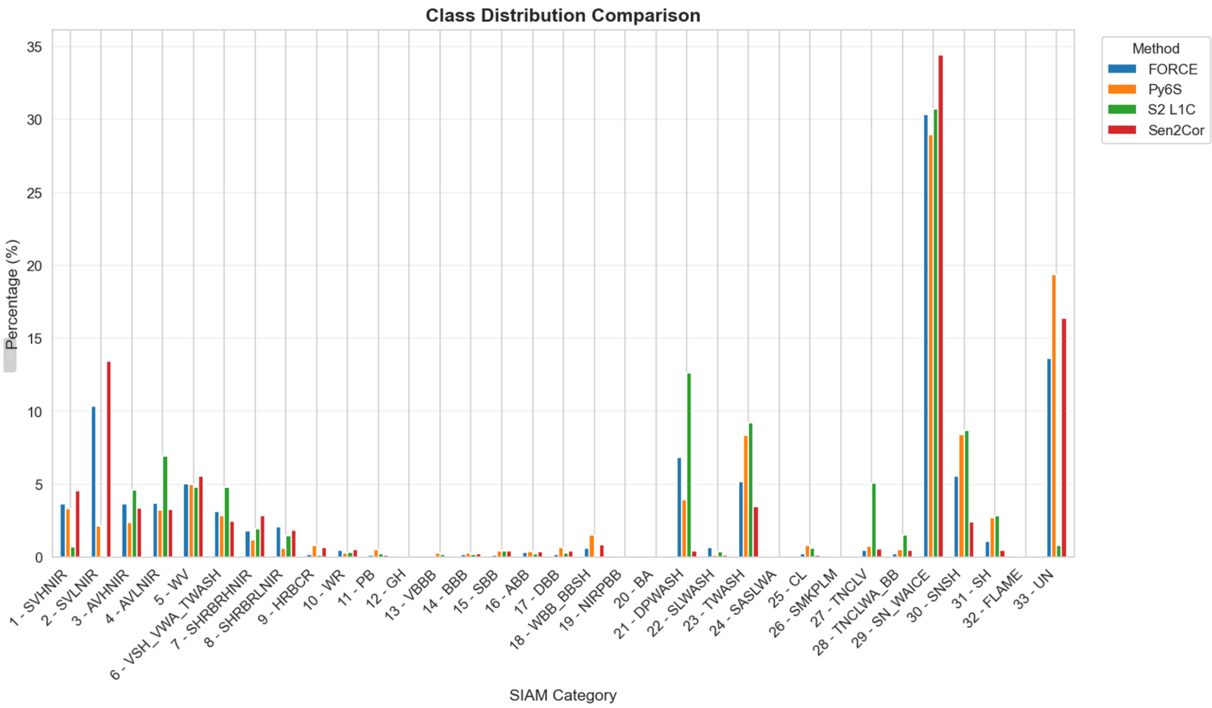

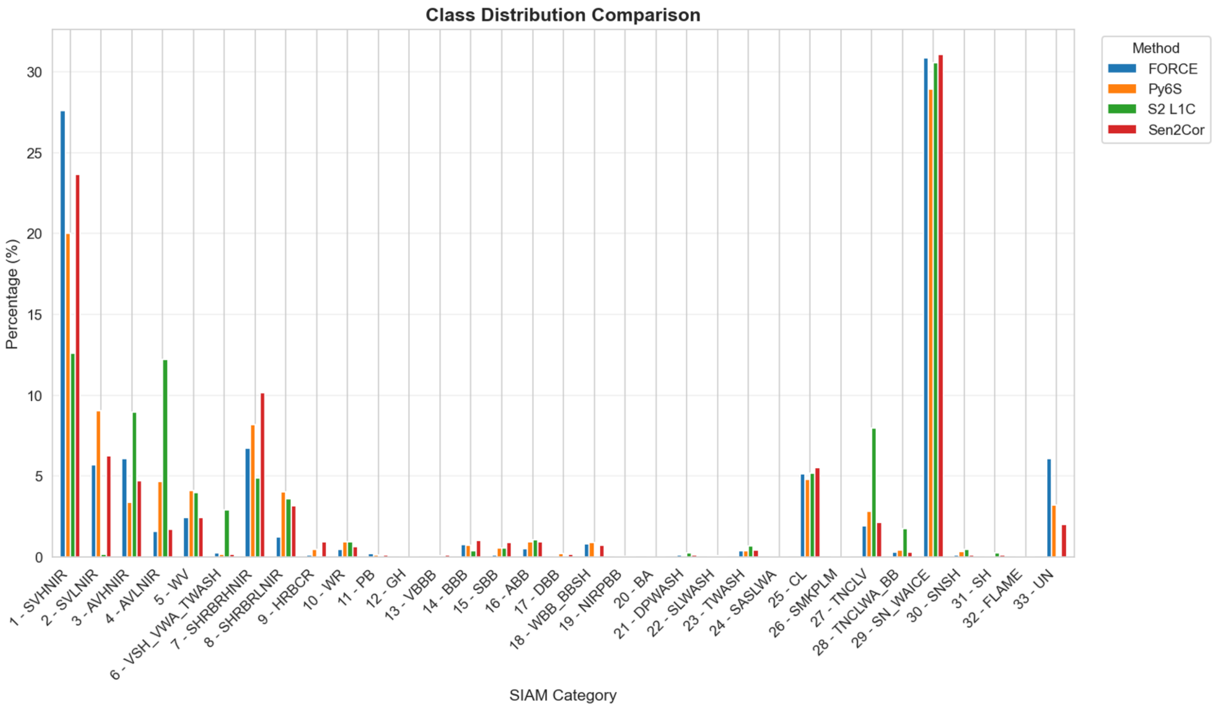

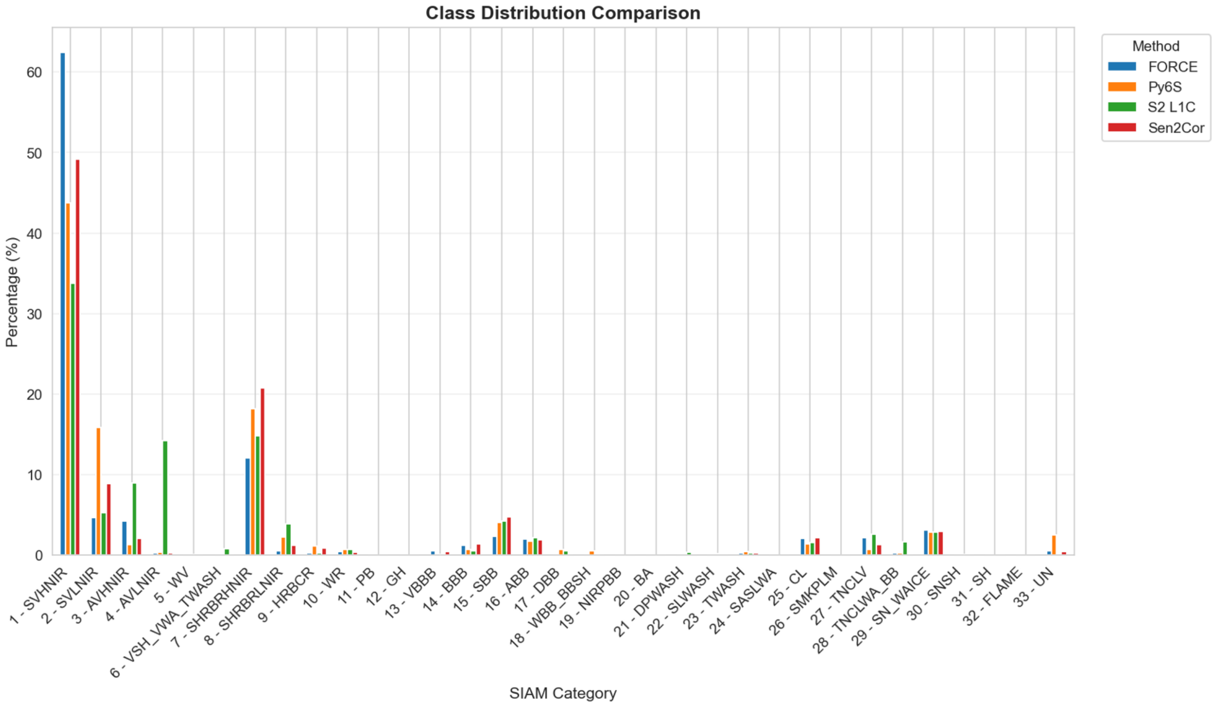
Class Distribution Comparison
Method
FORCE
Py6S
S2 L1C
Sen2Cor
Percentage (%)
SIAM Category
1 - SVHNIR
2 - SVLNIR
3 - AVHNIR
4 - AVLNIR
5 - WV
6 - VSH_VWA_TWASH
7 - SHRBRHNIR
8 - SHRBRLNIR
9 - HRBCR
10 - WR
11 - PB
12 - GH
13 - VBBB
14 - BBB
15 - SBB
16 - ABB
17 - DBB
18 - WBB_BBSH
19 - NIRPBB
20 - BA
21 - DPWASH
22 - SLWASH
23 - TWASH
24 - SASLWA
25 - CL
26 - SMKPLM
27 - TNCLV
28 - TNCLWA_BB
29 - SN_WAICE
30 - SNSH
31 - SH
32 - FLAME
33 - UN

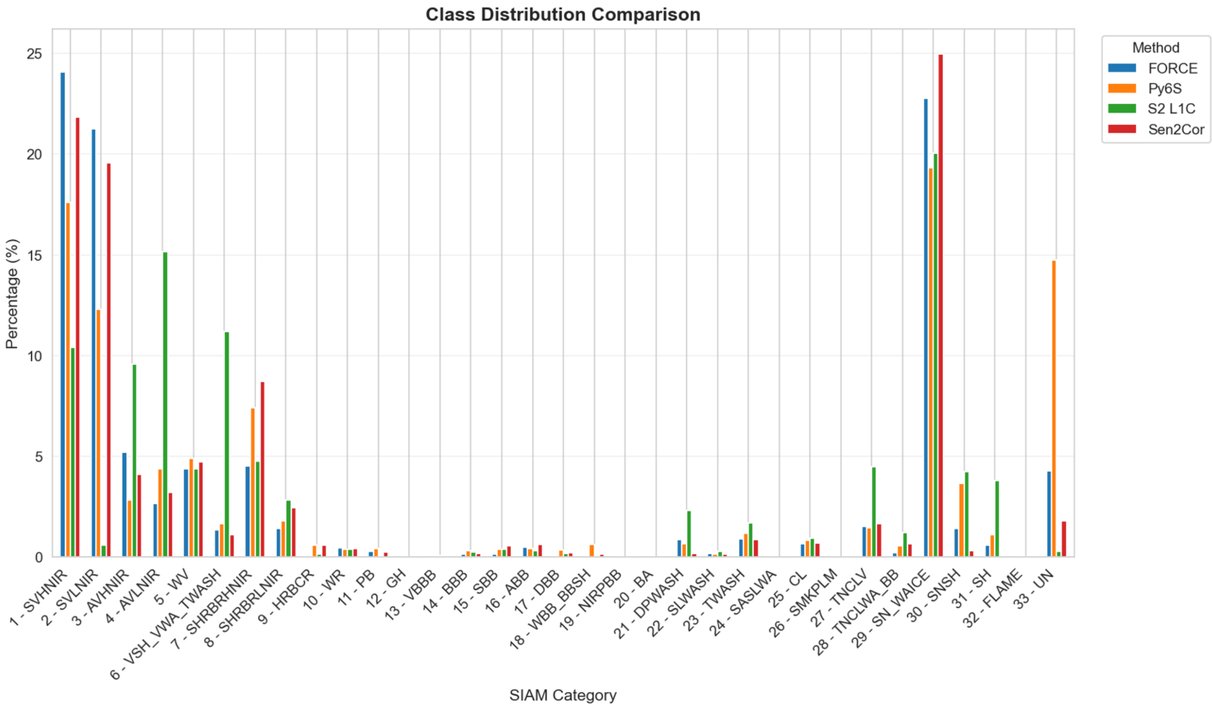
Class Distribution Comparison
Method
FORCE
Py6S
S2 L1C
Sen2Cor
Percentage (%)
SIAM Category
1 - SVHNIR
2 - SVLNIR
3 - AVHNIR
4 - AVLNIR
5 - WV
6 - VSH_VWA_TWASH
7 - SHRBRHNIR
8 - SHRBRLNIR
9 - HRBCR
10 - WR
11 - PB
12 - GH
13 - VBBB
14 - BBB
15 - SBB
16 - ABB
17 - DBB
18 - WBB_BBSH
19 - NIRPBB
20 - BA
21 - DPWASH
22 - SLWASH
23 - TWASH
24 - SASLWA
25 - CL
26 - SMKPLM
27 - TNCLV
28 - TNCLWA_BB
29 - SN_WAICE
30 - SNSH
31 - SH
32 - FLAME
33 - UN

Appendix E – Pre-Alps – Class (category) distribution (from top to bottom: winter, spring, summer, autumn)

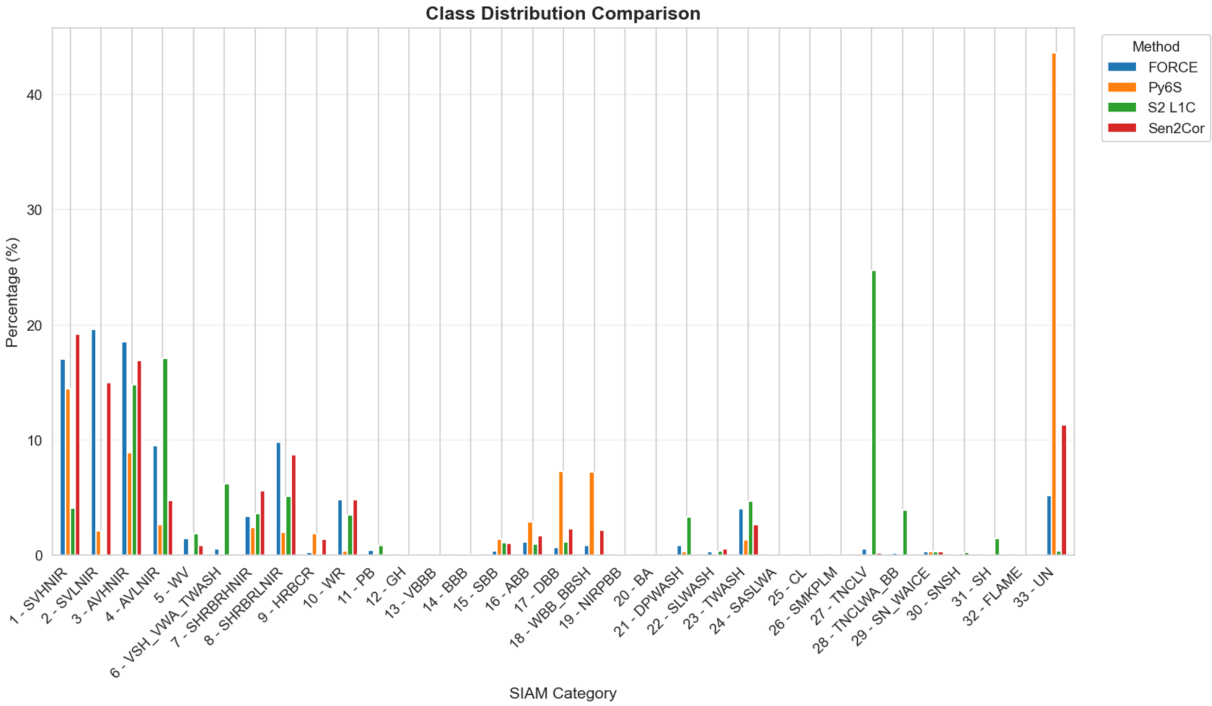

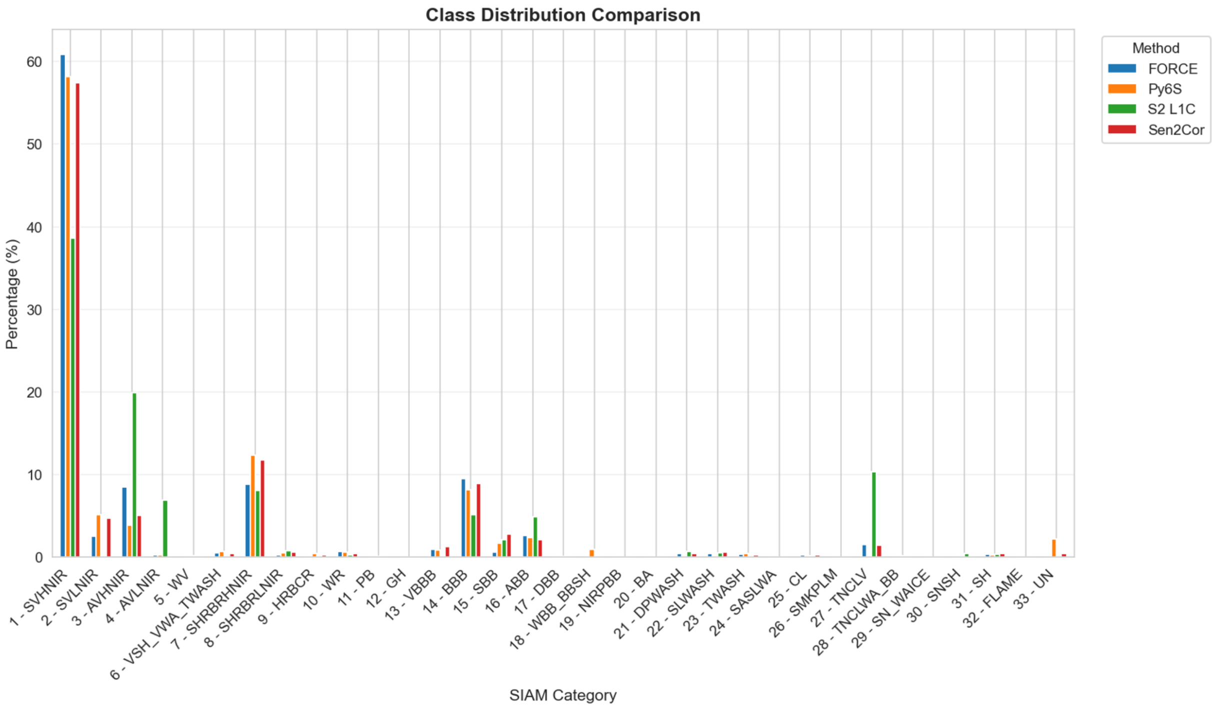

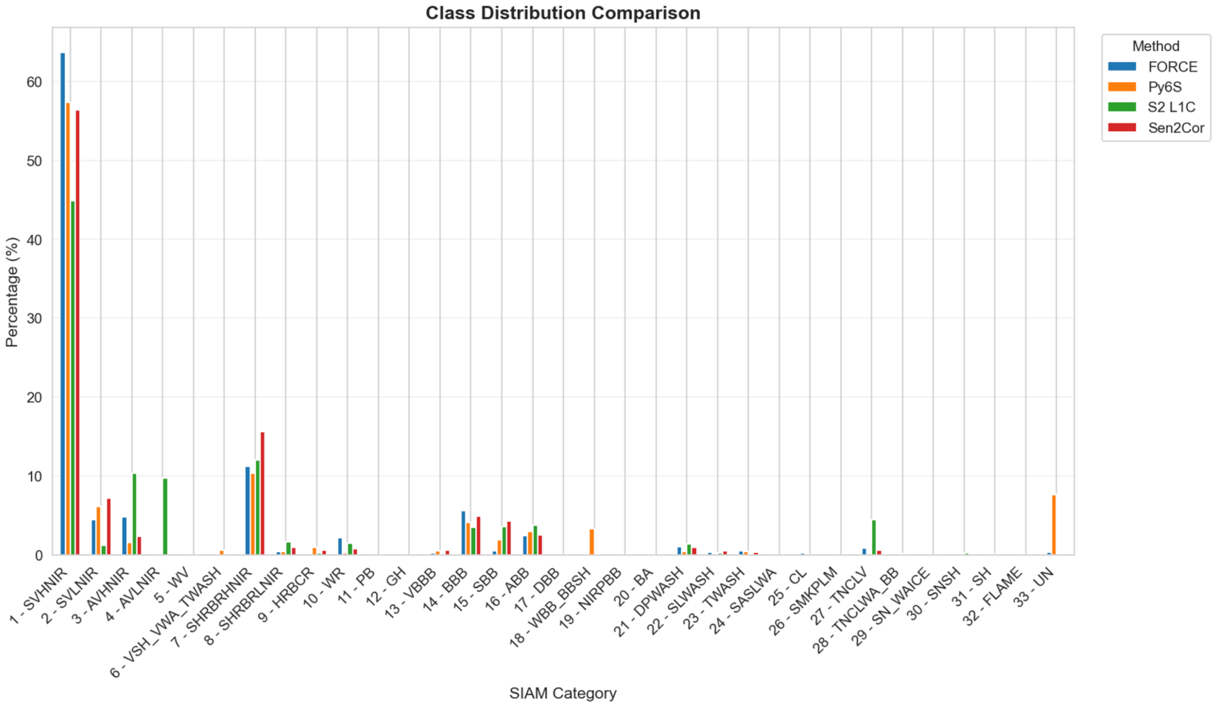

Class Distribution Comparison
Percentage (%)
SIAM Category
Method
FORCE
Py6S
S2 L1C
Sen2Cor
1 - SVHNIR
2 - SVLNIR
3 - AVHNIR
4 - AVLNIR
5 - WV
6 - VSH_VWA_TWASH
7 - SHRBRHNIR
8 - SHRBRLNIR
9 - HRBCR
10 - WR
11 - PB
12 - GH
13 - VBBB
14 - BBB
15 - SBB
16 - ABB
17 - DBB
18 - WBB_BBSH
19 - NIRPBB
20 - BA
21 - DPWASH
22 - SLWASH
23 - TWASH
24 - SASLWA
25 - CL
26 - SMKPLM
27 - TNCLV
28 - TNCLWA_BB
29 - SN_WAICE
30 - SNSH
31 - SH
32 - FLAME
33 - UN

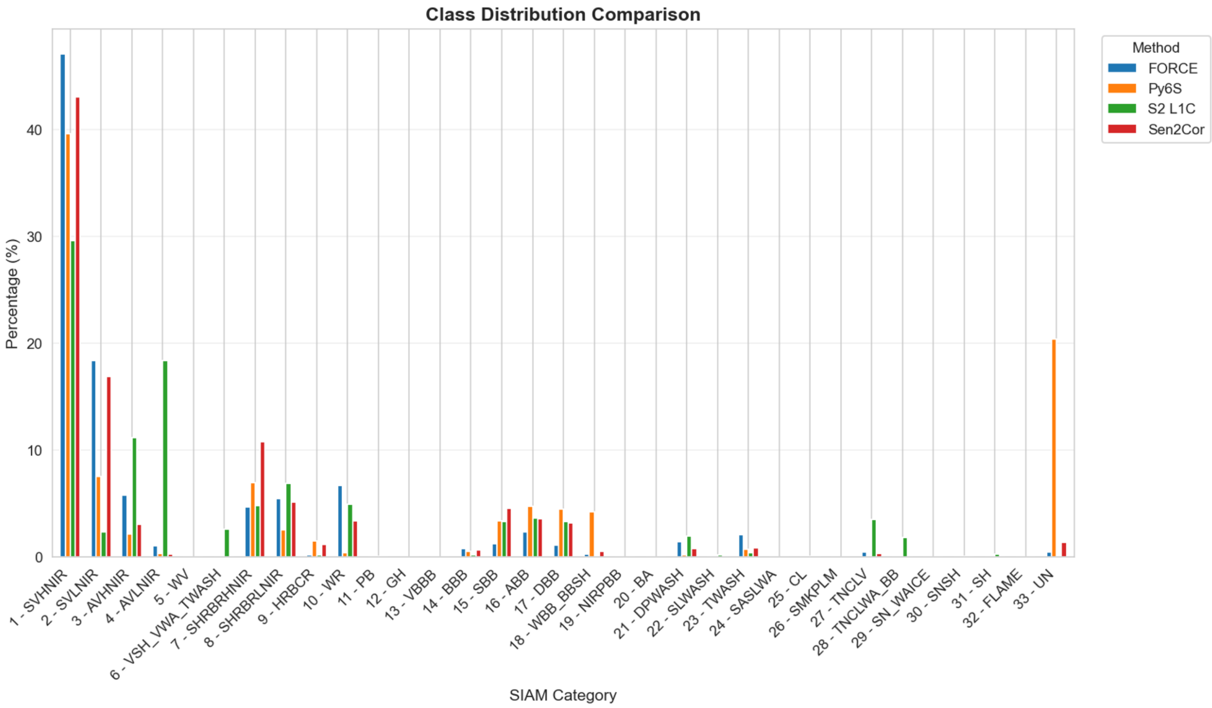

Class Distribution Comparison
Percentage (%)
SIAM Category
Method
FORCE
Py6S
S2 L1C
Sen2Cor
1 - SVHNIR
2 - SVLNIR
3 - AVHNIR
4 - AVLNIR
5 - WV
6 - VSH_VWA_TWASH
7 - SHRBRHNIR
8 - SHRBRLNIR
9 - HRBCR
10 - WR
11 - PB
12 - GH
13 - VBBB
14 - BBB
15 - SBB
16 - ABB
17 - DBB
18 - WBB_BBSH
19 - NIRPBB
20 - BA
21 - DPWASH
22 - SLWASH
23 - TWASH
24 - SASLWA
25 - CL
26 - SMKPLM
27 - TNCLV
28 - TNCLWA_BB
29 - SN_WAICE
30 - SNSH
31 - SH
32 - FLAME
33 - UN

Appendix F – Eastern planes – Class (category) distribution (from top to bottom: winter, spring, summer, autumn)

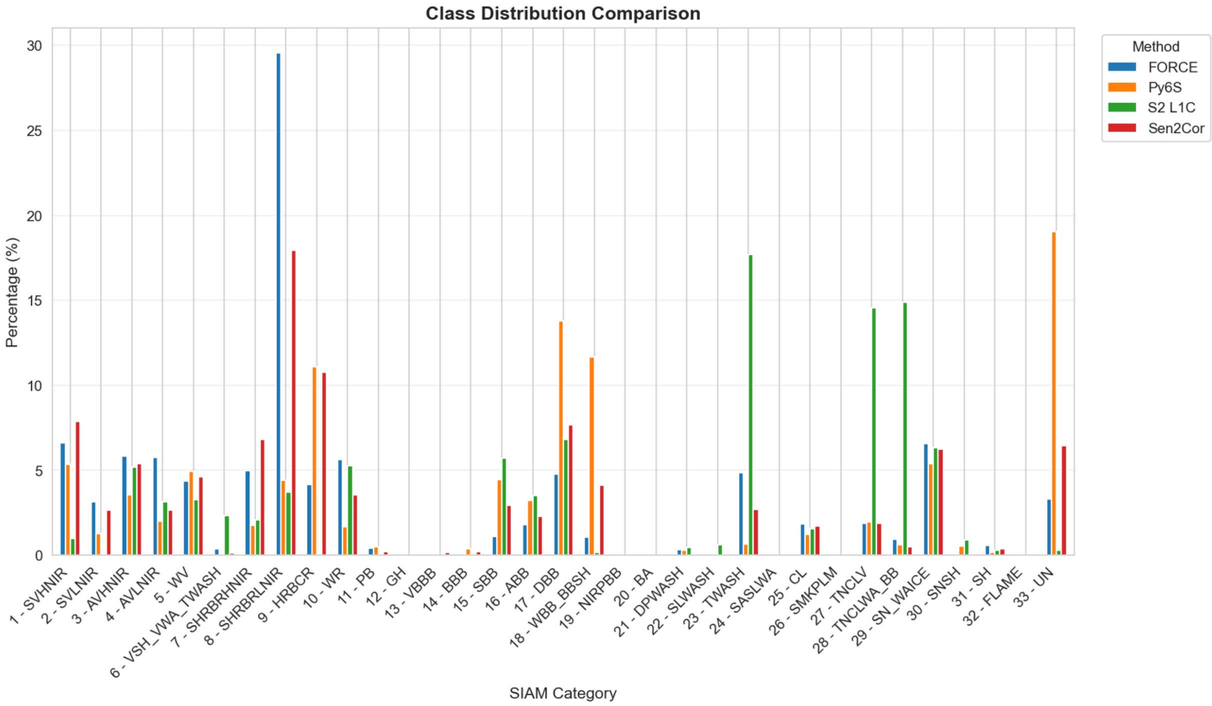

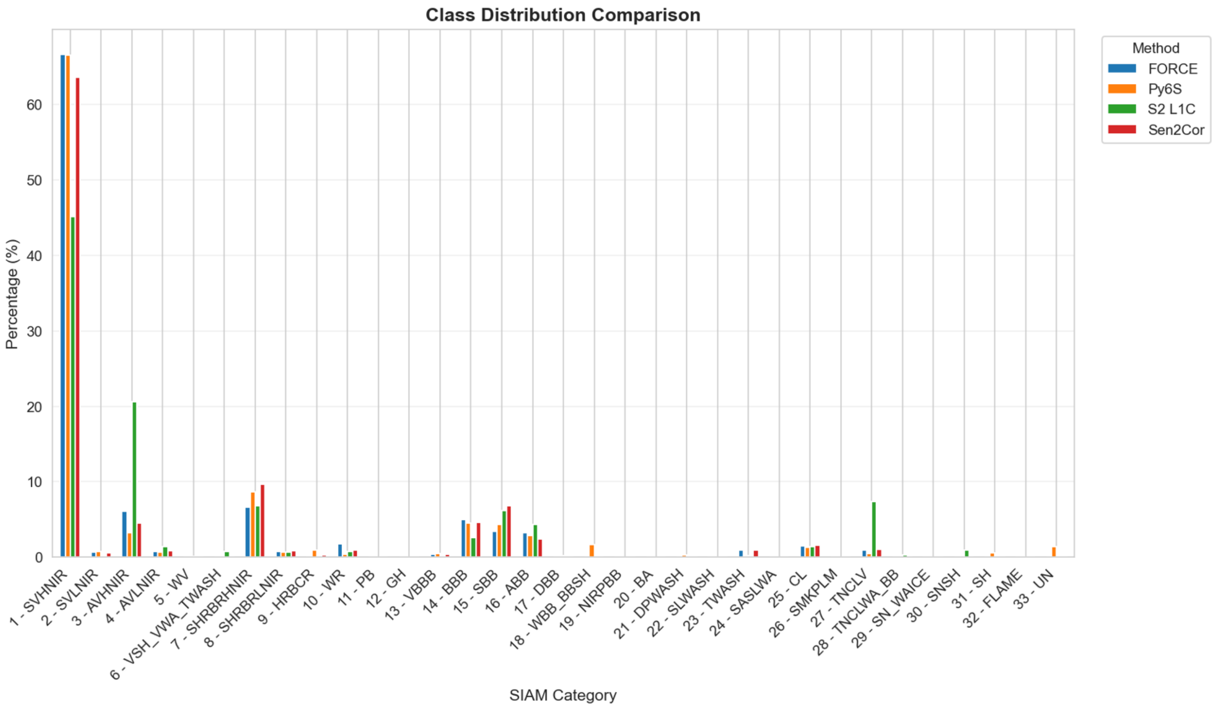

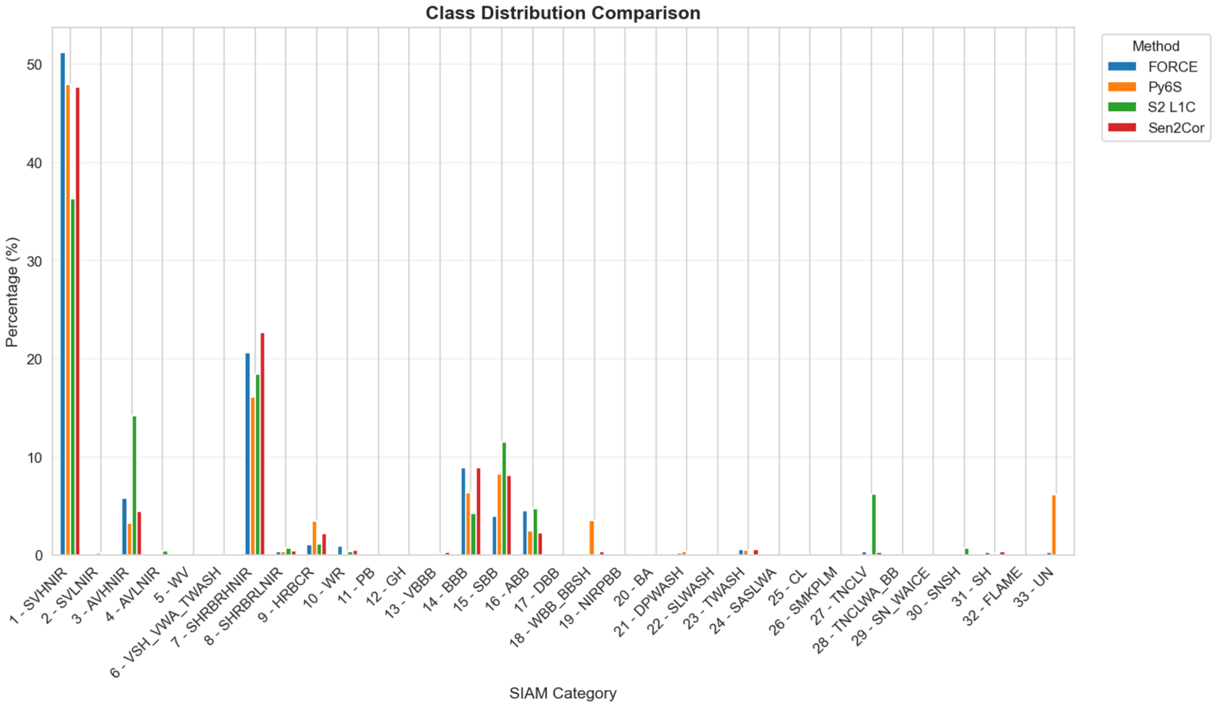

Class Distribution Comparison
Method
FORCE
Py6S
S2 L1C
Sen2Cor
Percentage (%)
SIAM Category
1 - SVHNIR
2 - SVLNIR
3 - AVHNIR
4 - AVLNIR
5 - WV
6 - VSH_VWA_TWASH
7 - SHRBRHNIR
8 - SHRBRLNIR
9 - HRBCR
10 - WR
11 - PB
12 - GH
13 - VBBB
14 - BBB
15 - SBB
16 - ABB
17 - DBB
18 - WBB_BBSH
19 - NIRPBB
20 - BA
21 - DPWASH
22 - SLWASH
23 - TWASH
24 - SASLWA
25 - CL
26 - SMKPLM
27 - TNCLV
28 - TNCLWA_BB
29 - SN_WAICE
30 - SNSH
31 - SH
32 - FLAME
33 - UN

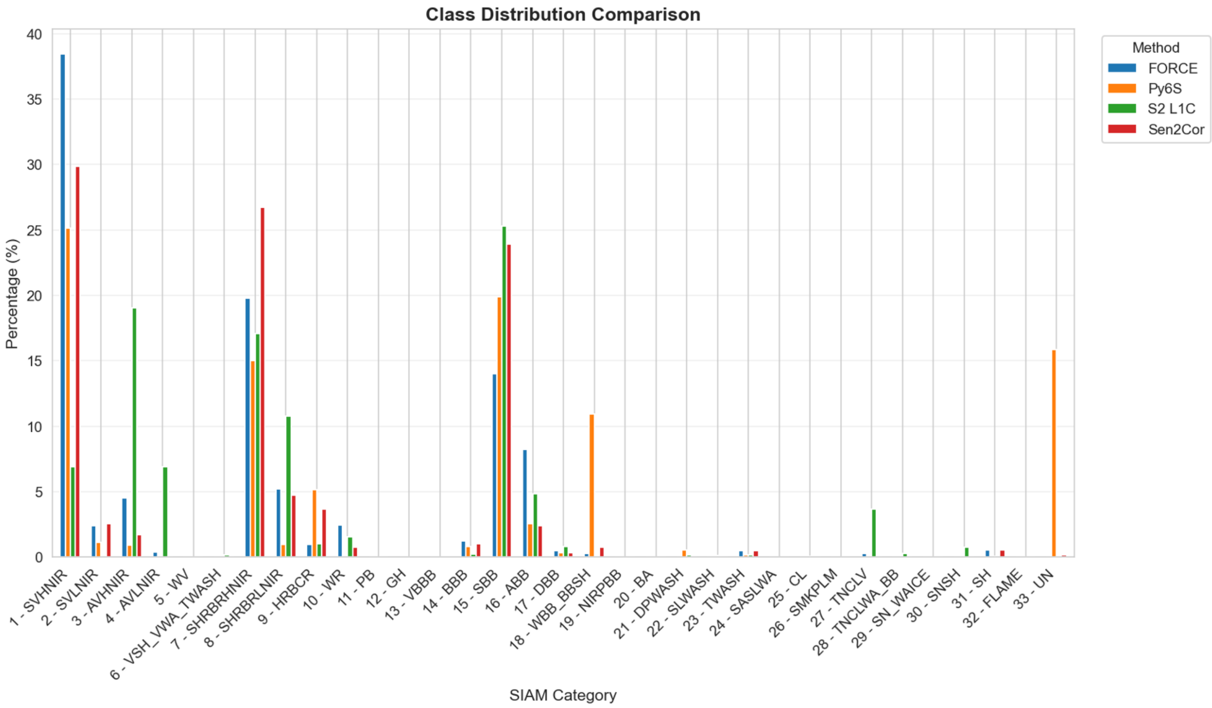

Class Distribution Comparison
Method
FORCE
Py6S
S2 L1C
Sen2Cor
Percentage (%)
SIAM Category
1 - SVHNIR
2 - SVLNIR
3 - AVHNIR
4 - AVLNIR
5 - WV
6 - VSH_VWA_TWASH
7 - SHRBRHNIR
8 - SHRBRLNIR
9 - HRBCR
10 - WR
11 - PB
12 - GH
13 - VBBB
14 - BBB
15 - SBB
16 - ABB
17 - DBB
18 - WBB_BBSH
19 - NIRPBB
20 - BA
21 - DPWASH
22 - SLWASH
23 - TWASH
24 - SASLWA
25 - CL
26 - SMKPLM
27 - TNCLV
28 - TNCLWA_BB
29 - SN_WAICE
30 - SNSH
31 - SH
32 - FLAME
33 - UN

Appendix G – Alpine valleys – Pairwise agreement BOA-BOA (from top to bottom: winter, spring, summer, autumn)

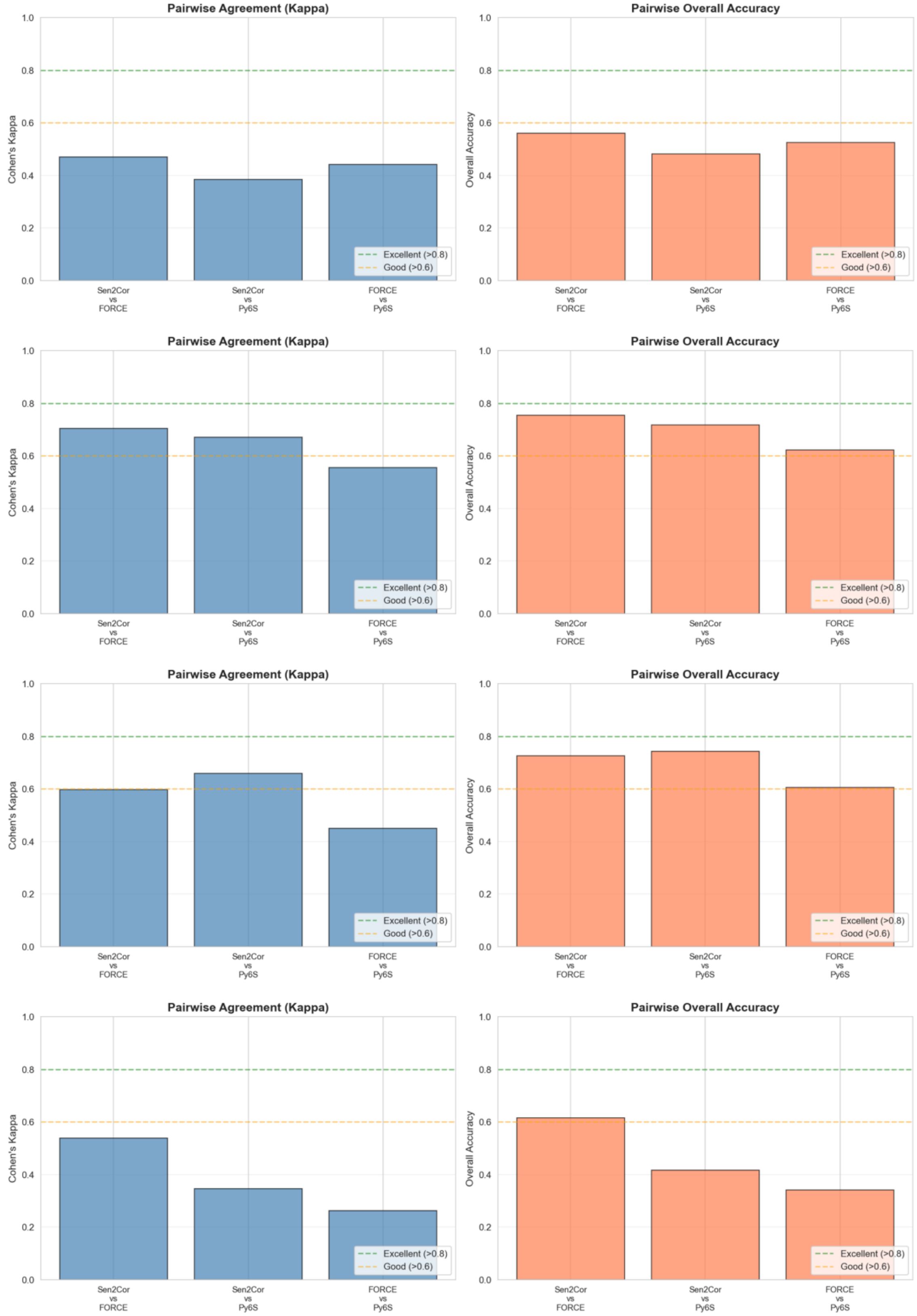

Appendix H – High Alps – Pairwise agreement BOA-BOA (from top to bottom: winter, spring, summer, autumn)

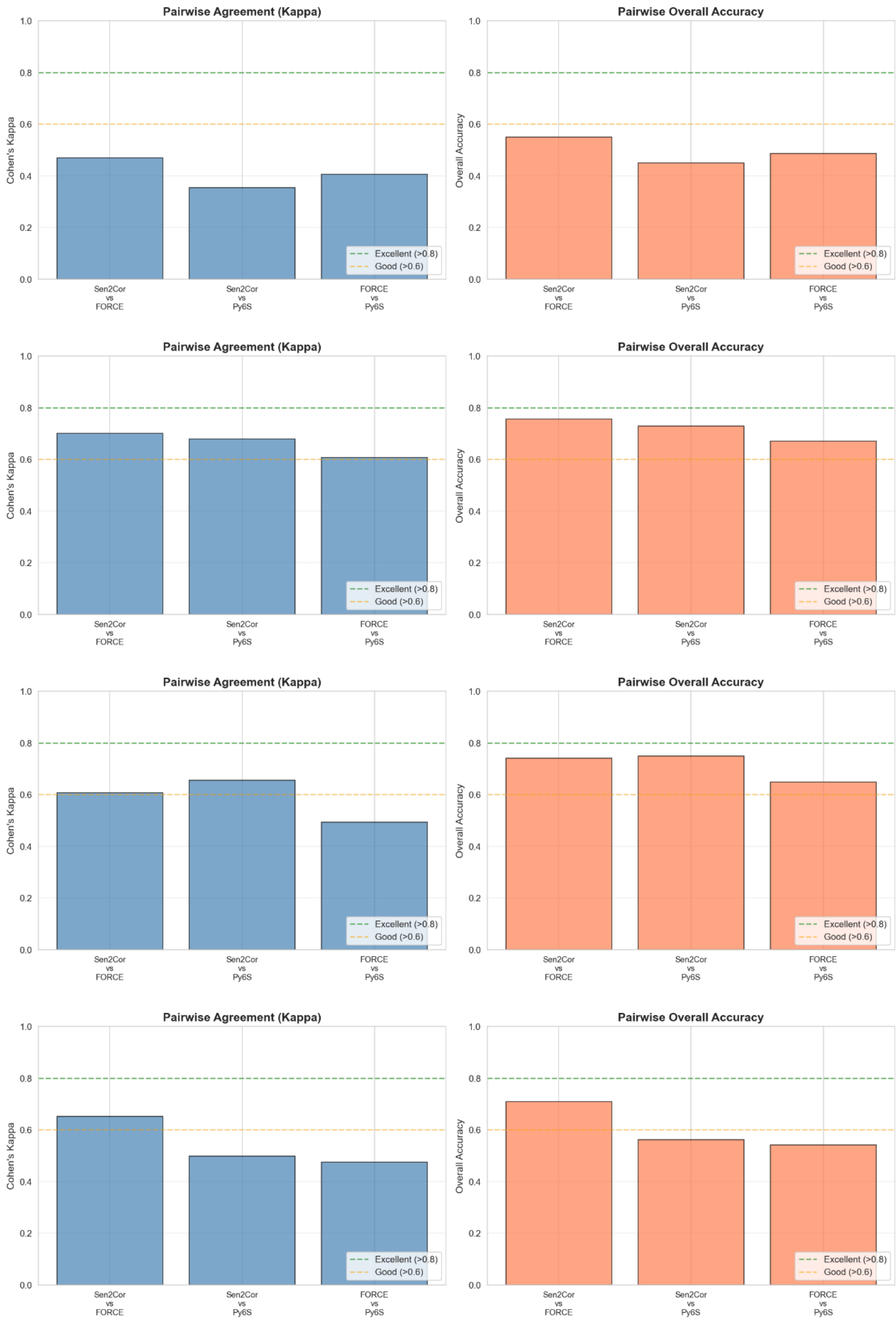

Appendix I – Pre-Alps – Pairwise agreement BOA-BOA (from top to bottom: winter, spring, summer, autumn)

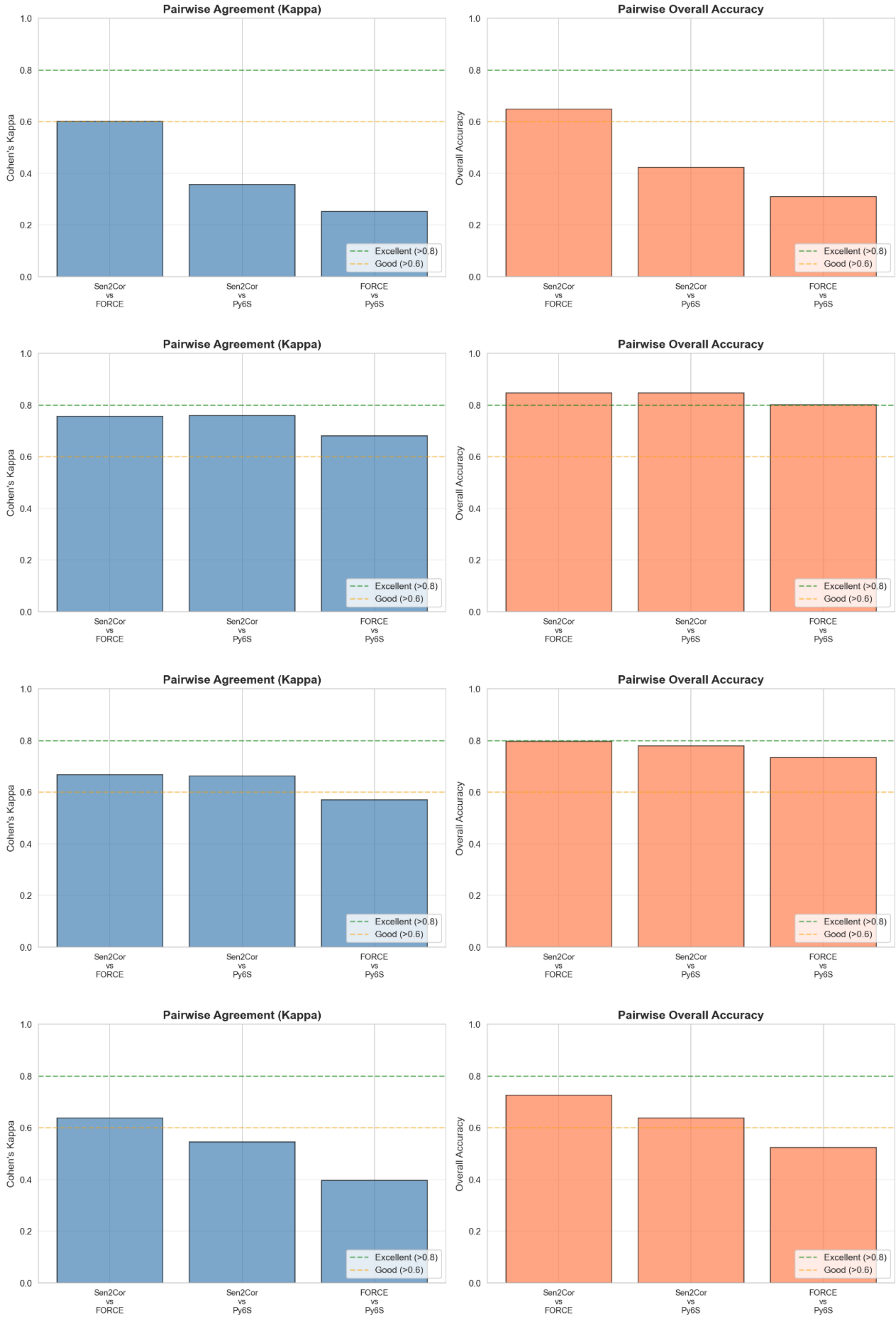

Appendix J – Eastern planes – Pairwise agreement BOA-BOA (from top to bottom: winter, spring, summer, autumn)

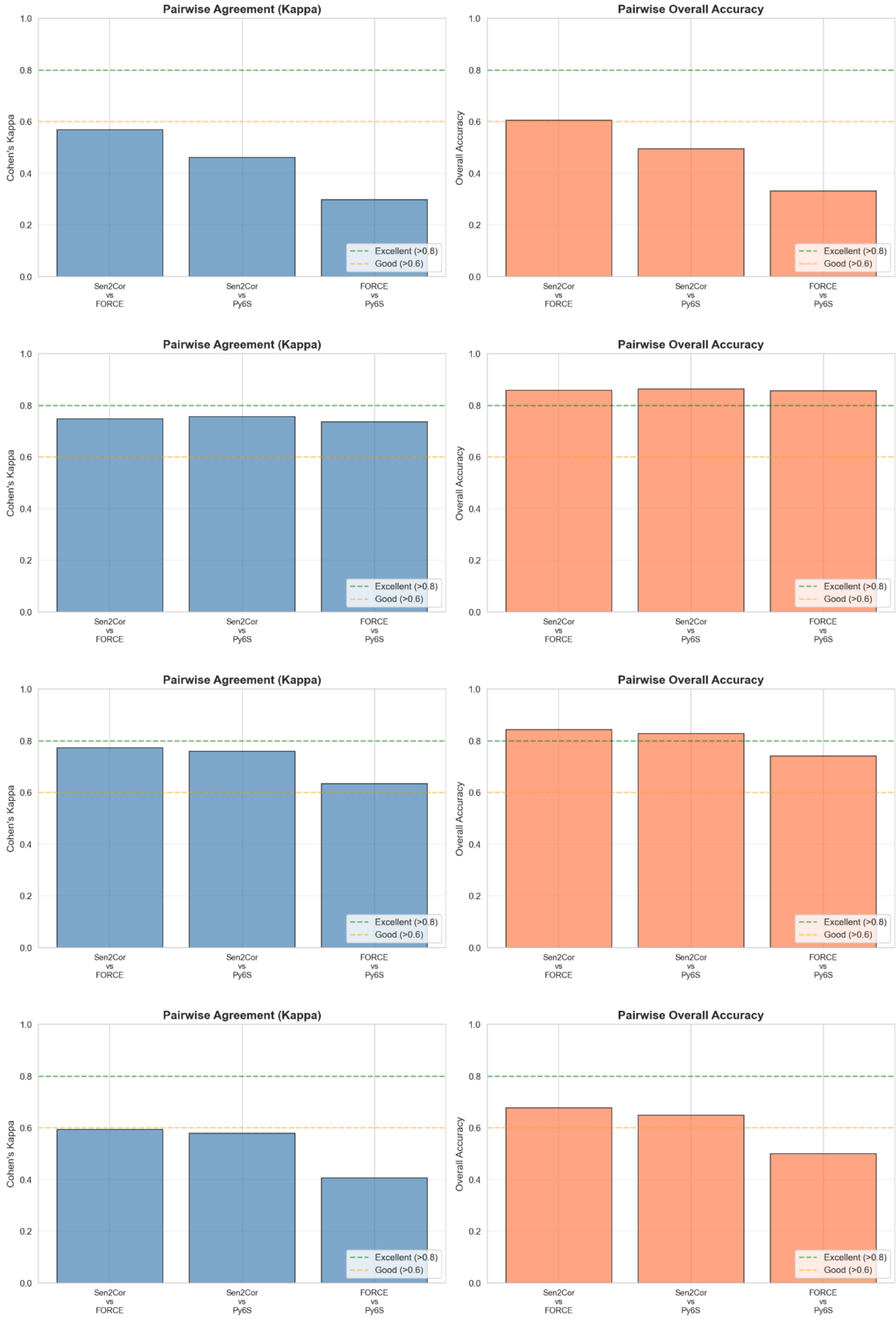

Appendix K – Category stability across seasons

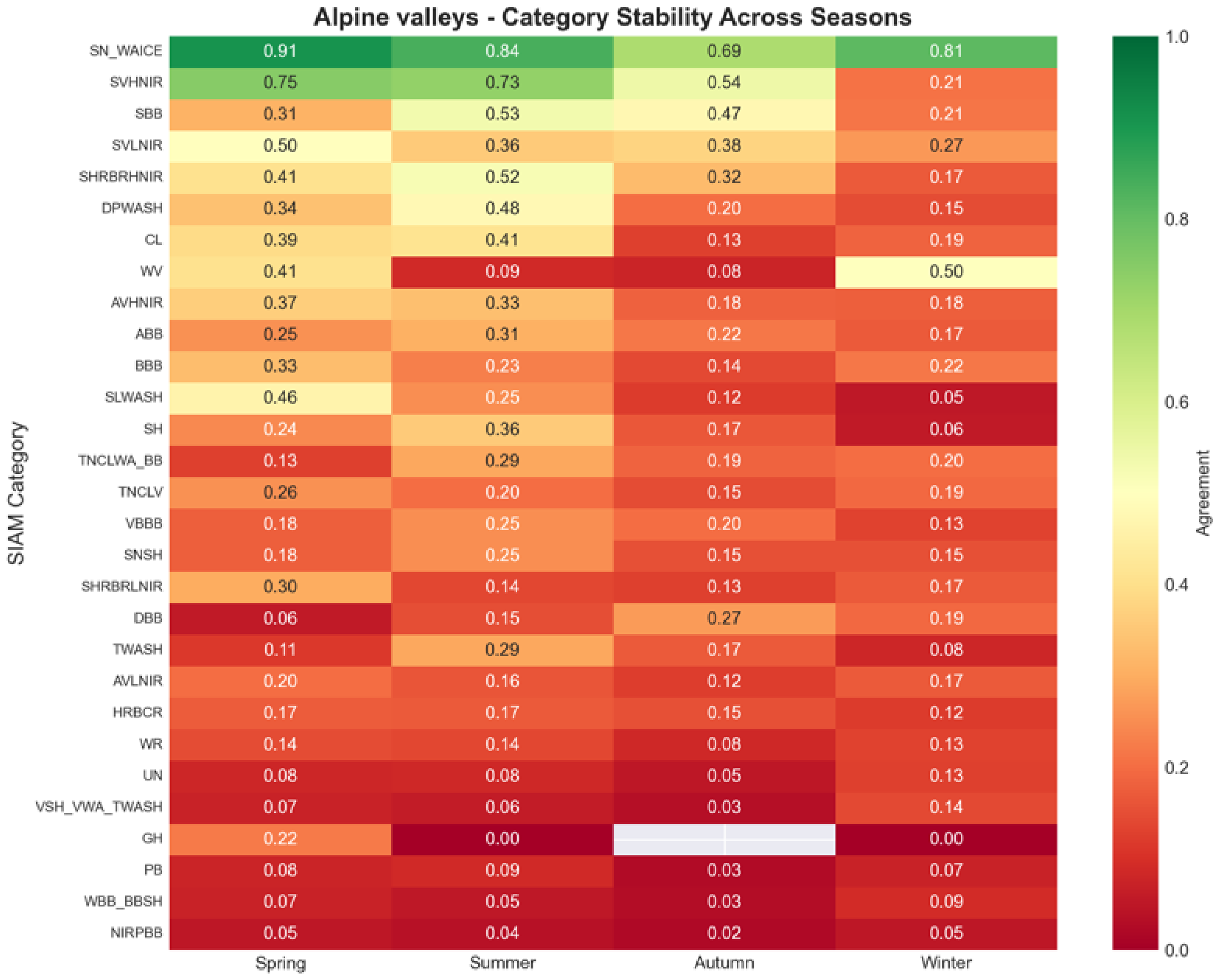

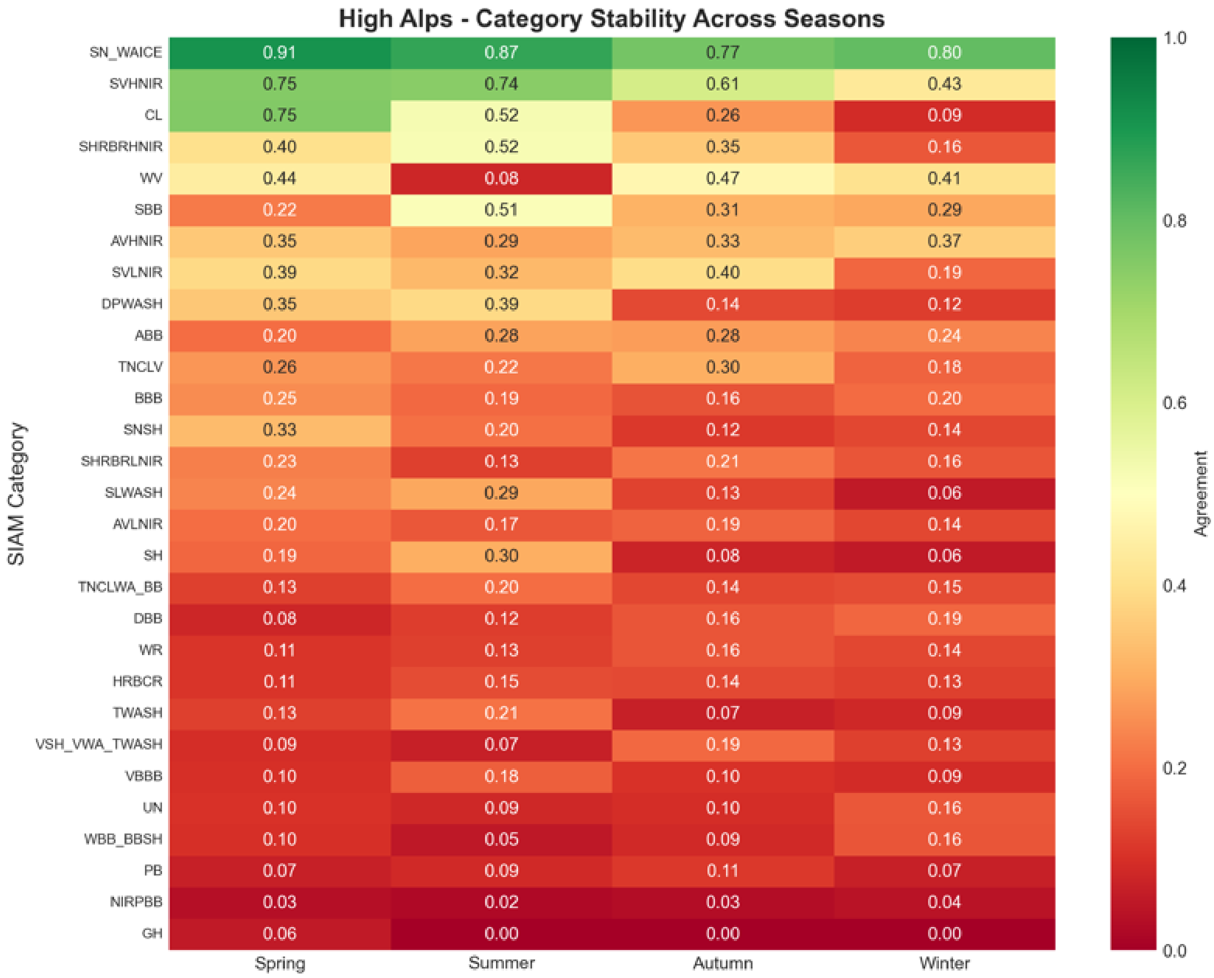
High Alps - Category Stability Across Seasons
SIAM Category
Agreement
SN_WAICE
SVHNIR
CL
SHRBRHNIR
WV
SBB
AVHNIR
SVLNIR
DPWASH
ABB
TNCLV
BBB
SNSH
SHRBRLNIR
SLWASH
AVLNIR
SH
TNCLWA_BB
DBB
WR
HRBCR
TWASH
VSH_VWA_TWASH
VBBB
UN
WBB_BBSH
PB
NIRPBB
GH
Spring
Summer
Autumn
Winter
0.91 0.87 0.77 0.80
0.75 0.74 0.61 0.43
0.75 0.52 0.26 0.09
0.40 0.52 0.35 0.16
0.44 0.08 0.47 0.41
0.22 0.51 0.31 0.29
0.35 0.29 0.33 0.37
0.39 0.32 0.40 0.19
0.35 0.39 0.14 0.12
0.20 0.28 0.28 0.24
0.26 0.22 0.30 0.18
0.25 0.19 0.16 0.20
0.33 0.20 0.12 0.14
0.23 0.13 0.21 0.16
0.24 0.29 0.13 0.06
0.20 0.17 0.19 0.14
0.19 0.30 0.08 0.06
0.13 0.20 0.14 0.15
0.08 0.12 0.16 0.19
0.11 0.13 0.16 0.14
0.11 0.15 0.14 0.13
0.13 0.21 0.07 0.09
0.09 0.07 0.19 0.13
0.10 0.18 0.10 0.09
0.10 0.09 0.10 0.16
0.10 0.05 0.09 0.16
0.07 0.09 0.11 0.07
0.03 0.02 0.03 0.04
0.06 0.00 0.00 0.00
1.0
0.8
0.6
0.4
0.2
0.0

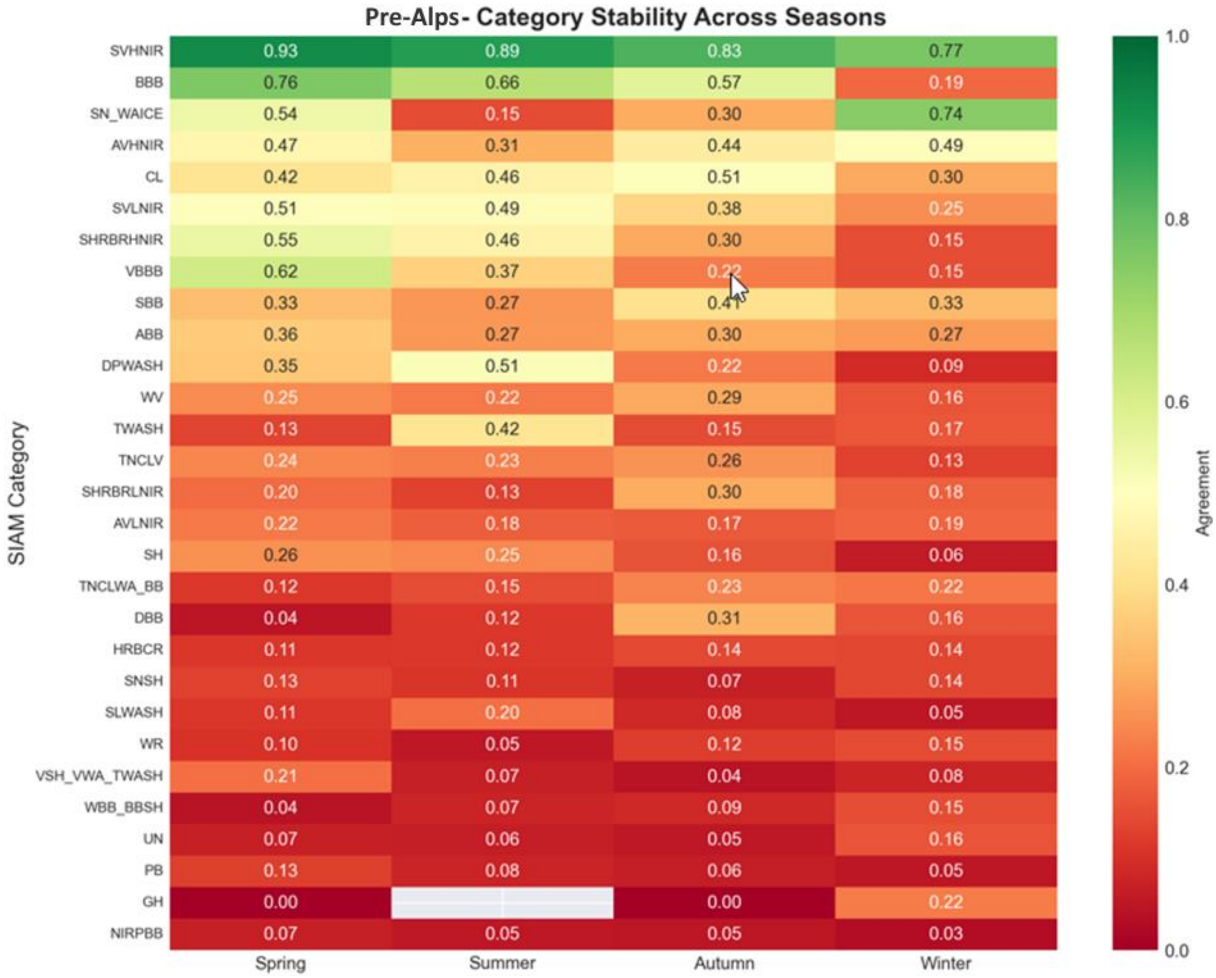
Pre-Alps- Category Stability Across Seasons
SVHNIR
BBB
SN_WAICE
AVHNIR
CL
SVLNIR
SHRBRHNIR
VBBB
SBB
ABB
DPWASH
WV
TWASH
TNCLV
SHRBRLNIR
AVLNIR
SH
TNCLWA_BB
DBB
HRBCR
SNSH
SLWASH
WR
VSH_VWA_TWASH
WBB_BBSH
UN
PB
GH
NIRPBB
SIAM Category
Spring
Summer
Autumn
Winter
Agreement

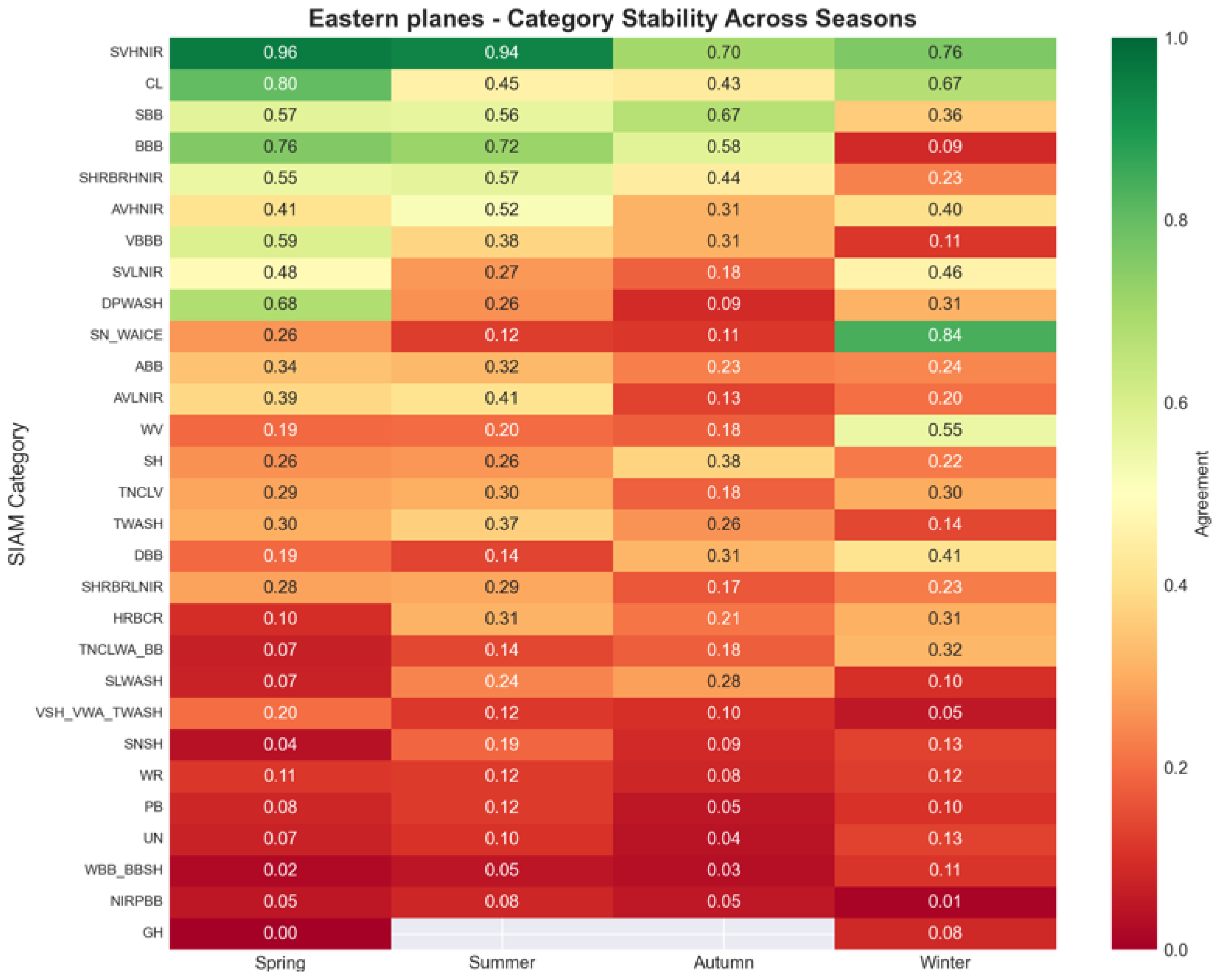
Eastern planes - Category Stability Across Seasons
SIAM Category
Agreement
Spring
Summer
Autumn
Winter
SVHNIR
CL
SBB
BBB
SHRBRHNIR
AVHNIR
VBBB
SVLNIR
DPWASH
SN_WAICE
ABB
AVLNIR
WV
SH
TNCLV
TWASH
DBB
SHRBRLNIR
HRBCR
TNCLWA_BB
SLWASH
VSH_VWA_TWASH
SNSH
WR
PB
UN
WBB_BBSH
NIRPBB
GH

Appendix L – Alpine valleys – change magnitude (from top to bottom: winter, spring, summer, autumn)

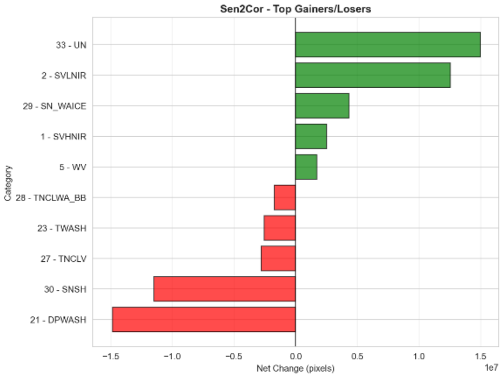

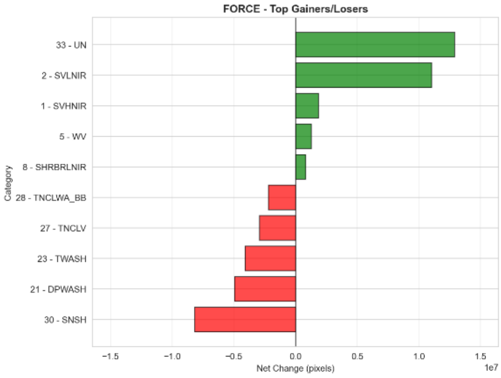

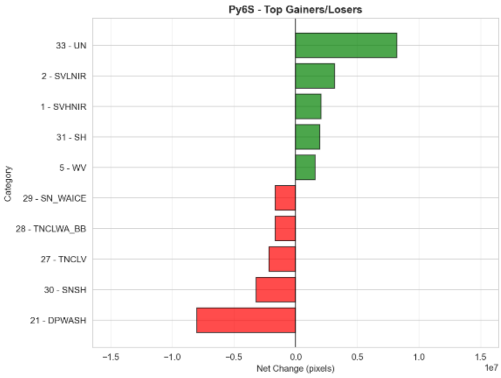

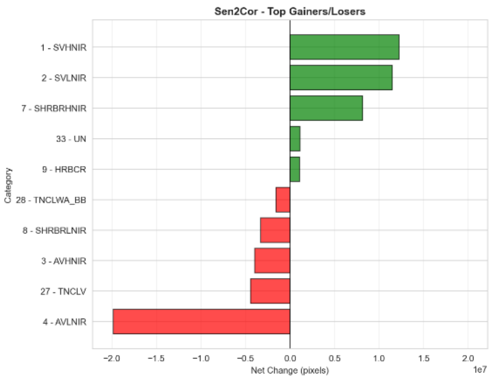

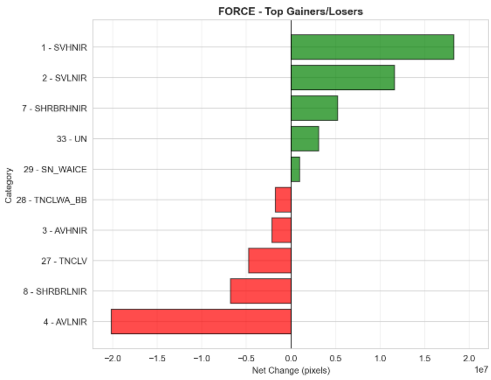

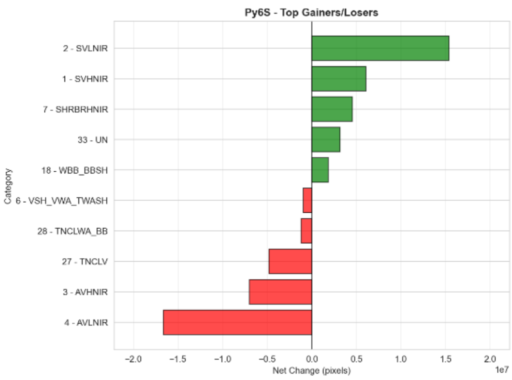

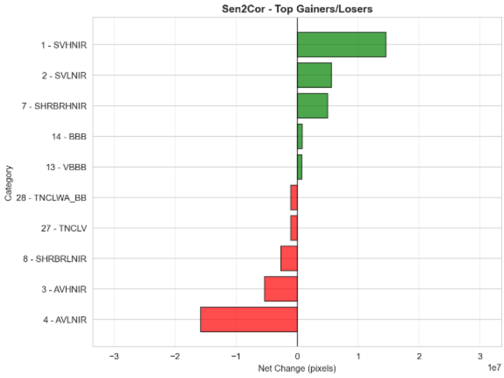
Sen2Cor - Top Gainers/Losers
1 - SVHNIR
2 - SVLNIR
7 - SHRBRHNIR
14 - BBB
13 - VBBB
28 - TNCLWA_BB
27 - TNCLV
8 - SHRBRLNIR
3 - AVHNIR
4 - AVLNIR
Category
−3 −2 −1 0 1 2 3
Net Change (pixels)
1e7

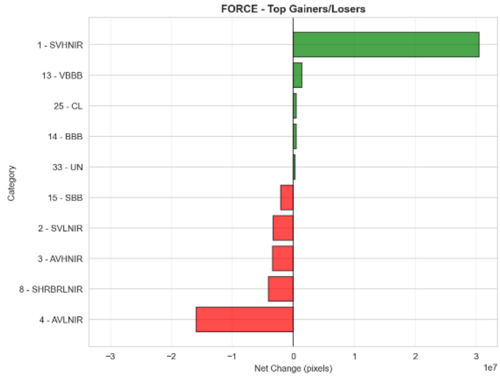
FORCE - Top Gainers/Losers
1 - SVHNIR
13 - VBBB
25 - CL
14 - BBB
33 - UN
15 - SBB
2 - SVLNIR
3 - AVHNIR
8 - SHRBRLNIR
4 - AVLNIR
Category
−3 −2 −1 0 1 2 3
Net Change (pixels)
1e7

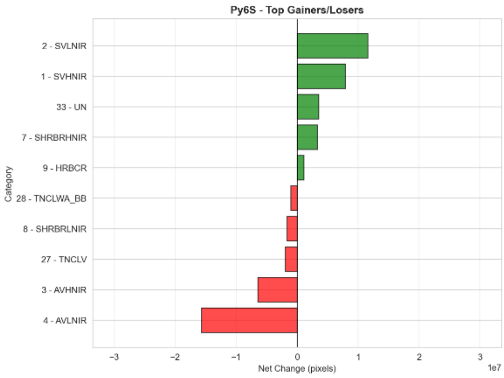
Py6S - Top Gainers/Losers
2 - SVLNIR
1 - SVHNIR
33 - UN
7 - SHRBRHNIR
9 - HRBCR
28 - TNCLWA_BB
8 - SHRBRLNIR
27 - TNCLV
3 - AVHNIR
4 - AVLNIR
Category
−3 −2 −1 0 1 2 3
Net Change (pixels)
1e7

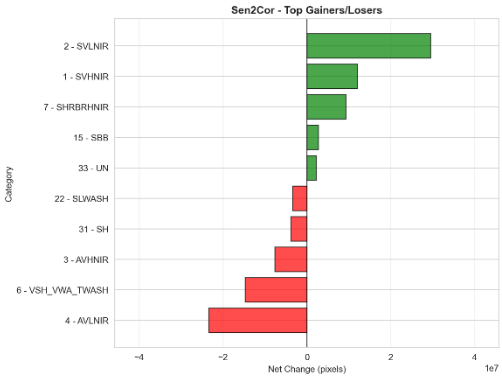
Sen2Cor - Top Gainers/Losers
2 - SVLNIR
1 - SVHNIR
7 - SHRBRHNIR
15 - SBB
33 - UN
22 - SLWASH
31 - SH
3 - AVHNIR
6 - VSH_VWA_TWASH
4 - AVLNIR
Category
−4 −2 0 2 4
Net Change (pixels)
1e7

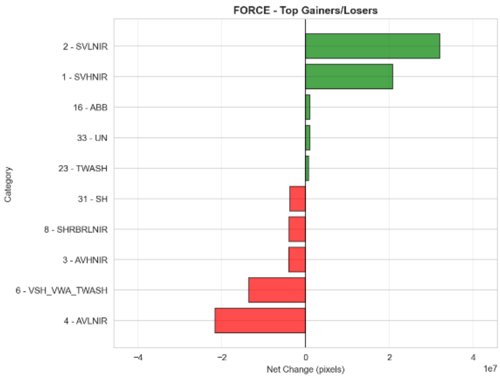
FORCE - Top Gainers/Losers
2 - SVLNIR
1 - SVHNIR
16 - ABB
33 - UN
23 - TWASH
31 - SH
8 - SHRBRLNIR
3 - AVHNIR
6 - VSH_VWA_TWASH
4 - AVLNIR
Category
−4 −2 0 2 4
Net Change (pixels)
1e7

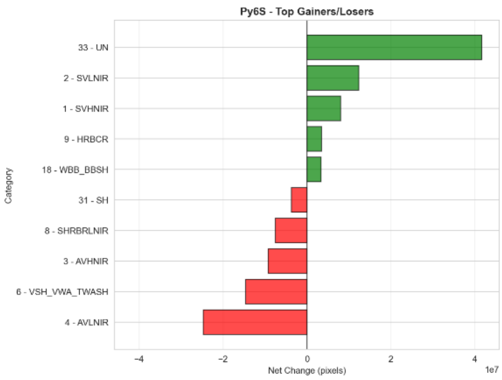
Py6S - Top Gainers/Losers
33 - UN
2 - SVLNIR
1 - SVHNIR
9 - HRBCR
18 - WBB_BBSH
31 - SH
8 - SHRBRLNIR
3 - AVHNIR
6 - VSH_VWA_TWASH
4 - AVLNIR
Category
−4 −2 0 2 4
Net Change (pixels)
1e7

Appendix M – High Alps – change magnitude (from top to bottom: winter, spring, summer, autumn)

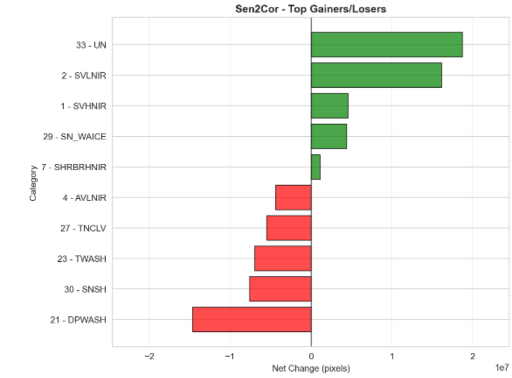

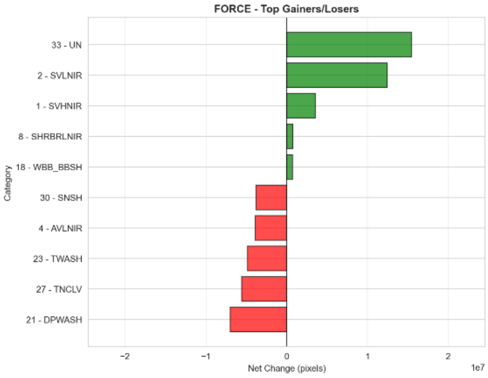

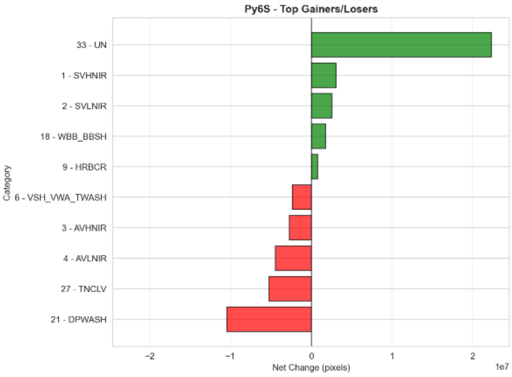

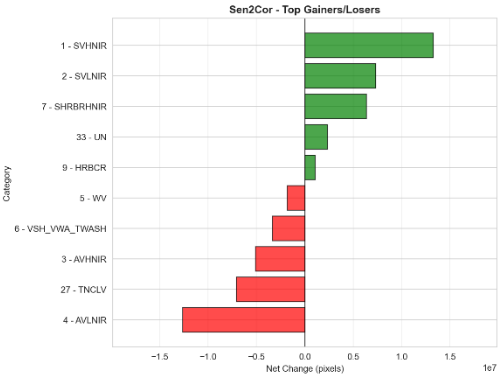

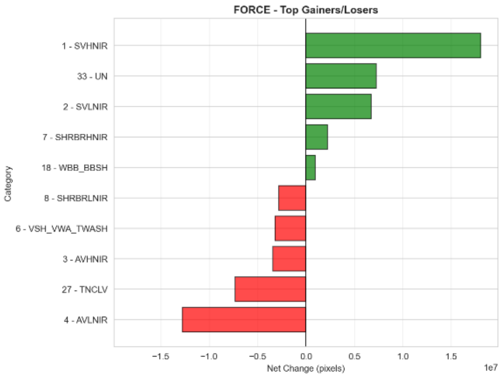

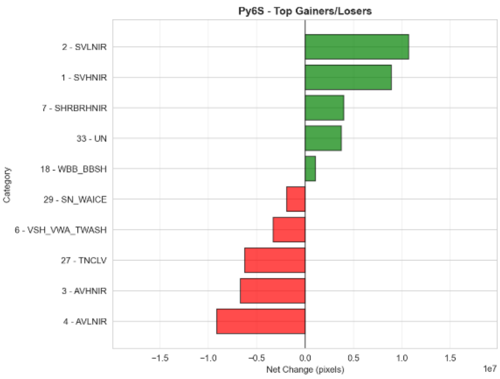

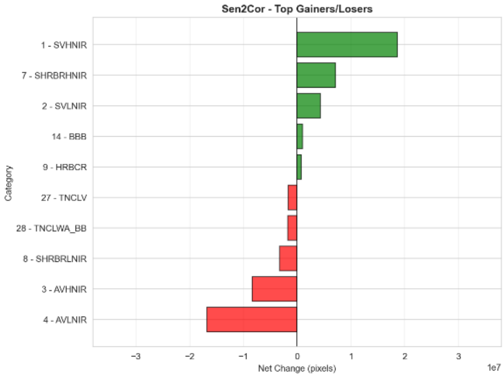
Sen2Cor - Top Gainers/Losers
1 - SVHNIR
7 - SHRBRHNIR
2 - SVLNIR
14 - BBB
9 - HRBCR
27 - TNCLV
28 - TNCLWA_BB
8 - SHRBRLNIR
3 - AVHNIR
4 - AVLNIR
Category
Net Change (pixels)
1e7

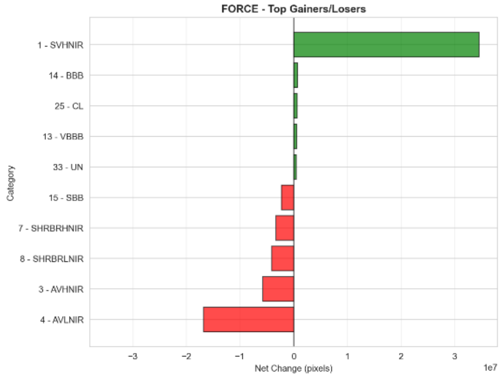
FORCE - Top Gainers/Losers
1 - SVHNIR
14 - BBB
25 - CL
13 - VBBB
33 - UN
15 - SBB
7 - SHRBRHNIR
8 - SHRBRLNIR
3 - AVHNIR
4 - AVLNIR
Category
Net Change (pixels)
1e7

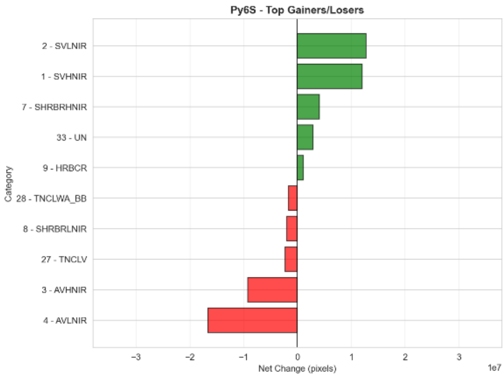
Py6S - Top Gainers/Losers
2 - SVLNIR
1 - SVHNIR
7 - SHRBRHNIR
33 - UN
9 - HRBCR
28 - TNCLWA_BB
8 - SHRBRLNIR
27 - TNCLV
3 - AVHNIR
4 - AVLNIR
Category
Net Change (pixels)
1e7

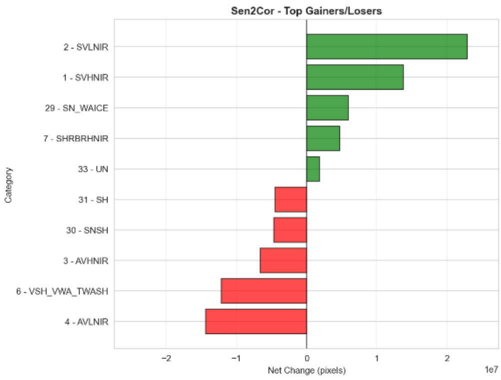
Sen2Cor - Top Gainers/Losers
2 - SVLNIR
1 - SVHNIR
29 - SN_WAICE
7 - SHRBRHNIR
33 - UN
31 - SH
30 - SNSH
3 - AVHNIR
6 - VSH_VWA_TWASH
4 - AVLNIR
Category
Net Change (pixels)
1e7

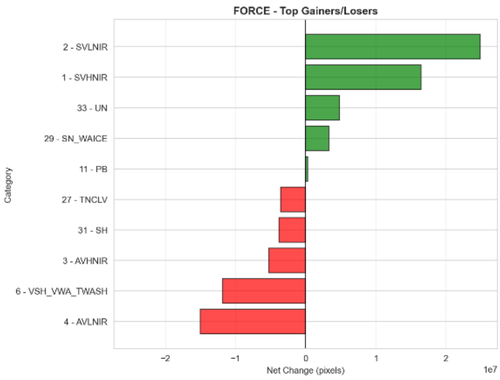
FORCE - Top Gainers/Losers
2 - SVLNIR
1 - SVHNIR
33 - UN
29 - SN_WAICE
11 - PB
27 - TNCLV
31 - SH
3 - AVHNIR
6 - VSH_VWA_TWASH
4 - AVLNIR
Category
Net Change (pixels)
1e7

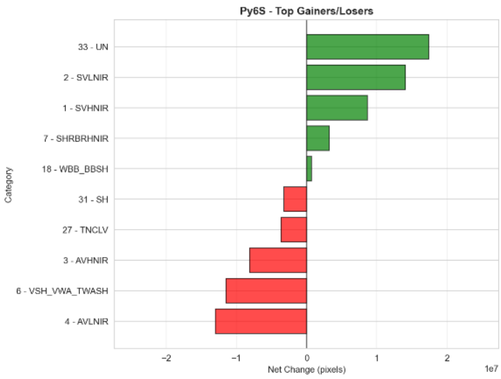
Py6S - Top Gainers/Losers
33 - UN
2 - SVLNIR
1 - SVHNIR
7 - SHRBRHNIR
18 - WBB_BBSH
31 - SH
27 - TNCLV
3 - AVHNIR
6 - VSH_VWA_TWASH
4 - AVLNIR
Category
Net Change (pixels)
1e7

Appendix N – Pre-Alps – change magnitude (from top to bottom: winter, spring, summer, autumn)

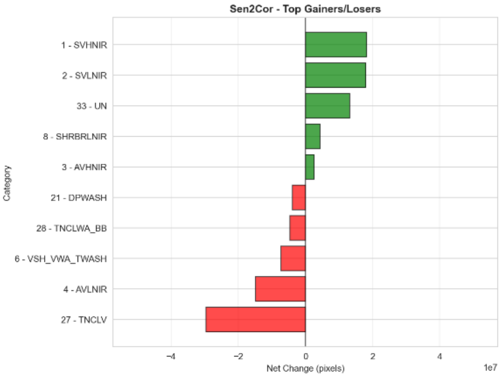

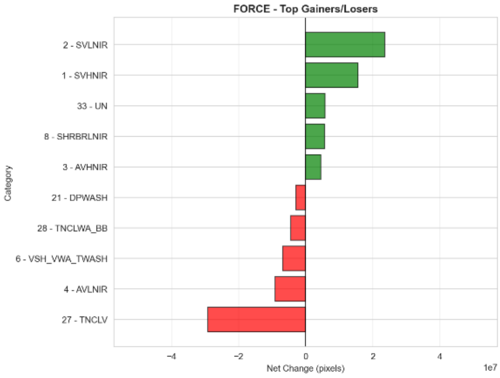

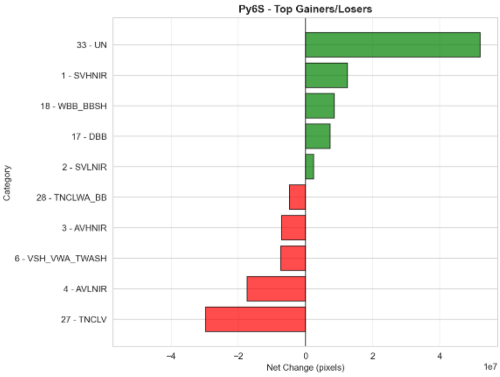

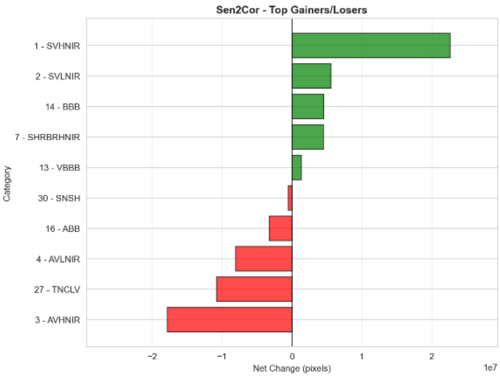

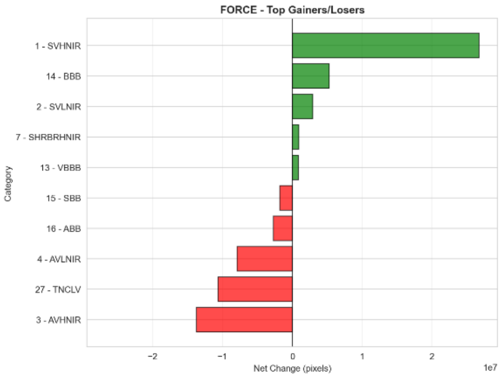

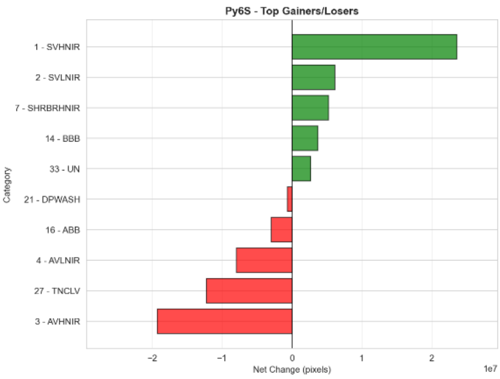

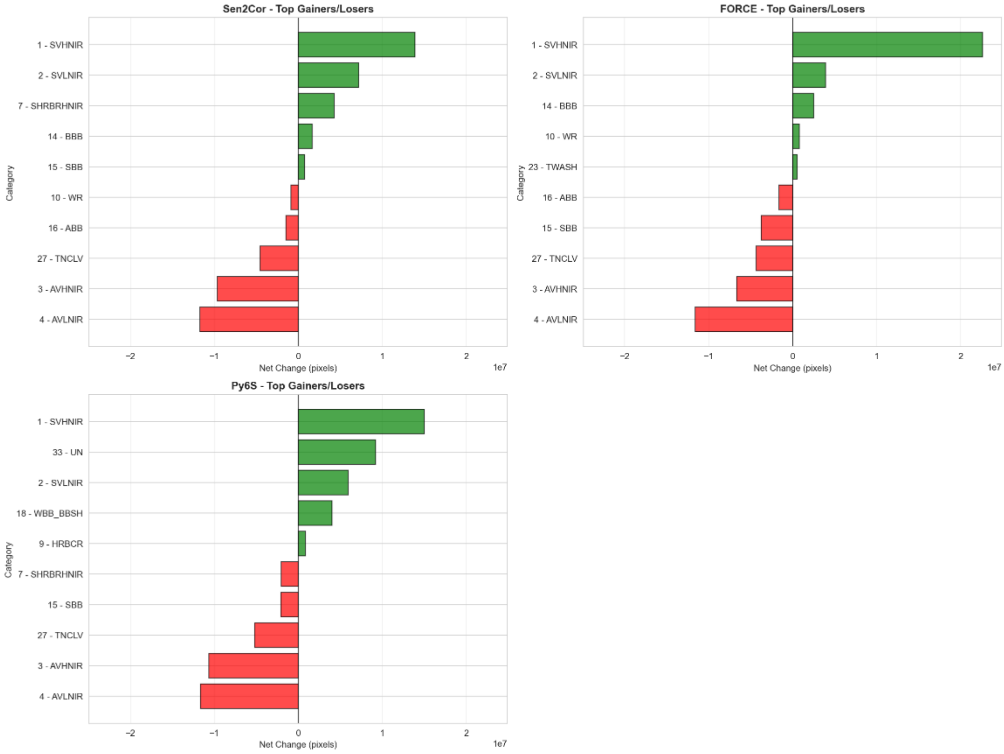
Sen2Cor - Top Gainers/Losers
1 - SVHNIR
2 - SVLNIR
7 - SHRBRHNIR
14 - BBB
15 - SBB
10 - WR
16 - ABB
27 - TNCLV
3 - AVHNIR
4 - AVLNIR
Category
Net Change (pixels)
1e7
FORCE - Top Gainers/Losers
1 - SVHNIR
2 - SVLNIR
14 - BBB
10 - WR
23 - TWASH
16 - ABB
15 - SBB
27 - TNCLV
3 - AVHNIR
4 - AVLNIR
Category
Net Change (pixels)
1e7
Py6S - Top Gainers/Losers
1 - SVHNIR
33 - UN
2 - SVLNIR
18 - WBB_BBSH
9 - HRBCR
7 - SHRBRHNIR
15 - SBB
27 - TNCLV
3 - AVHNIR
4 - AVLNIR
Category
Net Change (pixels)
1e7

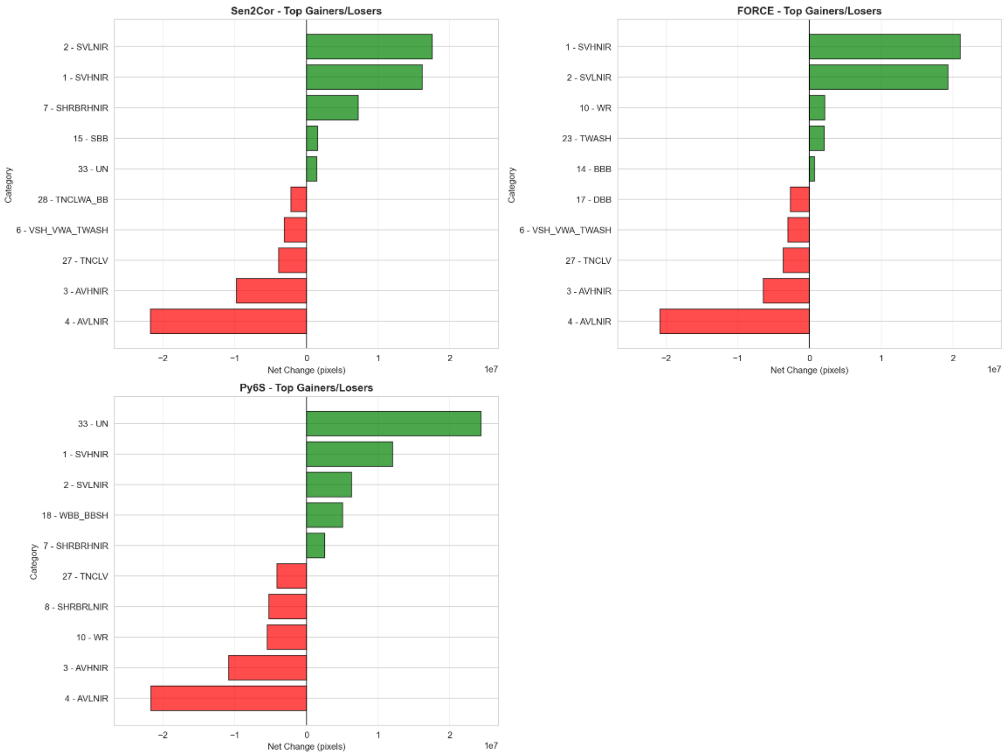
Sen2Cor - Top Gainers/Losers
2 - SVLNIR
1 - SVHNIR
7 - SHRBRHNIR
15 - SBB
33 - UN
28 - TNCLWA_BB
6 - VSH_VWA_TWASH
27 - TNCLV
3 - AVHNIR
4 - AVLNIR
Category
Net Change (pixels)
1e7
FORCE - Top Gainers/Losers
1 - SVHNIR
2 - SVLNIR
10 - WR
23 - TWASH
14 - BBB
17 - DBB
6 - VSH_VWA_TWASH
27 - TNCLV
3 - AVHNIR
4 - AVLNIR
Category
Net Change (pixels)
1e7
Py6S - Top Gainers/Losers
33 - UN
1 - SVHNIR
2 - SVLNIR
18 - WBB_BBSH
7 - SHRBRHNIR
27 - TNCLV
8 - SHRBRLNIR
10 - WR
3 - AVHNIR
4 - AVLNIR
Category
Net Change (pixels)
1e7

Appendix O – Eastern planes – change magnitude (from top to bottom: winter, spring, summer, autumn)

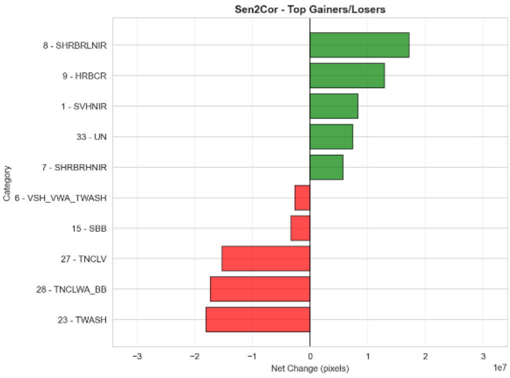

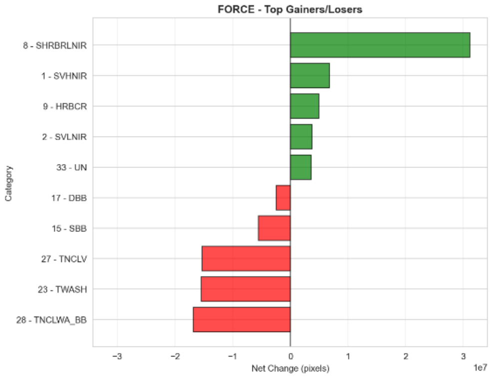

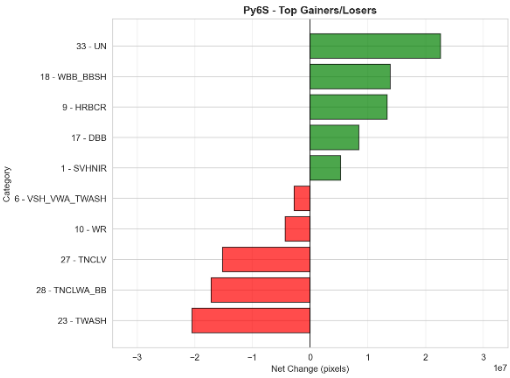

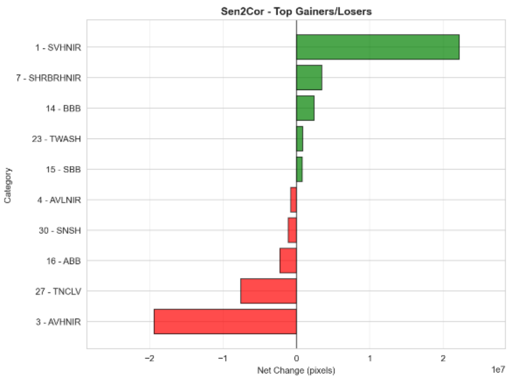

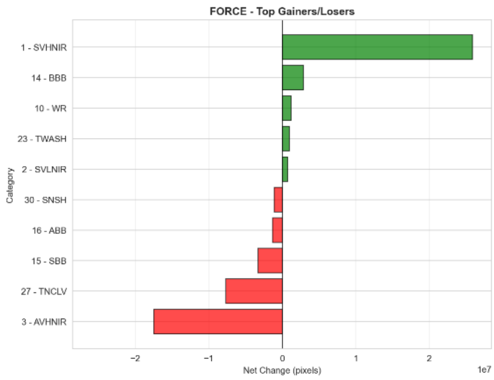

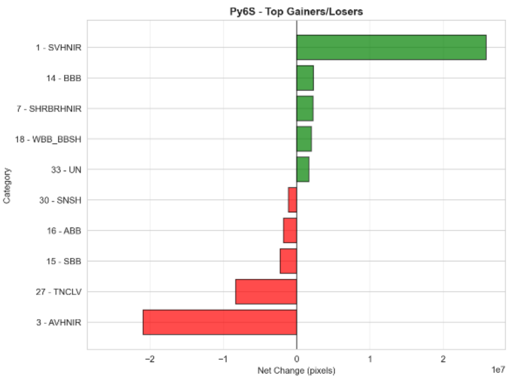

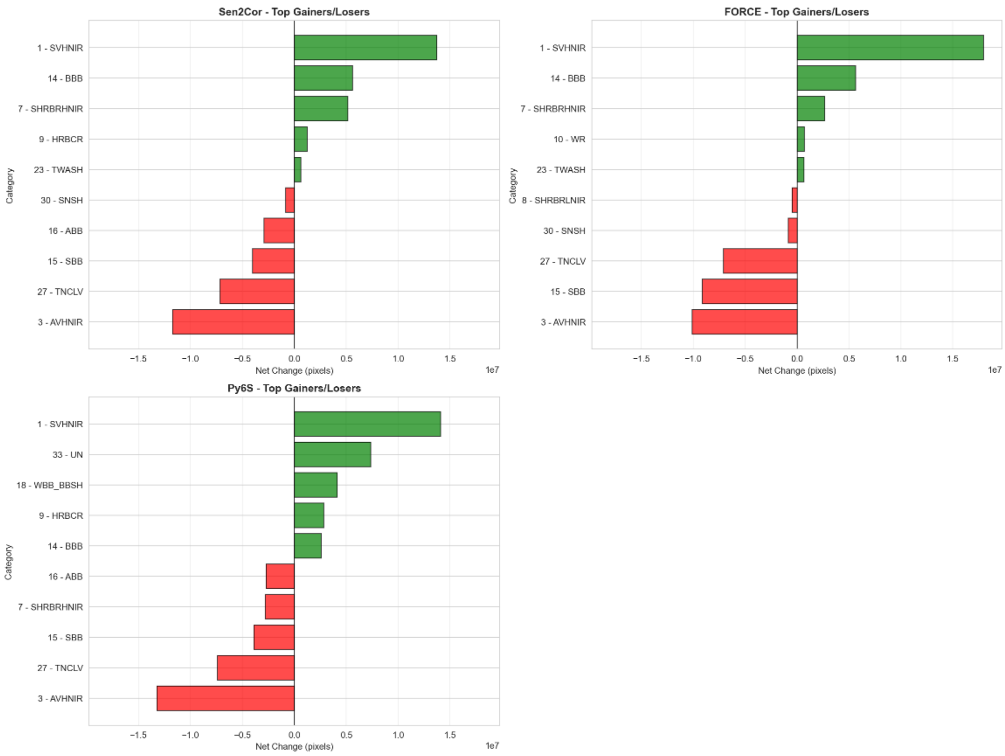
Sen2Cor - Top Gainers/Losers
1 - SVHNIR
14 - BBB
7 - SHRBRHNIR
9 - HRBCR
23 - TWASH
30 - SNSH
16 - ABB
15 - SBB
27 - TNCLV
3 - AVHNIR
Category
Net Change (pixels)
1e7
FORCE - Top Gainers/Losers
1 - SVHNIR
14 - BBB
7 - SHRBRHNIR
10 - WR
23 - TWASH
8 - SHRBRLNIR
30 - SNSH
27 - TNCLV
15 - SBB
3 - AVHNIR
Category
Net Change (pixels)
1e7
Py6S - Top Gainers/Losers
1 - SVHNIR
33 - UN
18 - WBB_BBSH
9 - HRBCR
14 - BBB
16 - ABB
7 - SHRBRHNIR
15 - SBB
27 - TNCLV
3 - AVHNIR
Category
Net Change (pixels)
1e7

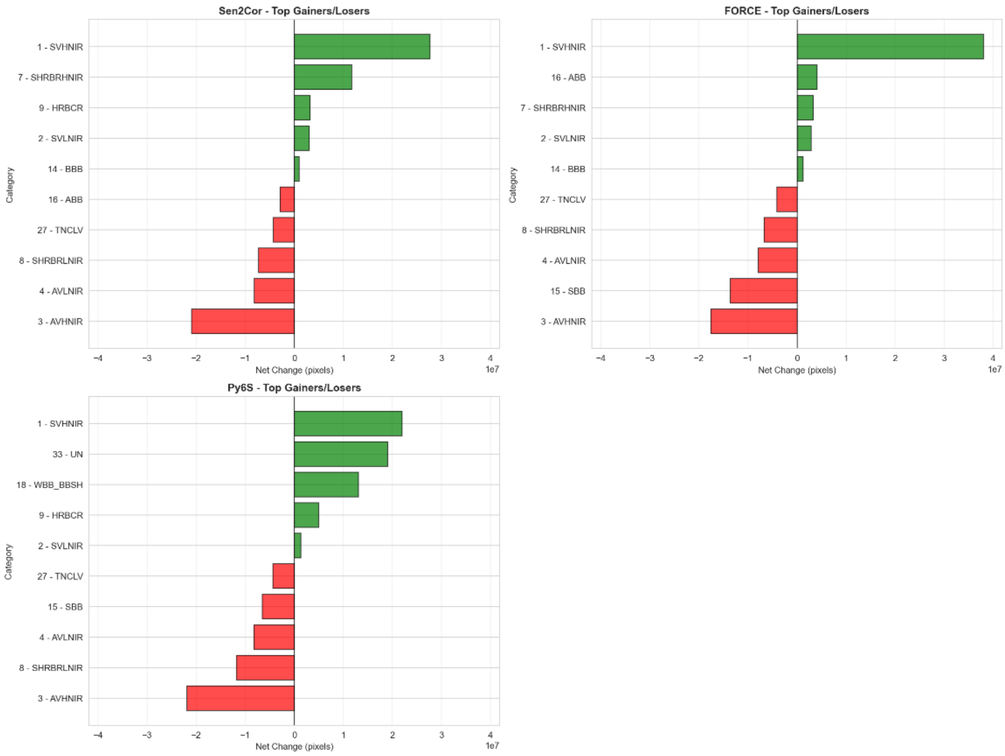
Sen2Cor - Top Gainers/Losers
1 - SVHNIR
7 - SHRBRHNIR
9 - HRBCR
2 - SVLNIR
14 - BBB
16 - ABB
27 - TNCLV
8 - SHRBRLNIR
4 - AVLNIR
3 - AVHNIR
Category
Net Change (pixels)
1e7
FORCE - Top Gainers/Losers
1 - SVHNIR
16 - ABB
7 - SHRBRHNIR
2 - SVLNIR
14 - BBB
27 - TNCLV
8 - SHRBRLNIR
4 - AVLNIR
15 - SBB
3 - AVHNIR
Category
Net Change (pixels)
1e7
Py6S - Top Gainers/Losers
1 - SVHNIR
33 - UN
18 - WBB_BBSH
9 - HRBCR
2 - SVLNIR
27 - TNCLV
15 - SBB
4 - AVLNIR
8 - SHRBRLNIR
3 - AVHNIR
Category
Net Change (pixels)
1e7

Appendix P - Alpine valleys – systematic bias (from top to bottom: winter, spring, summer, autumn)

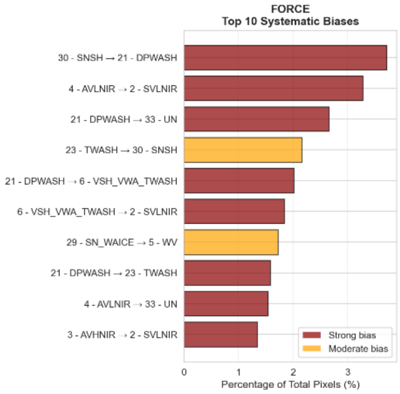

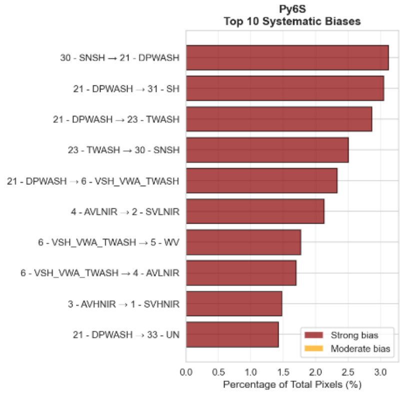

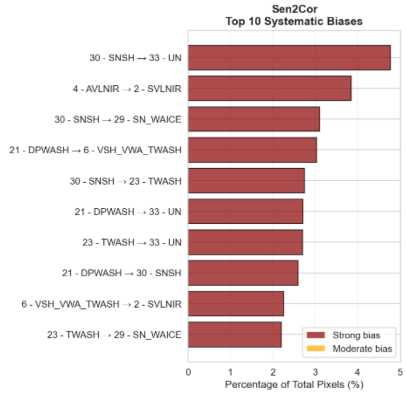

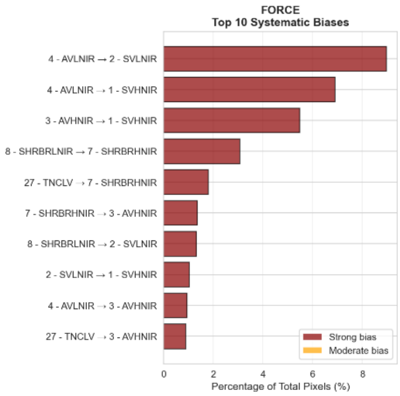

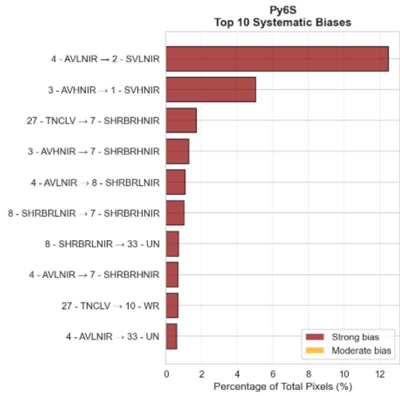

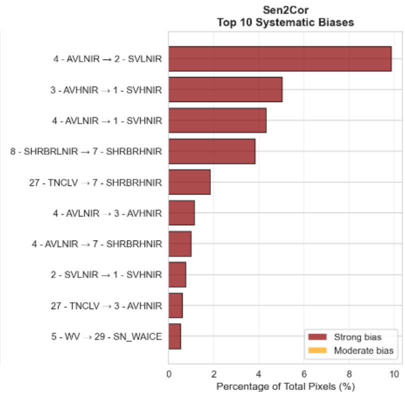

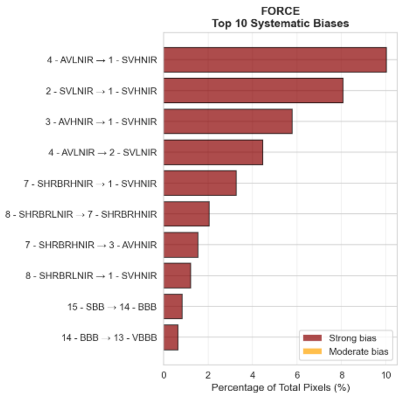

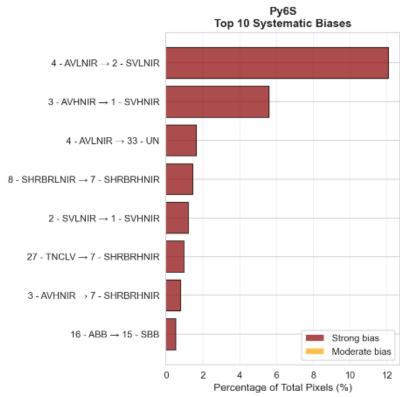

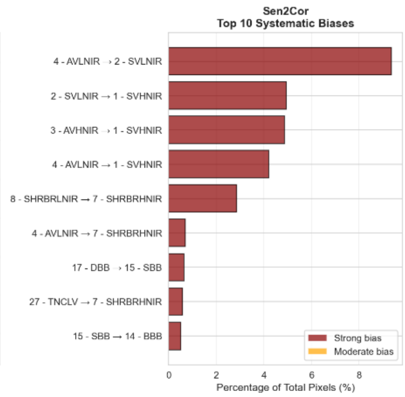

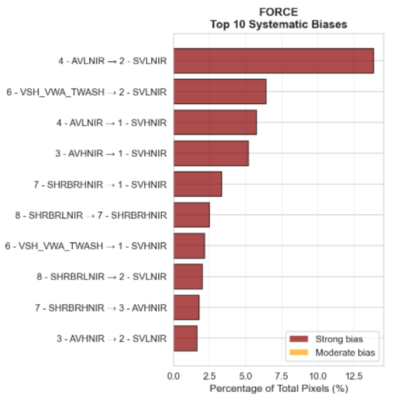

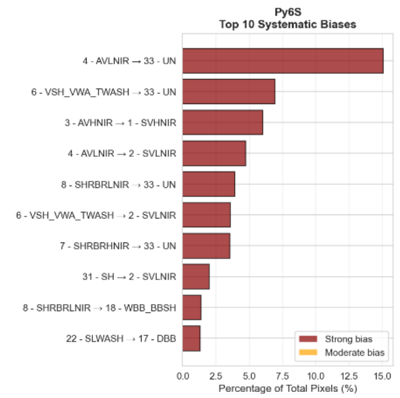

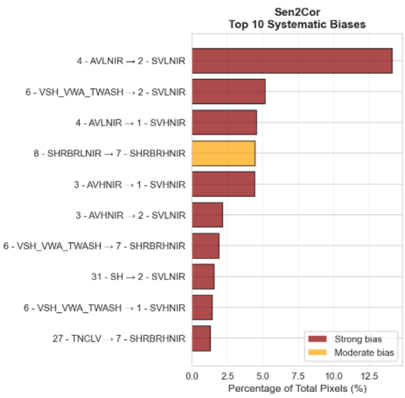

Appendix Q – High Alps – systematic bias (from top to bottom: winter, spring, summer, autumn)

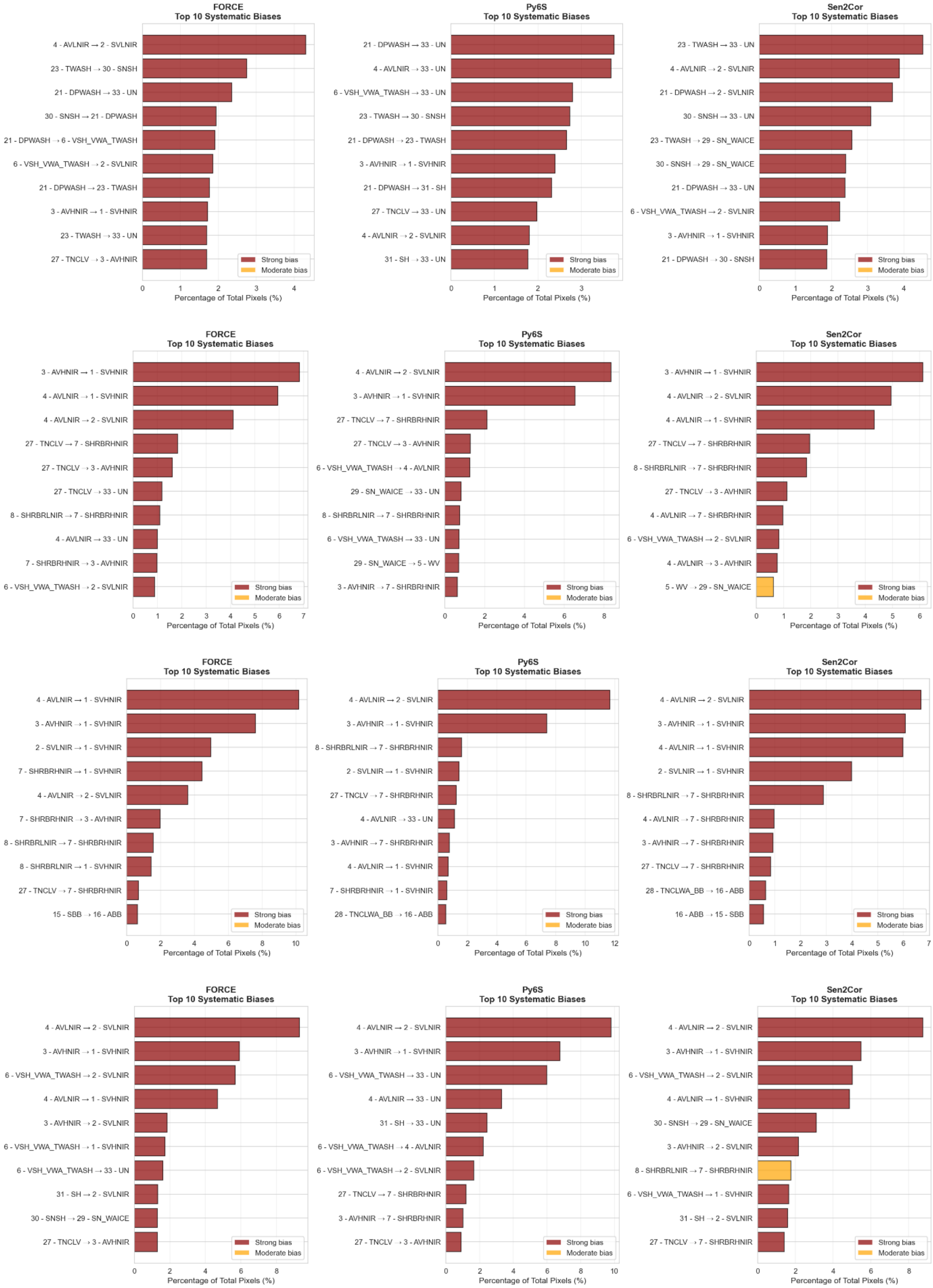

Appendix R – Pre-Alps – systematic bias (from top to bottom: winter, spring, summer, autumn)

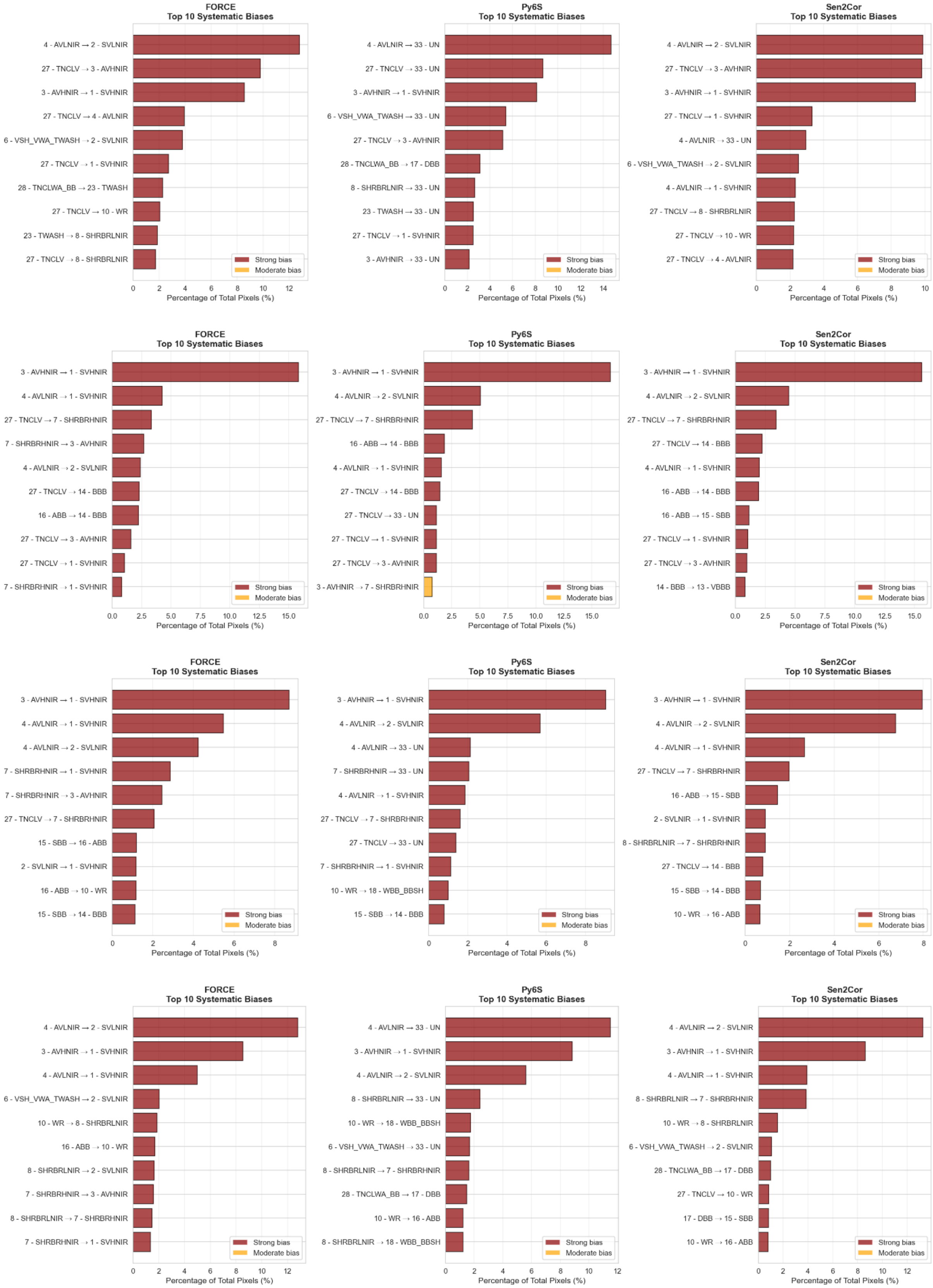

Appendix S – Eastern planes – systematic bias (from top to bottom: winter, spring, summer, autumn)

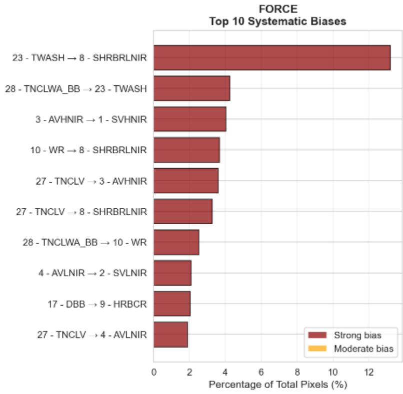

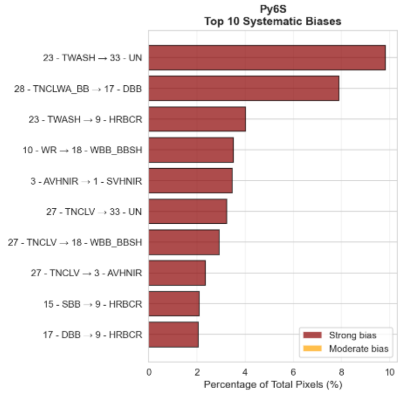

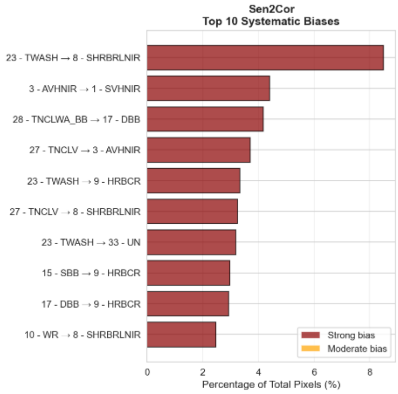

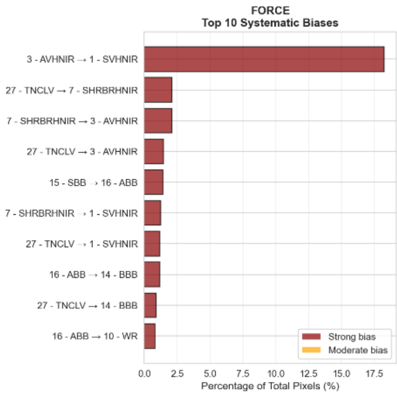

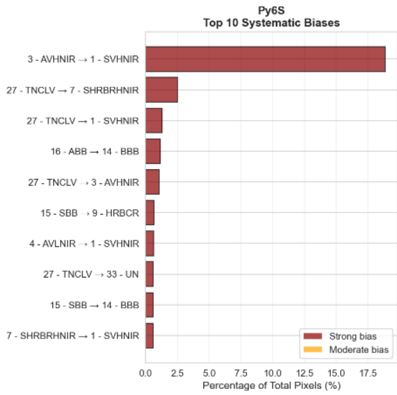

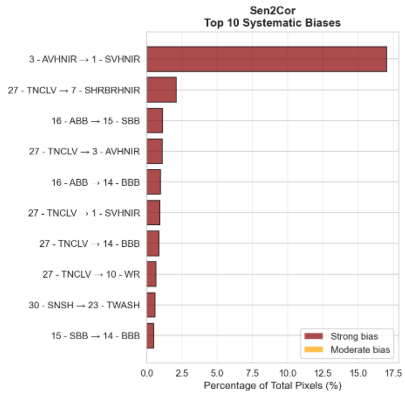

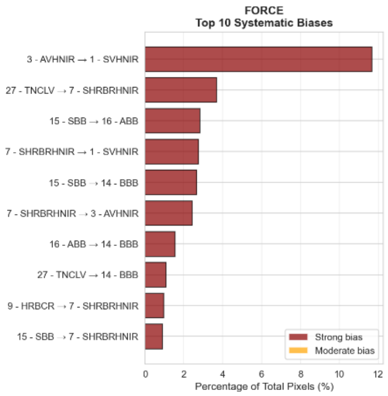

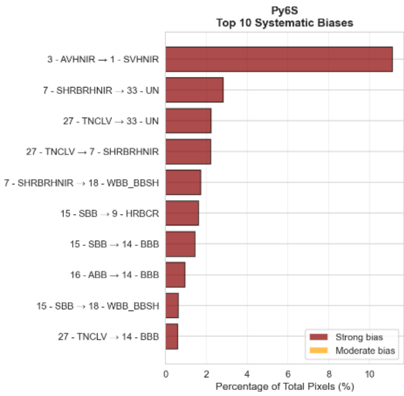

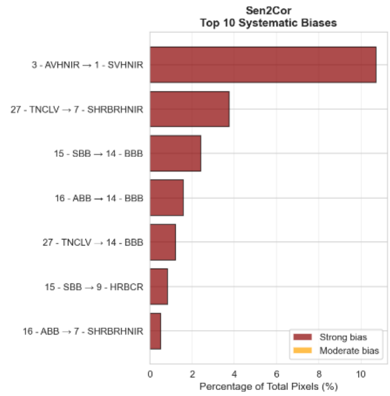

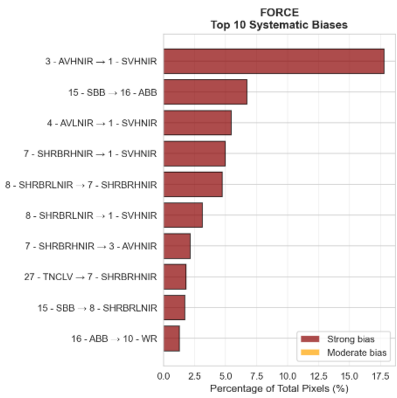

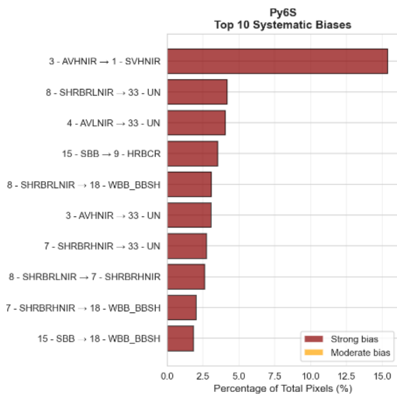

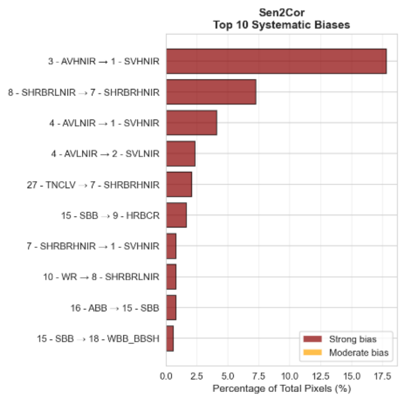

Appendix T - Alpine valleys – change severity distribution (from top to bottom: winter, spring, summer, autumn)

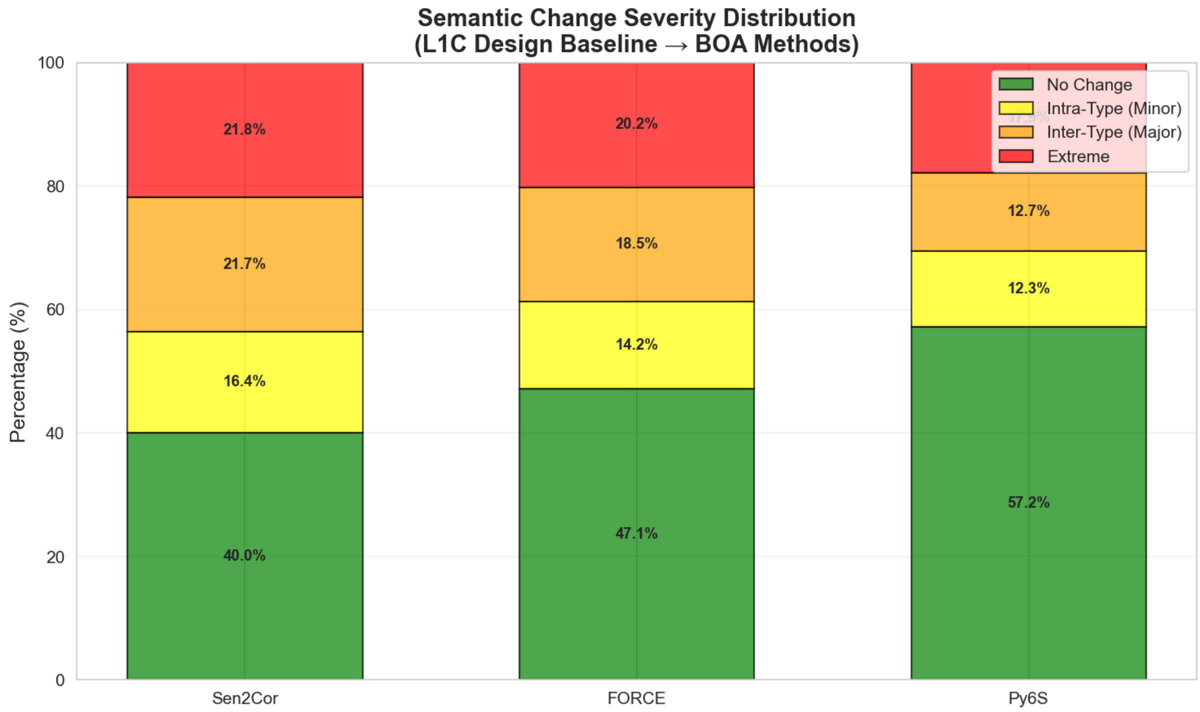

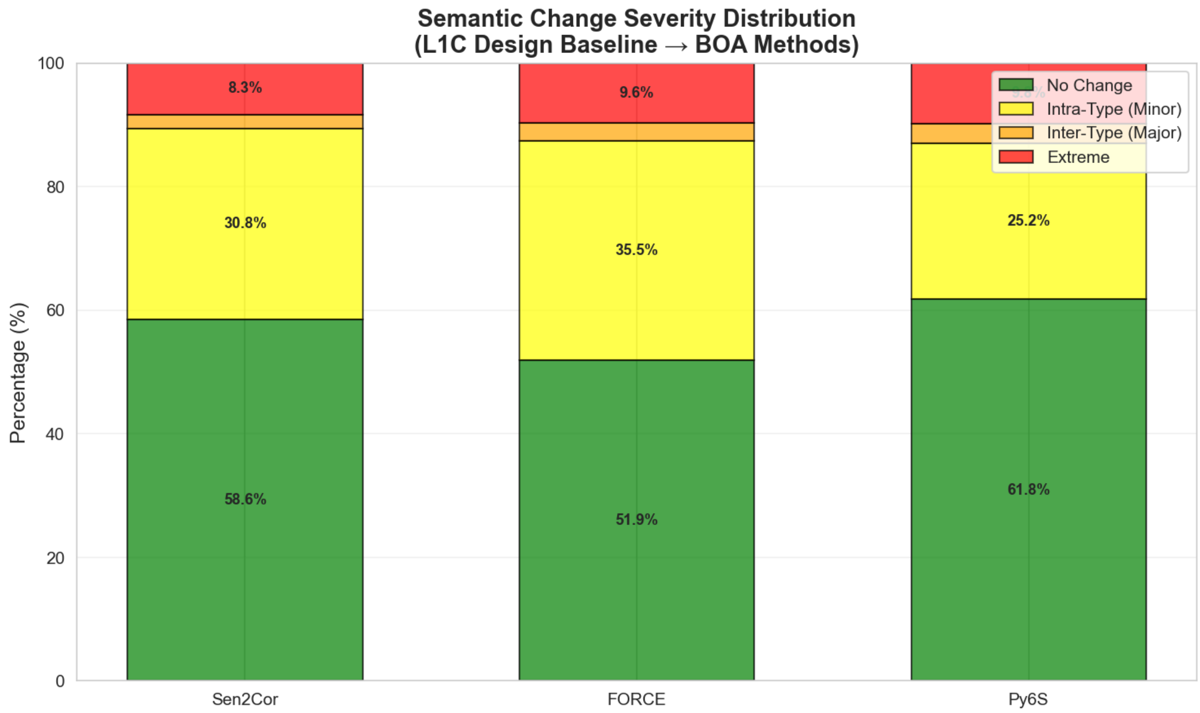

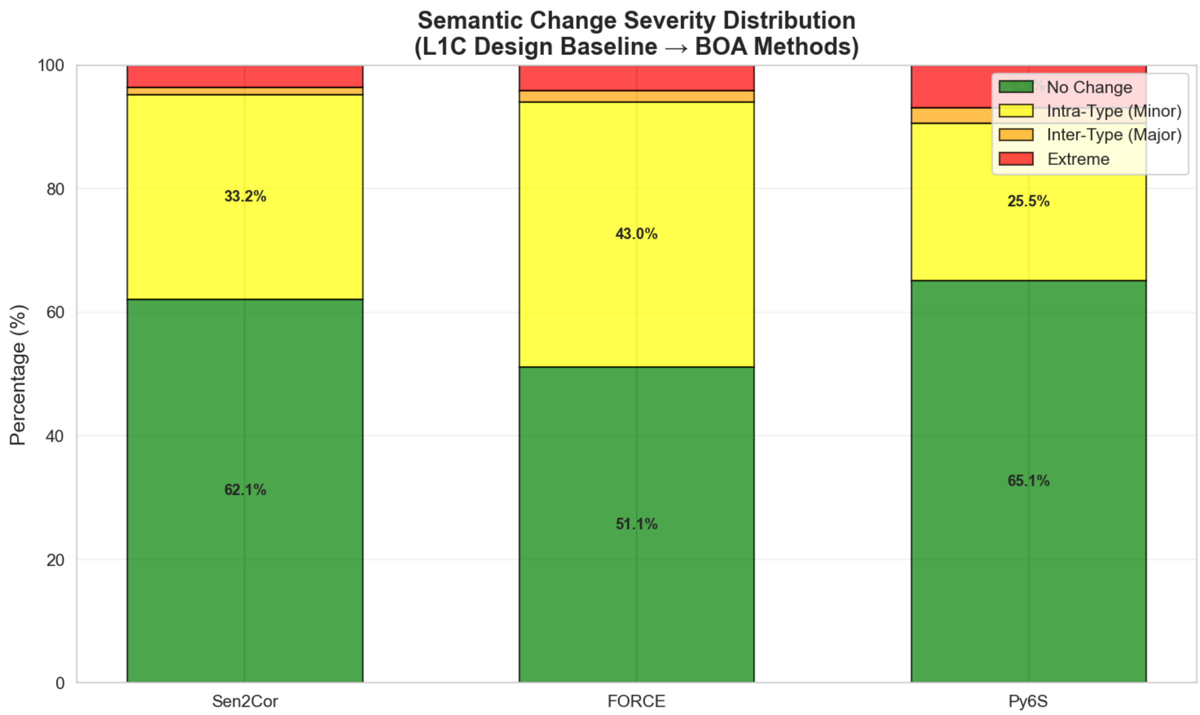
Semantic Change Severity Distribution
(L1C Design Baseline → BOA Methods)
Percentage (%)
0
20
40
60
80
100
Sen2Cor
FORCE
Py6S
No Change
Intra-Type (Minor)
Inter-Type (Major)
Extreme
33.2%
62.1%
43.0%
51.1%
25.5%
65.1%

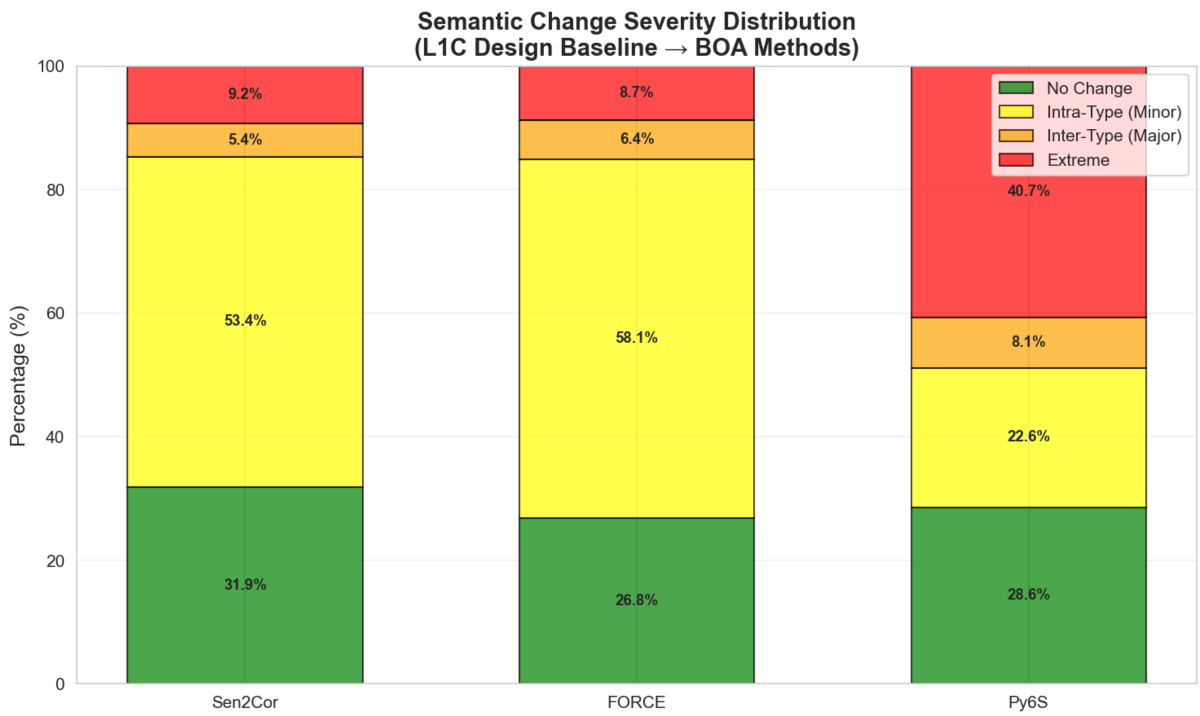
Semantic Change Severity Distribution
(L1C Design Baseline → BOA Methods)
Percentage (%)
0
20
40
60
80
100
Sen2Cor
FORCE
Py6S
No Change
Intra-Type (Minor)
Inter-Type (Major)
Extreme
9.2%
5.4%
53.4%
31.9%
8.7%
6.4%
58.1%
26.8%
40.7%
8.1%
22.6%
28.6%

Appendix U – High Alps – change severity distribution (from top to bottom: winter, spring, summer, autumn)

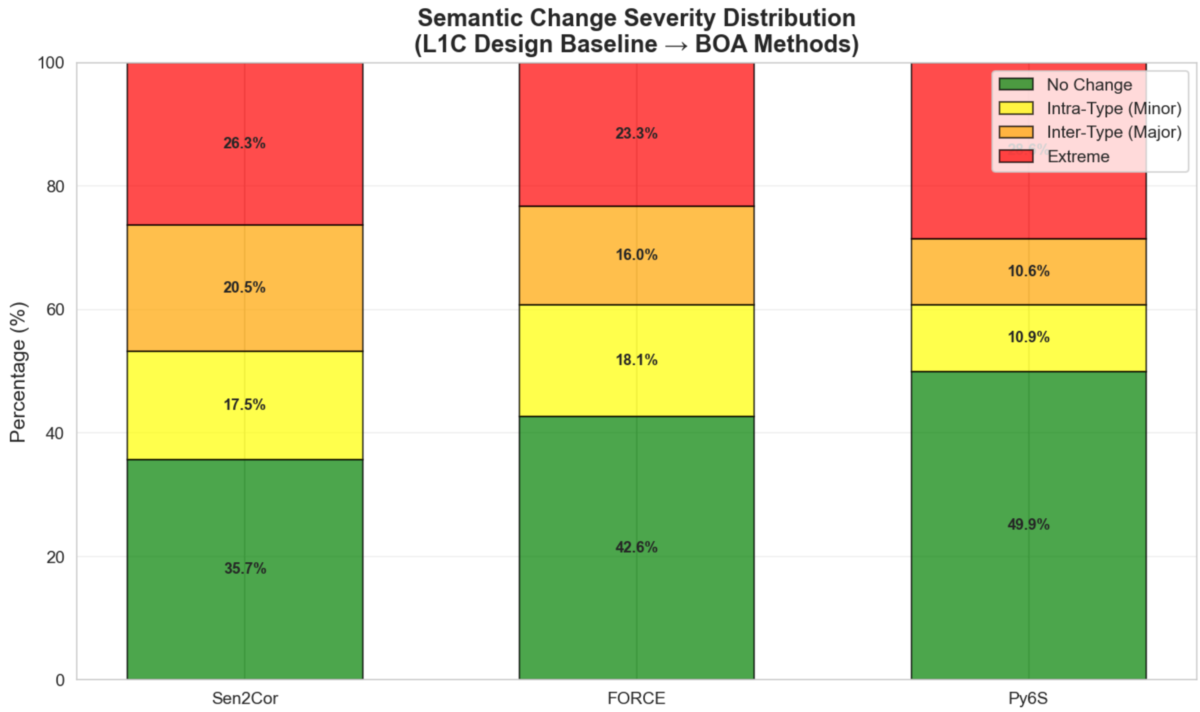

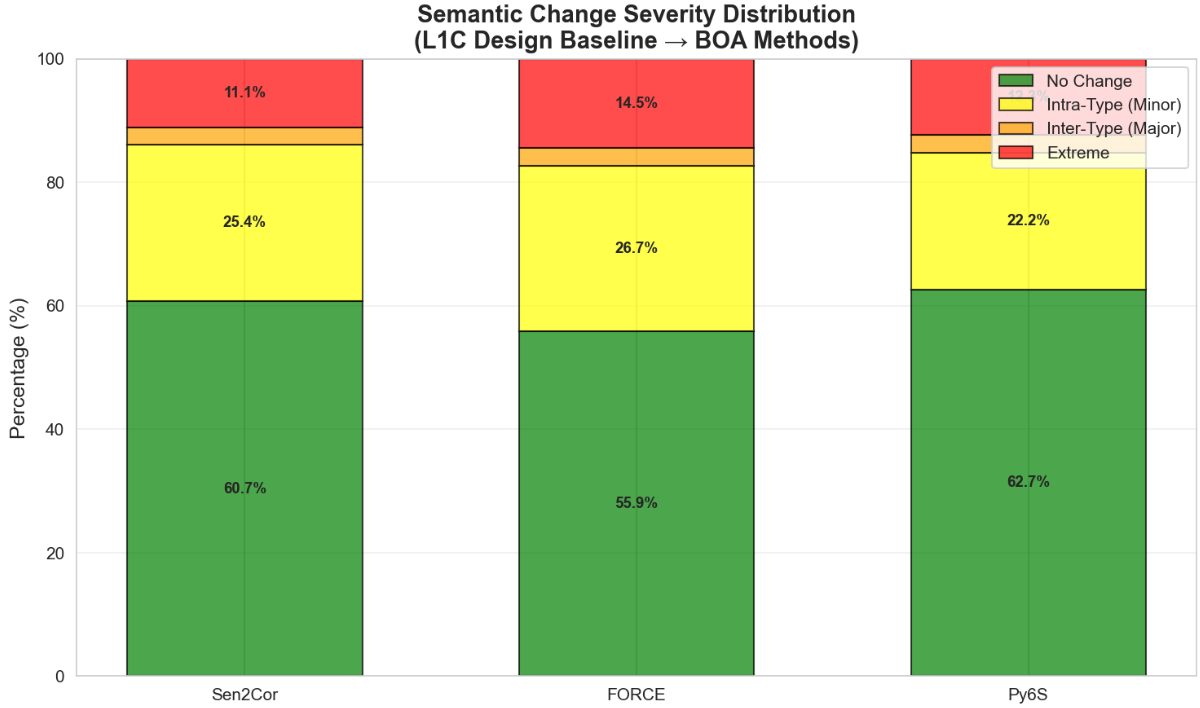

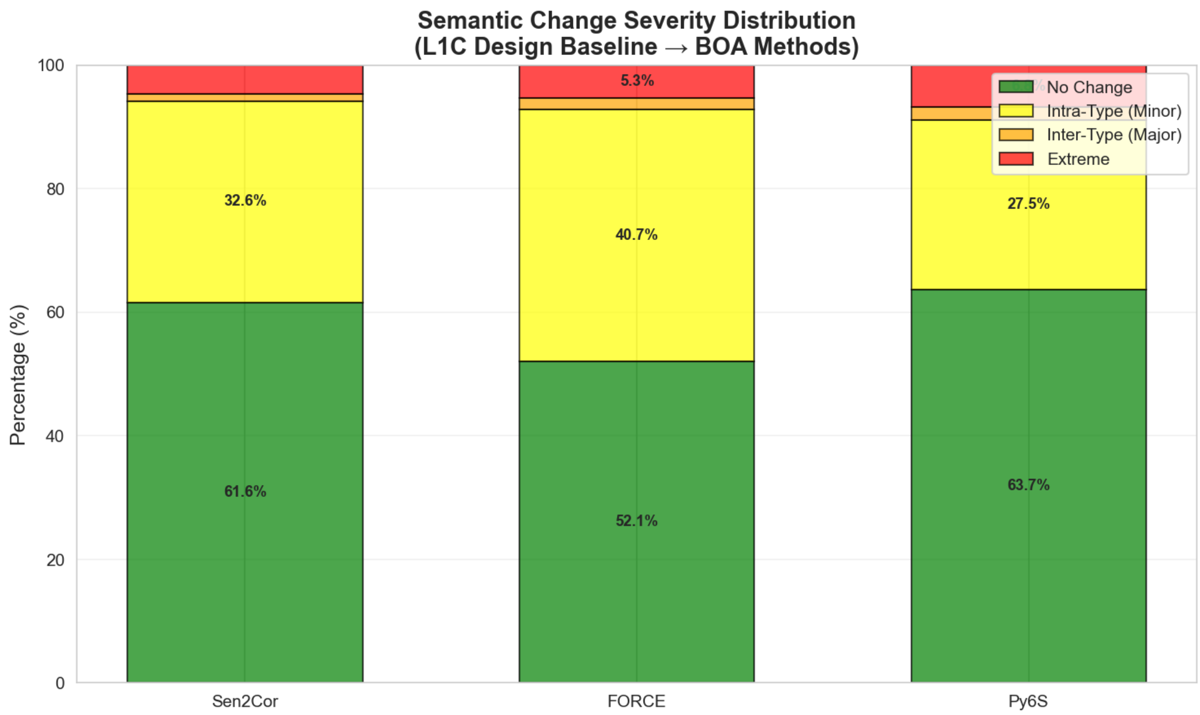
Semantic Change Severity Distribution
(L1C Design Baseline → BOA Methods)
Percentage (%)
0
20
40
60
80
100
Sen2Cor
FORCE
Py6S
No Change
Intra-Type (Minor)
Inter-Type (Major)
Extreme
61.6%
32.6%
52.1%
40.7%
5.3%
63.7%
27.5%

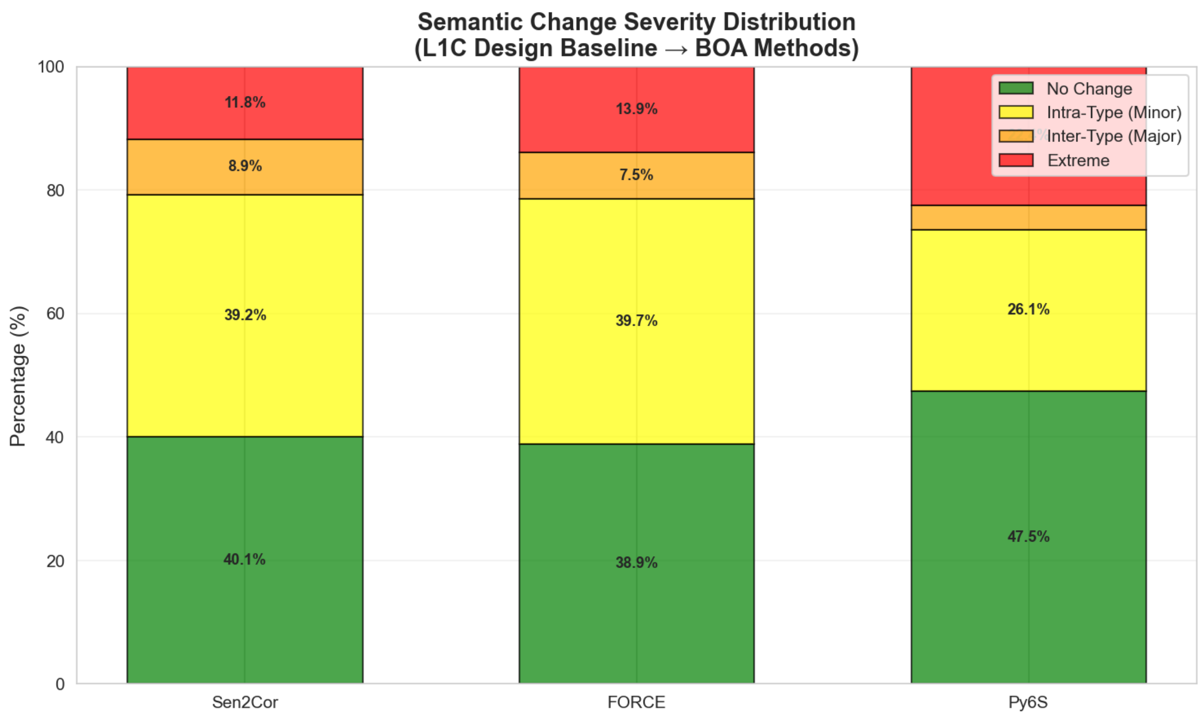
Semantic Change Severity Distribution
(L1C Design Baseline → BOA Methods)
Percentage (%)
0
20
40
60
80
100
Sen2Cor
FORCE
Py6S
No Change
Intra-Type (Minor)
Inter-Type (Major)
Extreme
40.1%
39.2%
8.9%
11.8%
38.9%
39.7%
7.5%
13.9%
47.5%
26.1%

Appendix V – Pre-Alps – change severity distribution (from top to bottom: winter, spring, summer, autumn)

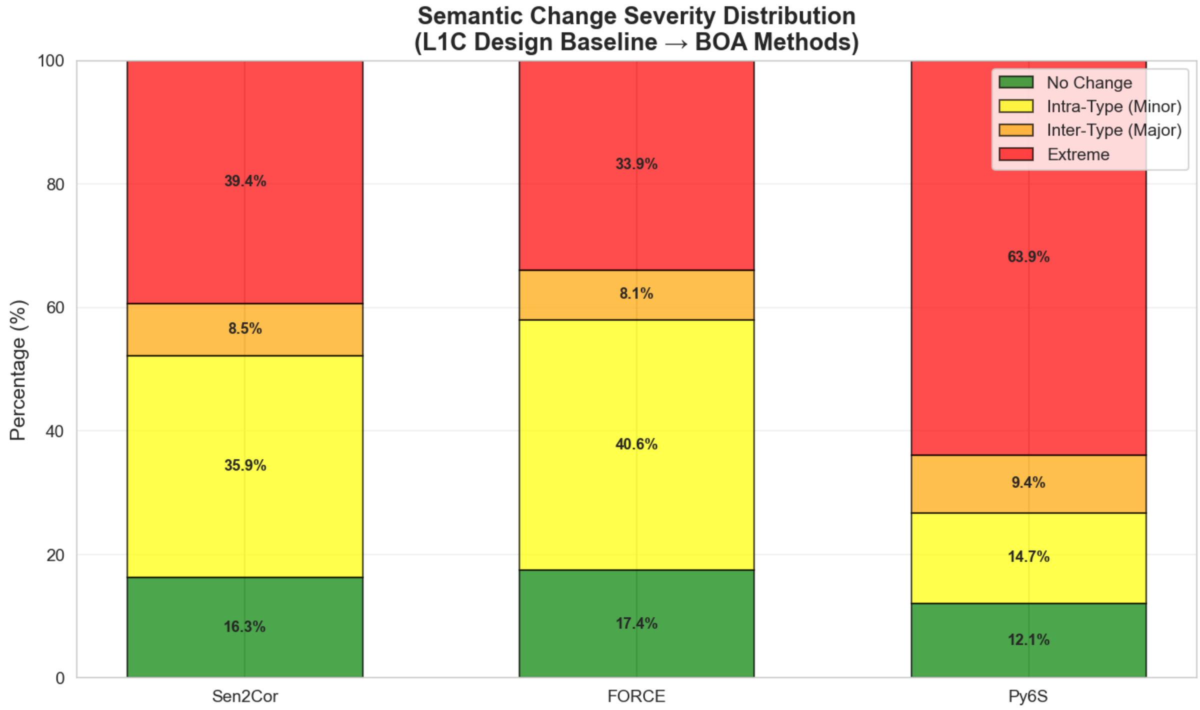

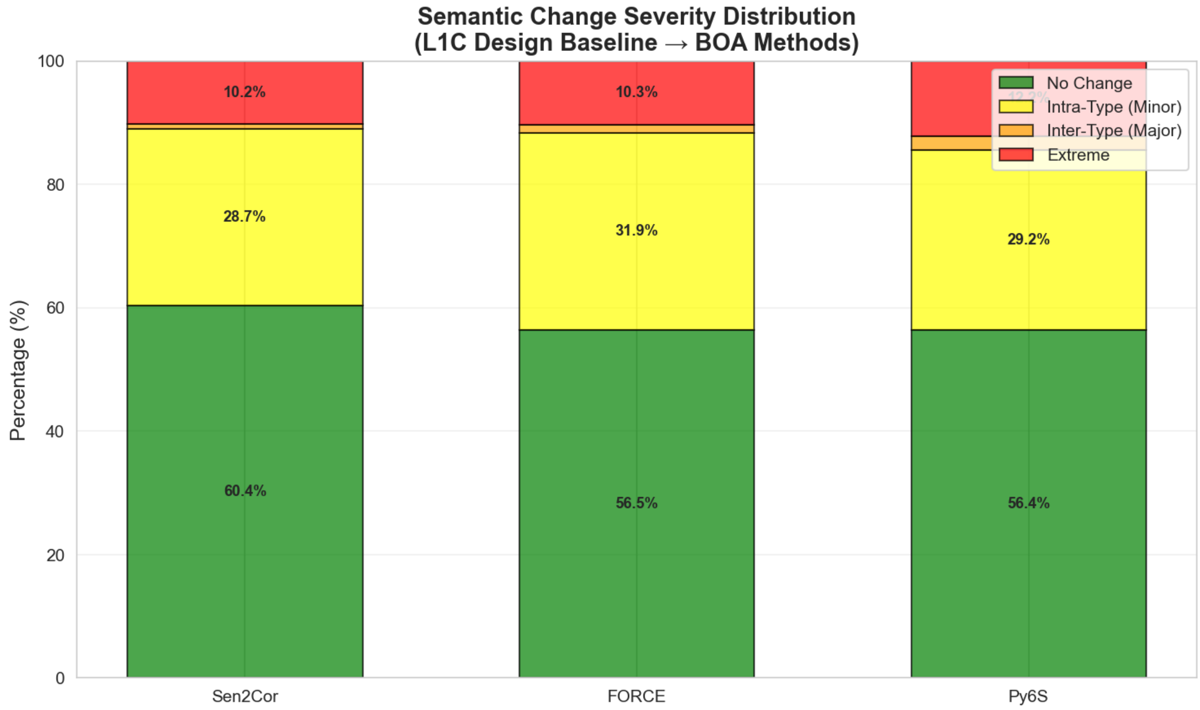

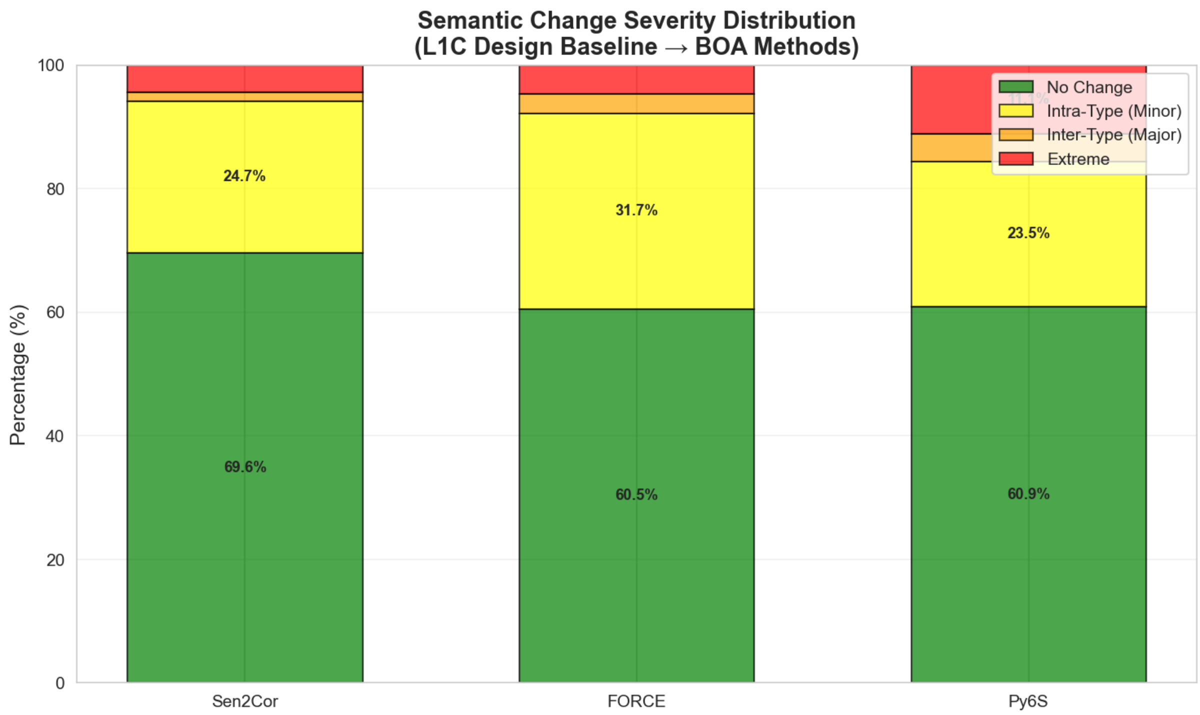
Semantic Change Severity Distribution
(L1C Design Baseline → BOA Methods)
Percentage (%)
0
20
40
60
80
100
No Change
Intra-Type (Minor)
Inter-Type (Major)
Extreme
69.6%
24.7%
60.5%
31.7%
60.9%
23.5%
Sen2Cor
FORCE
Py6S

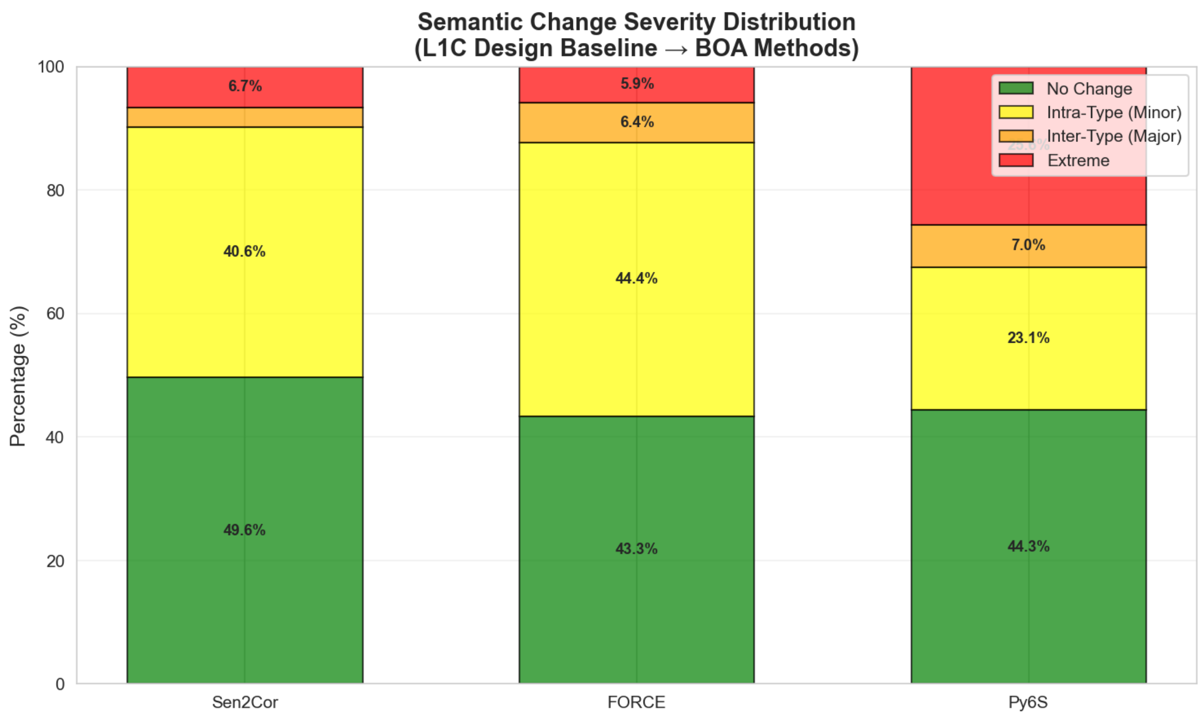
Semantic Change Severity Distribution
(L1C Design Baseline → BOA Methods)
Percentage (%)
0
20
40
60
80
100
No Change
Intra-Type (Minor)
Inter-Type (Major)
Extreme
6.7%
40.6%
49.6%
5.9%
6.4%
44.4%
43.3%
7.0%
23.1%
44.3%
Sen2Cor
FORCE
Py6S

Appendix W – Eastern planes – change severity distribution (from top to bottom: winter, spring, summer, autumn)

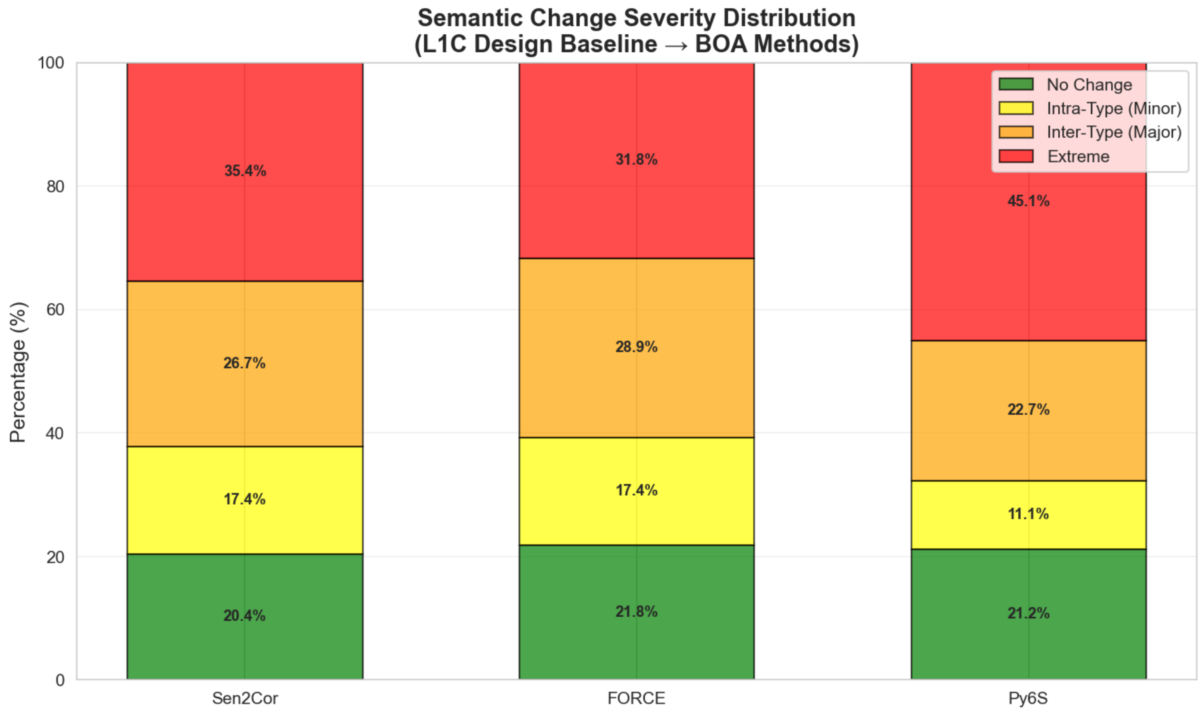

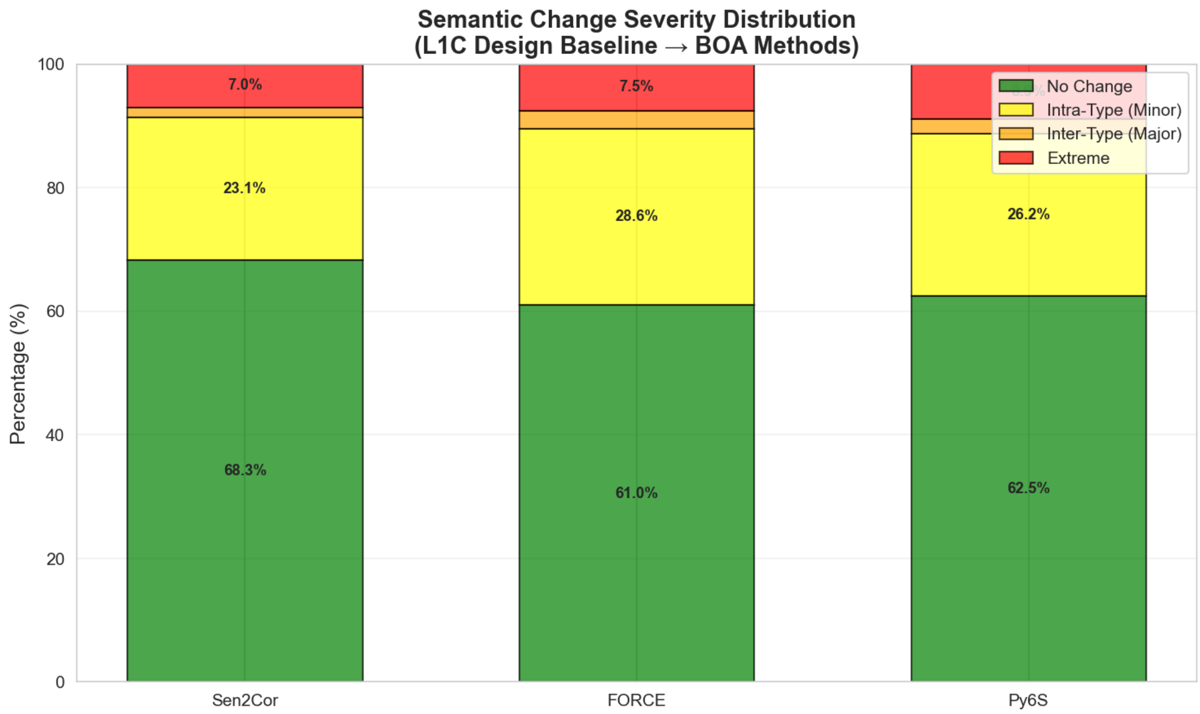

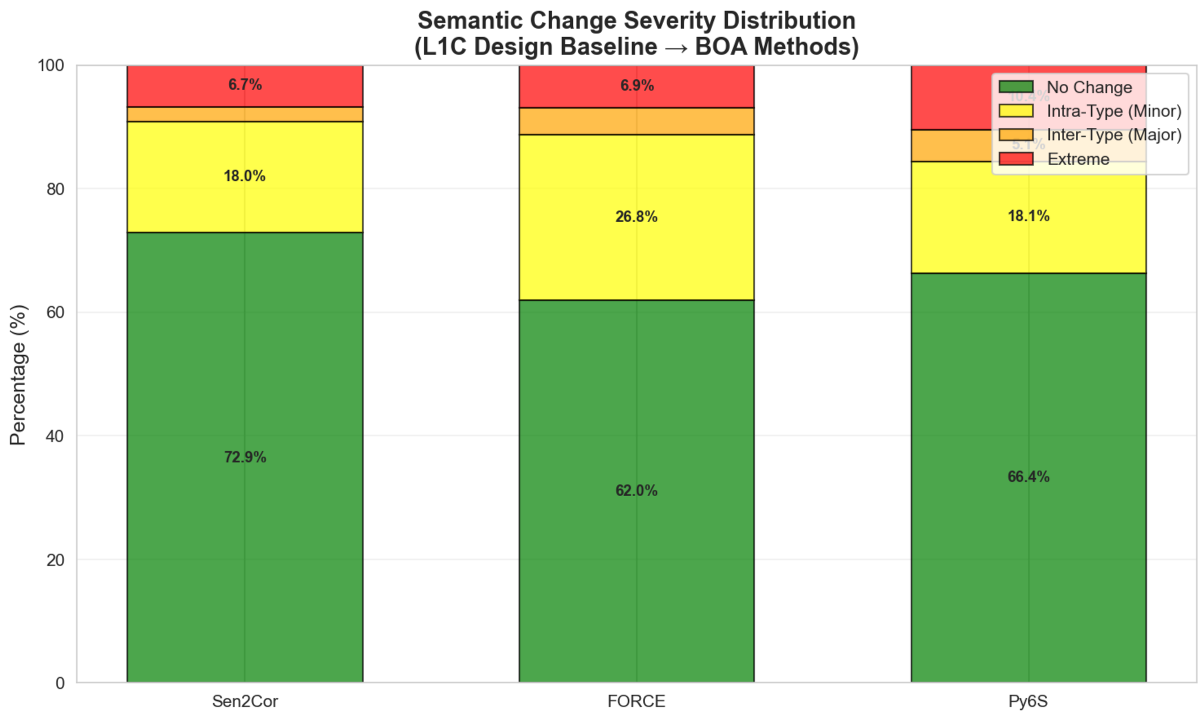
Semantic Change Severity Distribution
(L1C Design Baseline → BOA Methods)
Percentage (%)
0
20
40
60
80
100
Sen2Cor
FORCE
Py6S
No Change
Intra-Type (Minor)
Inter-Type (Major)
Extreme
6.7%
18.0%
72.9%
6.9%
26.8%
62.0%
18.1%
66.4%

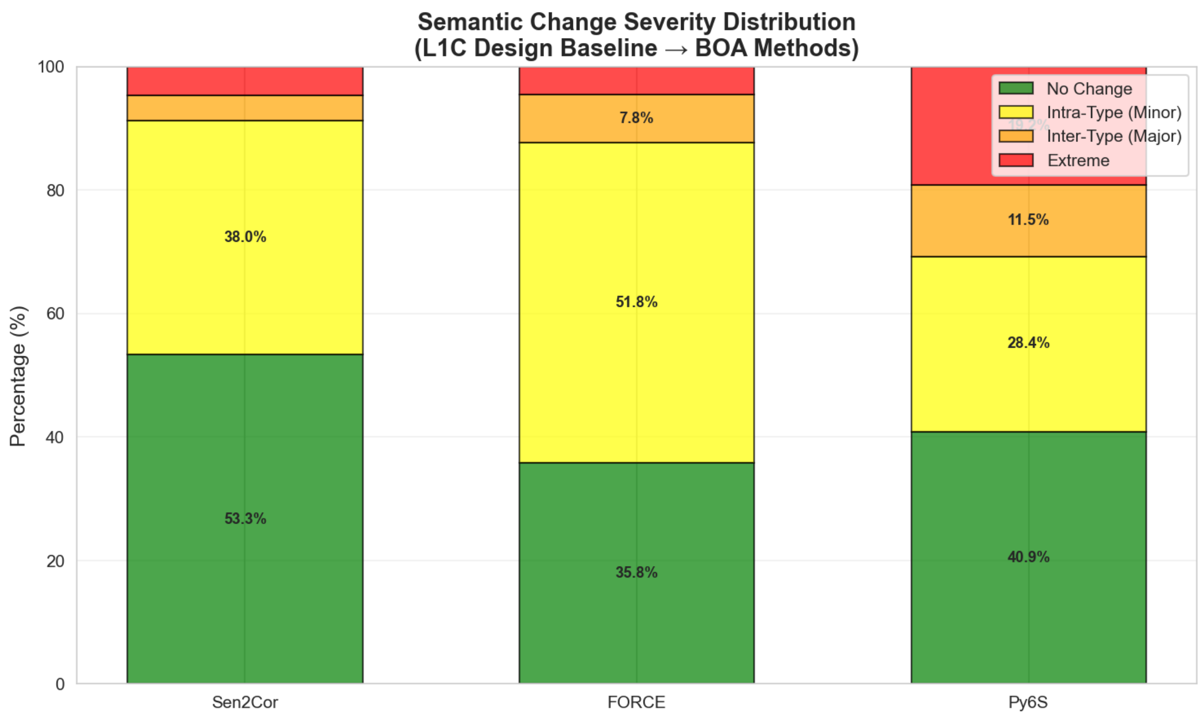
Semantic Change Severity Distribution
(L1C Design Baseline → BOA Methods)
Percentage (%)
0
20
40
60
80
100
Sen2Cor
FORCE
Py6S
No Change
Intra-Type (Minor)
Inter-Type (Major)
Extreme
38.0%
53.3%
7.8%
51.8%
35.8%
11.5%
28.4%
40.9%

Appendix X - Alpine valleys – cover type stability (from top to bottom: winter, spring, summer, autumn)

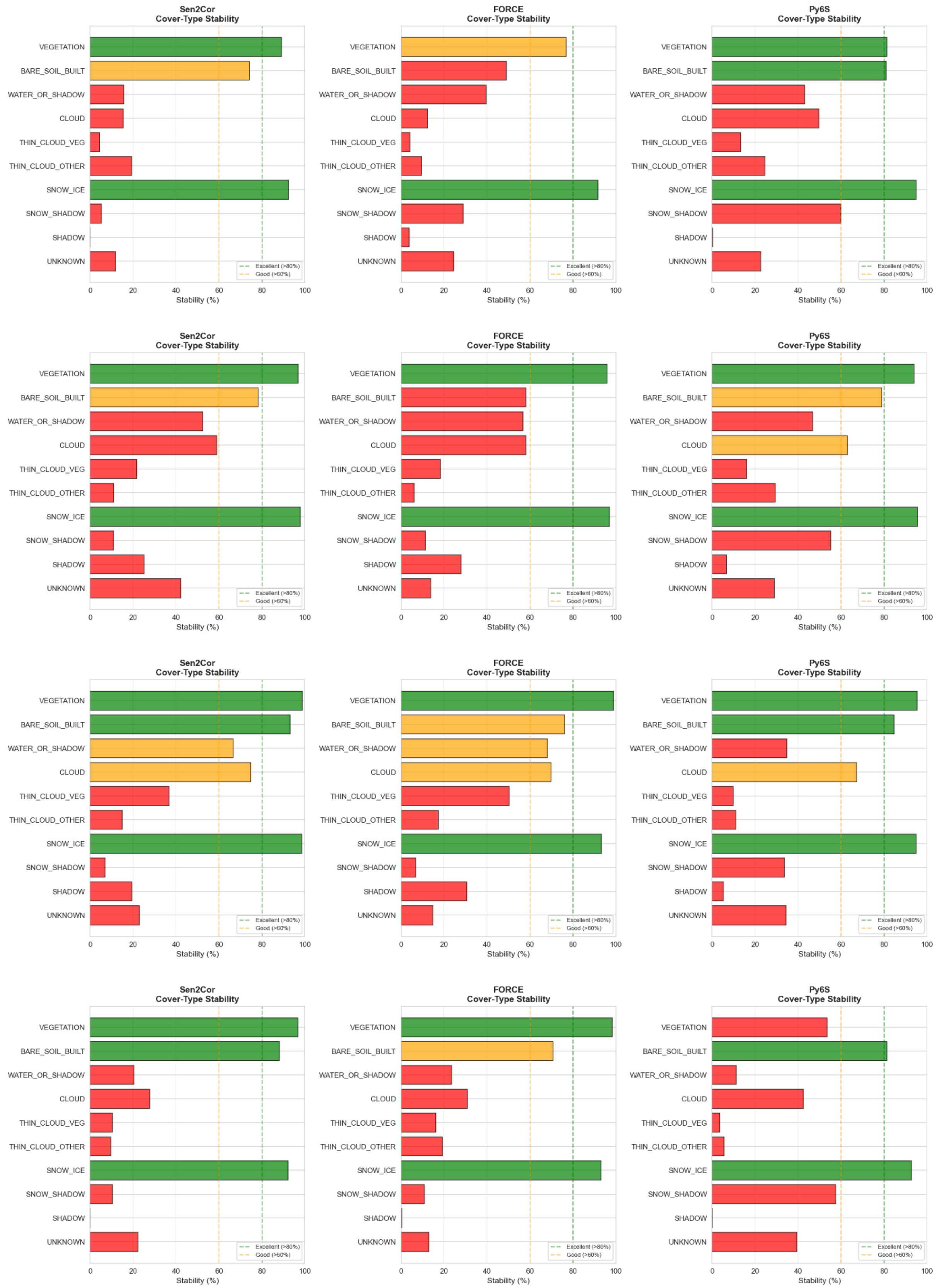

Appendix Y – High Alps – cover type stability (from top to bottom: winter, spring, summer, autumn)

Appendix Z – Pre-Alps – cover type stability (from top to bottom: winter, spring, summer, autumn)

Appendix AA – Eastern planes – cover type stability (from top to bottom: winter, spring, summer, autumn)

Appendix AB – SIAM categories

Table 4 - SIAM categories with their colour symbolization, abbreviations and descriptions (Major et al., 2025, Table 2)

	SVHNIR	Strong vegetation with high NIR
	SVLNIR	Strong vegetation with low NIR
	AVHNIR	Average vegetation with high NIR
	AVLNIR	Average vegetation with low NIR
	WV	Weak vegetation
	VSH_VWA_TWASH	Vegetation in shadow or vegetation in water or turbid water or shadow
	SHRBRHNIR	Shrub rangeland with high NIR
	SHRBRLNIR	Shrub rangeland with low NIR
	HRBCR	Herbaceous rangeland
	WR	Weak rangeland
	PB	Pit bog
	GH	Greenhouse
	VBBB	Very bright Bare soil (barren land) or built-up
	BBB	Bright bare soil (barren land) or built-up
	SBB	Strong bare soil (barren land) or built-up
	ABB	Average bare soil (barren land) or built-up
	DBB	Dark bare soil (barren land) or built-up
	WBB_BBSH	Weak bare soil (barren land) or built-up or bare soil (barren land) or built-up in shadow
	NIRPBB	Near infrared-peaked bare soil (barren land) or built-up
	BA	Burned area
	DPWASH	Deep water or shadow
	SLWASH	Shallow water or shadow
	TWASH	Turbid water or shadow
	SASLWA	Salty shallow water
	CL	Cloud
	SMKPLM	Smoke plume
	TNCLV	Thin cloud over vegetation
	TNCLWA_BB	Thin clouds over water or bare soil (barren land) or built-up
	SN_WAICE	Snow or water ice
	SNSH	Snow in shadow
	SH	Shadow areas
	FLAME	Flame, active fire
	UN	Unknown
	MASKED_NO_DATA	No data